Two-terminal transport measurements with cold atoms

Topical Review

Two-terminal transport measurements with cold atoms

Sebastian Krinner[1]**, Tilman Esslinger**[1] **and Jean-Philippe Brantut**[2,3]

[1] Institute for Quantum Electronics, ETH Zurich, 8093 Zurich, Switzerland
[2] Institute of Physics, EPFL, 1015 Lausanne, Switzerland

E-mail: jean-philippe.brantut@epfl.ch

CrossMark

Abstract

In recent years, the ability of cold atom experiments to explore condensed-matter-related questions has dramatically progressed. Transport experiments, in particular, have expanded to the point in which conductance and other transport coefficients can now be measured in a way that is directly analogous to solid-state physics, extending cold-atom-based quantum simulations into the domain of quantum electronic devices. In this topical review, we describe the transport experiments performed with cold gases in the two-terminal configuration, with an emphasis on the specific features of cold atomic gases compared to solid-state physics. We present the experimental techniques and the main experimental findings, focusing on—but not restricted to—the recent experiments performed by our group. We finally discuss the perspectives opened up by this approach, the main technical and conceptual challenges for future developments, and potential applications in quantum simulation for transport phenomena and mesoscopic physics problems.

Keywords: cold atoms, quantum simulation, mesoscopic physics, quantum transport

(Some figures may appear in colour only in the online journal)

1. Introduction

The measurement of transport between particle reservoirs, or terminals, exposes the fundamental properties of quantum matter, such as the insulating and superconducting behavior, or the quantization of conductance. These properties are in fact often used to classify solid-state systems. Understanding the underlying processes is essential for the construction of almost all solid-state devices, where transport properties determine the suitability of a material for a desired application, ranging from energy harvesting, to the conveyance, storage and processing of information. From a more fundamental

point of view, transport measurements provide a well-defined setting to study challenging questions in out-of-equilibrium quantum many-body physics.

Indeed, the study of transport in condensed matter physics has been a driving force for advancements in quantum mechanics, since transport entails both static, equilibrium properties of matter, such as the density of states, and its dynamic aspects, such as the nature of excitation above the ground state. In parallel with an understanding of increasingly more complex materials, progress in the control of semiconductor materials has allowed for the fabrication of almost defect-free systems. These have led to the development of quantum devices, where the quantum behavior is engineered at the mesoscopic level (see for example [1]). Contrary to materials where the quantum nature of the system emerges spontaneously in the ground state of the (possibly many-body) problem, such as in superconductors or quantum Hall effects, here the quantum aspect is imposed by a specially designed

[3] Author to whom any correspondence should be addressed

structure. In most cases the quantum mechanical nature of the effects is revealed by their consequences on the transport properties.

During the last decade, cold atoms have emerged as a powerful tool for investigating models originating from condensed matter physics. The idea is to use a quantum degenerate gas of neutral atoms to simulate the behavior of electrons in these model systems and to explore regimes not accessible to solid-state systems. Prominent examples include the Hubbard model [2, 3], BCS pairing and the BEC–BCS crossover [4], as well as topological quantum matter [5]. By construction, the atomic gas is free of any impurity or disorder, and is almost perfectly isolated from the environment. In addition, the relevant length and energy scales in an atomic cloud differ by orders of magnitude from those of an electron gas in a solid:

Density scale. A typical degenerate Fermi gas has a density of about $10^{12}\,\mathrm{cm}^{-3}$, which amounts to an interparticle spacing of about 1 μm, which is comparable to the wavelength of typical near-infrared or visible light. This allows for the creation, manipulation and observation of atomic gases by optical techniques: optical lattices are made from interfering laser beams and often operate in the single band Hubbard regime [2, 3], disorder is created by optical speckle patterns leading to Anderson localization [6], and high resolution microscopes can resolve individual particles in a many-body system [7–14].

Energy scale. Because of the large mass of atoms and the low densities, cold gases operate with Fermi energies in the micro-Kelvin regime, and are cooled using a combination of laser cooling and evaporative cooling to reach quantum degeneracy [15]. In turn, these low energy scales translate into long timescales for the microscopic evolution of the system. This allows for time-resolved control over the internal degree of freedom of atoms on time scales shorter than the Fermi time, using standard radio frequency technologies.

The quest to measure the transport properties of cold atomic gases originates in the requirement to further complete the toolbox for the quantum simulations of condensed matter models, as well as in the prospect of addressing a new set of questions in many-body physics. For the quantum simulations of solid-state systems, it is essential to extract the same observables as in the simulated device and reproduce its phenomenology. This also allows for a direct comparison between the measurements carried out on the device with those obtained by a quantum simulation—even without the need for modeling the system or having precise knowledge of all aspects of the underlying Hamiltonian. From the point of view of the quantum engineering of new many-body systems, cold atoms offer a situation where device-like systems can be carved from a fully controlled material. The control extends to parameters, such as the strength of interactions between the particles, or the nature and strength of disorder, which are not controlled or out of reach in quantum devices made of solid-state materials.

The question of transport has been investigated from various points of view in cold atom physics, but for a long time

experiments were not able to explore it in full generality: in most cases transport processes occur as density redistribution within atomic clouds, where thermal equilibration time and length scales are not separated from the transport scales themselves (see for example [16, 17]). This coupled evolution hinders the systematic extraction of transport coefficients independently of the static properties. This limitation was overcome by the two-terminal technique that we applied to cold atomic gas systems in our group during the last few years. The principal concept was pioneered in mesoscopic solid-state physics, and provides access to transport coefficients. In cold gases, it can be applied to both weakly and strongly interacting systems and it yields observables that are the direct counterparts of the condensed-matter measurements [18–25]. In particular, a precise meaning is given to conductance and other transport coefficients despite the gases being charge-neutral.

The paper is structured as follows: the remainder of the introduction is devoted to a short description of the various techniques related to the transport used in cold atoms, and to a conceptual presentation of the two-terminal approach providing a precise definition of transport coefficients for general charge-neutral systems. The second section describes the experimental techniques, in particular the initialization of the measurements and the interpretation of the results. In the third section, we describe experiments with noninteracting particles, where the conductor is in a multimode regime, illustrating the experimental techniques. The fourth section is dedicated to experiments with a single- mode conductor, the observation of quantized conductance and its interpretation using the Landauer formalism. In section five, we describe some transport experiments with a Bose–Einstein condensate and discuss the role of superfluidity. In section six, recent experiments with strongly attractive Fermions are described, showing some of the consequences of pairing and superfluidity. The last section discusses the perspectives and challenges opened up by these results, both as tools for the study of quantum gases and as a quantum simulator for condensed-matter-related questions.

1.1. Transport measurements and cold atomic gases

To investigate the transport properties of quantum gases, a variety of approaches have been tested. The reason for this diversity is the isolated nature of quantum gases, which prevents the direct connection of a cold atom device to a battery capable of biasing the system, and injecting and collecting atoms driven through the system. Therefore, no strictly DC currents can exist in a cold gas and the response is inherently transient. The main techniques used so far can be roughly classified as follows.

1.1.1. Response to an external force. The cloud is subject to a homogeneous force and subsequent evolution is observed. In a harmonic trap, this yields dipole oscillations of the center of mass of the cloud, which is fully decoupled from the internal properties of the gas by virtue of Kohn's theorem [26]. Upon superimposing an extra potential, such as a lattice or a random potential, the oscillations get damped and their relaxation rate is used as a measure of the transport properties [16, 27–33].

The isolated nature of the atoms allows for their quantum coherent evolution under the influence of the homogenous force, leading to counterintuitive results. For example, atoms in an optical lattice show Bloch oscillations in the presence of an external force: atoms are constantly accelerated by the force until they reach the Bragg condition, and are then coherently reflected by the lattice yielding an oscillatory motion [34]. This observation illustrates the difficulties in interpreting the results of such homogenous force response in terms of transport coefficients: one would conclude that the DC conductance of a lattice is always zero, as the current response averages over the Bloch cycles. At timescales shorter than the Bloch period, the atoms are continuously accelerated as the quasi-momentum increases. This increase results from the phase coherence of the single particle wave function of the atoms over neighboring sites of the lattice. In the presence of perturbations, such as interactions between particles or disorder, Bloch oscillations are damped and dephased [35–40], and for some specific cases only the transport results of the linear response theory can be recovered [41].

1.1.2. Release and expansion of a cloud. In this case, a cold atom cloud is prepared in a trap, and the trap, or a specific direction of confinement, is released, letting the atoms freely expand. The initial cloud thus acts as a transient atom source [17, 42–49]. The atom laser, which is generated by continuously out-coupling atoms from a cloud, is a particularly refined instance of this situation [50–54]. Typically, the atoms interact with a background potential during the expansion, or among each other. The time evolution of the distribution of atoms following the release reveals information about the diffusion processes. In the simple case of noninteracting particles, the diffusion coefficient averaged over the initial energy distribution is directly accessible [46–48], and is measured to identify Anderson localization. In periodic structures, the coherent evolution yields ballistic expansion, which is compatible with the intuitive picture of a perfect lattice being a perfect conductor. In the presence of interactions between the particles, the evolution is more intricate as the edges of the cloud behave differently from the center. Nevertheless, some features have been observed, as interactions are varied in an optical lattice [17, 49, 55]. For very strongly interacting gases, the evolution can be modeled by a hydrodynamic expansion, and momentum transfer between the different directions during the expansion can be traced back to the shear viscosity of the homogenous gas [56, 57].

1.1.3. Coherent dynamics in superfluids. The long-range coherence is a distinctive feature of superfluids. The existence of a complex order parameter is at the root of some of the most intriguing manifestations of superfluidity. As far as transport is concerned, the most important consequence is that the superfluid current is proportional to the gradient of the phase of the order parameter. This implies, in particular, that the superfluid flow is irrotational, and angular momentum within the fluid is carried by quantized vortices. Such vortices have been extensively studied in the context of Bose–Einstein condensates, and successfully demonstrated for fermionic superfluids as well (see [58, 59] for reviews). The irrotational flow is particularly striking in the connected geometry of a ring trap, where it produces quantized permanent currents that are robust against weak perturbations [60–63].

For clouds or systems composed of several parts separated by short barriers or weak links, long-range phase coherence leads to the celebrated Josephson oscillations. These have been extensively studied with Bose–Einstein condensates, both as a manifestation of the superfluid character of the system, and as a tool to realize phase-sensitive measurements [64–68]. Such weak links have now been extended to fermionic superfluids [69].

1.1.4. Spin and heat diffusion. Beyond the transport of particles, several other conserved quantities can be transported within cold atomic clouds. In particular, for fermionic quantum gases, the internal degree of freedom plays an essential role. For electronic systems it is the spin of the particles, while for cold atoms the different hyperfine states—i.e. the relative orientation of the nuclear and electronic spin—play an analogous role. In the remainder of this review, we refer to internal degrees of freedom as spin in analogy with the electronic case. Using spin-selective manipulation tools, spin inhomogeneities can be produced in cold atomic clouds and their evolution monitored [70, 71]. For instance, a gradient of spin populations was created in [70] by spatially separating the spin components, and the relaxation of the system was observed, providing insights into the spin-diffusion coefficient of the strongly interacting Fermi gas. In other sets of experiments, the decoherence of a spin texture was investigated, and the transverse spin diffusion coefficient was observed [72–75]. One of the main focuses of these experiments is the investigation of strongly interacting Fermi gases, where the scattering mean free path is of the order of the interparticle spacing and the coefficients are believed to take universal values. Heat diffusion has been investigated in the same spirit by locally heating clouds, but it is technically more difficult in that it requires the local measurement of temperatures. The effects of superfluidity and interactions have been investigated via heat transport [76, 77], and a second sound was observed in strongly interacting Fermi superfluids [78].

1.1.5. Response to particle decay due to natural or induced losses. The existence of particle loss processes can be used to trigger transport across the system. Intrinsic losses, such as three-body collisions, have a natural density dependence and tend to create chemical potential and temperature gradients that can be used to extract transport coefficients [77]. Local addressing techniques allow losses to be induced at very short length scales within cold atomic clouds, creating a well-defined nonequilibrium situation, which triggers a time evolution that provides information on particle flow within the cloud [79, 80].

Even though these techniques all have intimate links with transport, their relation to the concepts of conductivity or conductance, as understood in condensed matter physics, is sometimes very indirect. Questions of timescales, length scales and trap averaging have to be investigated in a case-by-case fashion.

This review is devoted to the implementation of the Landauer two-terminal configuration for cold gases. We have
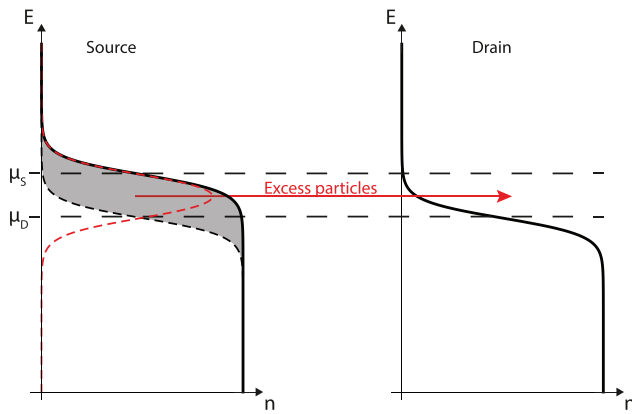
Figure 1. The concept of a two-terminal transport measurement. Source and drain reservoirs are contacted to the conductor of interest. A chemical potential difference is introduced between them, leading to different energy distributions of particles in the source and drain. A net current of particles is driven from the source, as a result of the excess of particles above the Fermi level of the drain. The red dashed line indicates the energy distribution of the particles giving rise to the net current.

developed this technique with the aim of providing a generic method to extract the equivalent of the DC conductance for a quantum gas system, in particular for fermionic quantum gases where the analogy with condensed matter systems is most relevant. The route that was followed is inspired by the Laudauer approach to transport, which (i) explicitly considers terminals that introduce the bias in the system and (ii) applies equally well to charged and charge-neutral particles, since it does not refer in any respect to electric fields or electrical potentials.

1.2. Two-terminal transport of particles

The generic concept of a two-terminal transport measurement is presented in figure 1. The system of interest is connected on two sides to particle reservoirs, which supply and collect particles to and from the system. A bias is then introduced between the two reservoirs, in the form of a chemical potential difference, and the resulting current through the system is observed. Conceptually, the chemical potential bias can be thought of as a thermodynamic force, driving a current of an extensive, thermodynamically conjugate quantity, namely the atom number.

By specifying the system of interest, the process by which the system is attached to the reservoirs is also specified. The nature of the interfaces with the reservoirs may have a large influence on the results, for example when their geometry leads to particle reflections. We also suppose that transport inside the conductor is fully elastic, i.e. energy is strictly conserved, as it is realized in cold atom experiments and in many condensed matter physics situations as well.

These reservoirs play a central role in the concept of two- or multiple-terminal transport measurements. It is assumed that they contain fast relaxation processes that ensure the quick thermalization of the incoming particles. By analogy with optics, reservoirs act like *perfect fermionic black-bodies*. Two important characteristics follow from these requirements:

Phase incoherence No quantum interference processes take place inside the reservoirs at the time and length scales relevant for the transport. This implies that particles emitted from different reservoirs have no phase relation. This also implies that energy is the only relevant character of the particles emerging out of one reservoir. In particular, all energetically available momenta are populated irrespective of the possible directions.

Energy relaxation Incident particles from the conductor are drawn from the energy distribution of another reservoir, possibly modified by interactions with the conductor. Fast scattering processes serve to erase the memory of the incident particles such that, should it be reemitted at later times, it will appear as having been drawn from the energy distribution of the reservoir it is emitted from.

In addition, the reservoirs are assumed to have standard reservoir properties from the point of view of statistical mechanics: they have a very large heat capacity, compressibility, spin susceptibility, etc, such that their chemical potential, temperature or spin potential is not affected by the emission and absorption of particles into and from the conductor.

In condensed matter physics, these hypotheses are natural and follow from the experimental situation, where leads are essentially infinite, and the intrinsic complexity of the materials ensures efficient inelastic processes in the leads. The strength of the Landauer approach is that it does not require a precise description of the physics of the reservoirs. The main disadvantage is that the hypothesis is very hard to check independently of the transport measurements themselves. As will be explained in the next sections, cold atoms offer a situation where the reservoirs can be experimentally observed and controlled, providing perspectives for novel tests of the validity and breakdown of the hypothesis underlying the Landauer approach.

The process by which the bias is introduced is usually not specified, and it is assumed that the system as a whole reaches a steady state in which a DC current is established, and its magnitude only depends on the bias rather than the precise history of the setup operation. While this is very likely to be the case in most experimental situations, it is worth noting that in some important cases, such as glasses, this may not be the case, or the establishment of the steady state may take an exponentially long time. There again, cold atom implementation offers a renewed perspective on this problem, owing to the long timescales at play, opening up the possibility of observing the establishment of a steady state.

The transport process can be understood from the point of view of the energy distribution in the reservoirs, as presented in figure 1. The two Fermi distributions describing the left and right reservoirs differ by their chemical potential, the difference being the bias. Since transport is elastic in the conductor, the current can be considered separately for each energy. This leads to the fundamental conclusion that the net current driven by the bias through the conductor originates from a narrow energy window around the Fermi level, the width of which is set by the bias or the temperature. In essence, it is

a differential measurement, in which the contributions of the low energy levels cancel between the source and the drain. A detailed calculation will be presented later in the specific context of the Landauer formula applied to a quantum point contact.

The fact that transport is a property of the Fermi surface is well known in condensed matter physics. The two-terminal configuration provides a concrete implementation of the transport measurement that fulfills this property. Interestingly, this approach directly applies to charge-neutral particles without having to exhibit a counterpart to electric fields and electric potentials. In cold atoms, the typical experimental observable is the density distribution measured destructively at a given time. It is not energy resolved, leading, for example, to well-known problems of thermometry in the degenerate regime where most of the atoms reside in the Fermi sea and carry no information about temperature. Energy resolution is restored using, for example, radio-frequency spectroscopy [81, 82], which is sensitive to the density of states, or Bragg spectroscopy measuring the density fluctuation spectrum [83, 84]. These techniques do not directly probe the localized or extended nature of the excitations at the Fermi level, which is an essential ingredient for the classification of phases of matter into insulating or metallic. The two-terminal transport measurements fill this gap in the cold atom toolbox. In addition, it gives a precise meaning to the conductance of a cold atomic gas.

By putting forward a description in terms of a system and reservoirs connected together but spatially separated, the Landauer approach leads naturally to a description of the system in terms of a *device*, connected in a circuit. Indeed, figure 1 provides a minimal circuit with two leads and a conductor. While this is natural for electronic systems, the approach is new in the field of cold atoms, where most of the systems considered are 'bulk'. The engineering of devices for atoms has been coined atomtronics, with an emphasis on reproducing the functionality of electronic devices. Here the device approach to cold atoms provides the natural way to perform and interpret transport measurements.

1.3. Heat and spin transport

The two-terminal approach can be directly generalized to the transport of other conserved quantities such as energy, spin etc. The cases of spin and heat (or energy) are relevant for some experiments and theoretical proposals in the context of cold atomic gases.

Figure 2(a) illustrates the case of spin transport. Here we suppose in addition that there is no interaction between the particles in different spin states within the reservoirs, or at least that these can be captured within a Fermi liquid picture. The spin bias, which is the thermodynamic force conjugate to magnetization, can be thought of as equal in magnitude with opposite chemical potential biases applied to the two spin components across the conductor. Following the reasoning above, in the narrow energy window around the Fermi energy, there is an excess of spin-up particles incident from
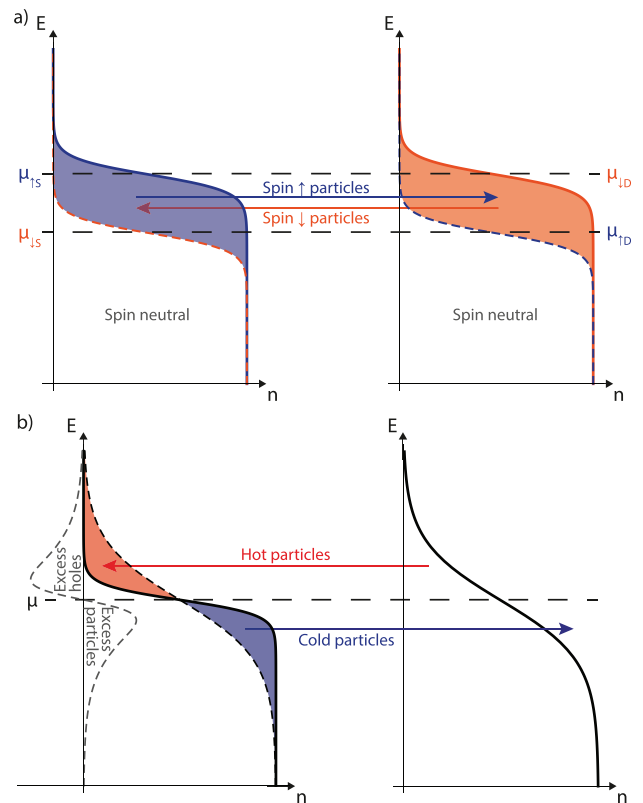

Figure 2. (a) Two-terminal transport of spin. Opposite chemical potential differences for the two spin components are introduced between the source and bias, driving currents of spin-up from the source to the drain and vice versa for spin-down. (b) Two-terminal transport of heat. The temperature difference between the source and drain drives a current of high energy particles from hot to cold, and a current of low energy particles from cold to hot.

the source, and an excess of spin-down particles incident from the drain. As a result, the net particle current is zero.

Such a configuration is particularly sensitive to scattering between the two spin components inside the conductor. Indeed, scattering between identical spin particles is forbidden, and scattering between different spin components is elastic, and thus conserves the total current. Thus, we expect the particle current to be weakly affected by interactions. In contrast, the spin current can be strongly damped by scattering, since momentum is not conserved within a single spin component. In the extreme case of a one-dimensional system, this yields the famous spin-charge separation. In conductors where interactions are important, the conductance and spin currents yield fundamentally different information compared to particle conductance alone.

In a situation where no net spin polarization is present, the spin and particle conductance fully describe the transport properties at the linear response level, and they are not coupled to each other. When a net spin polarization is present, spin and particle transport are no longer independent from each other, and couplings already appear at the level of linear response.

Heat transport can be envisioned within the same framework, as illustrated in figure 2(b). Here we consider one spin component, and the two reservoirs have identical chemical potentials but different temperatures, which are apparent in

figure 2(b) from the different broadenings of the Fermi distributions. Again, reasoning energy by energy, we observe that a net current of particles is driven from the cold to the hot reservoirs for energies below the Fermi level, and vice-versa above it. Since transport is elastic in the conductor, these processes are responsible for carrying net energy or heat current from the hot to the cold reservoir.

There is a fundamental coupling of heat and particle current at the linear response level [85, 86]: following the sketch of figure 2(b), there is no reason *a priori* for the high-energy particle current above the Fermi level and the low-energy particle currents below it to cancel each other out. When the rate of transport in the conductor depends on the energy, which is typically the case, then a *thermoelectric* coupling arises, which is proportional to the derivative of the transport coefficients with energy[4].

In general, when two possible transport processes can take place simultaneously within one conductor, they are coupled to each other. Thermoelectricity is only one example of such a coupling. The linear response takes the form of an Onsager matrix with nonzero off-diagonal coefficients relating currents of extensive quantities to the generalized thermodynamic forces. Like for the simple case of particle transport, the two-terminal configuration directly implements these concepts, and suggests a practical route for experimental investigations.

1.4. Bosons and classical particles

Even though the concepts have so far been illustrated on the basis of Fermi gases, the general ideas of the two-terminal setup can be extended to other types of particles. The case of particles following Boltzman statistics, such as high-temperature cold atom gases, is very similar to that of Fermions. The range of energies to be considered in the transport process is determined by the mean internal energy of the particles and the temperature.

The case of low-temperature bosons is much more delicate, because of the emergence of the Bose–Einstein condensate. There, the reservoirs acquire a superfluid character, with properties that are not universal but depend, for example, on the interactions between the particles. In contrast with Fermions, the case of noninteracting bosons is pathological, and has little experimental relevance. The long-range phase coherence produces macroscopic interference, which renders the coupling from the reservoirs to the conductor sensitive to details of the geometry. The case of superfluid reservoirs is of particular relevance to cold atoms and will be treated in detail in section 5.

The particular case of the atom laser, derived from a Bose–Einstein condensate, but constituting a strongly nonequilibrium case with a highly monochromatic beam of particles, strongly resembles the case of Fermions with a low temperature but a large bias (one reservoir is the vacuum) [50, 51, 54]. Guided atom lasers are currently being used as sources for atom optics, giving access to quantities such as the

---

energy-dependent transmission coefficient for atoms in structures that are closely related to the transport coefficients in the Landauer configuration [52, 53], as explained in section 4.

2. Two-terminal configuration for cold atoms

The two-terminal formulation provides a natural framework for the study of transport processes in charge neutral systems such as cold atoms. We now describe the two-terminal transport setup that we operate in our group, which implements the principles exposed above. For concreteness, we will give precise numbers from our experimental setup, but most of the experimental techniques can be generalized, for example, to different atomic species or different platforms such as atom chips [87].

The concept shares some similarities with previously implemented techniques such as double-wells or ring traps in the context of Bose–Einstein condensates. These experiments will be discussed in section 5 in the wider context of superfluid transport with cold atoms. We only briefly describe the aspects of cold atomic gases that are not directly related to the transport experiments, referring the readers to general textbooks about this topic (for example [82]).

2.1. Cold lithium gas with tunable interactions

The preparation of quantum degenerate Fermi gases in our setup follows standard procedures developed in the field in recent years. Our apparatus is described in [88]. It produces a quantum degenerate Fermi gas consisting of about $N_\sigma = 10^5$ atoms in each of the two different hyperfine states labeled by σ, which play the role of a spin degree of freedom. We reach temperatures in the range of $T = 0.1T_F$ to $0.3T_F$, where $T_F = \hbar\bar{\omega}(6N_\sigma)^{1/3}$ is the Fermi temperature of the trapped gas. Here $\bar{\omega} = (\omega_x\omega_y\omega_z)^{1/3}$, where ω_i is the angular trap frequency in direction i.

In cases where there are no interactions, T_F coincides with the Fermi temperature of a homogenous system $\hbar^2/2m(6\pi^2 n_\sigma)^{2/3}$ with a density per spin component n_σ equal to the density of the trapped gas at the center. Importantly, in the presence of interactions, the total atom number is constant, hence T_F is constant even though the actual density of atoms varies. In general, there is thus no direct relation between T_F and the actual density of particles anywhere in the trap. Complementarily, certain situations require a description of the gas within the local density approximation where the local density of the gas at one point $\mathbf{r}$ in the cloud is associated with a local Fermi temperature $T_0(\mathbf{r}) = \hbar^2/2m(6\pi^2 n_\sigma(\mathbf{r}))^{\frac{2}{3}}$. T_0 and T_F can be deduced from each other using the equation of state of the gas.

The interactions between atoms in the same spin component are suppressed by Fermi statistics, and s-wave scattering occurs for pairs of atoms in different hyperfine states. This stems from the van der Waals force between atoms, and at the density and energy scales of cold atom experiments, the only relevant parameter is the scattering length a, which depends on the precise molecular structure of the two-atom problem.
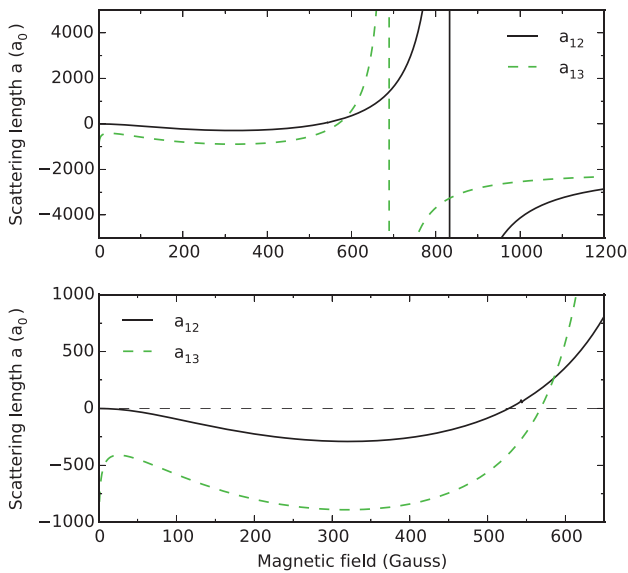
Figure 3. Feshbach resonances between two pairs of the $|1\rangle$, $|2\rangle$, $|3\rangle$ states of ^{6}Li, used in the experiments. (a) Scattering length as a function of magnetic field. (b) Zoom of (a) in the low magnetic field region to the left of the resonances.

The coupling between two atoms colliding in free space and a molecular channel leads to Feshbach resonances: the scattering length diverges upon tuning the energy of the molecular channel with respect to the scattering channel using a homogenous magnetic field. As a result, the scattering length is a control parameter that can be varied, keeping everything else equal over a wide range, up to the unitary limit reached on the resonance itself. More details on this phenomenon and the associated physics can be found in dedicated reviews, for example [89, 90].

The evolution of the scattering length of two Lithium atoms as a function of the magnetic field is presented in figure 3, based on the data of [91]. Depending on the situations, different mixtures of hyperfine states are used. In general, we found that the mixture of the lowest and third lowest hyperfine states (labeled 1 and 3) offers more flexibility in tuning the interactions while showing negligible losses, and our most recent measurements operate with this mixture. Otherwise a mixture of the first and second states (labeled 1 and 2) is used. Two operation regimes are used for the experiments: (i) the low or moderate interaction regime, at a low magnetic field, where the scattering length presents a local minimum and can be continuously tuned to zero, and (ii) the BEC-BCS crossover region which contains the unitary regime, where the system explores the strongly attractive regime, and becomes an s-wave superfluid at low temperatures [2, 4].

2.2. Trapping configuration

The configuration of traps used in the setup is presented in figure 4. It consists of (i) an optical dipole trap confining the atoms along the x and z directions and (ii) a magnetic field with a positive curvature providing a weak confinement along the y direction. The trapping frequency along y depends on
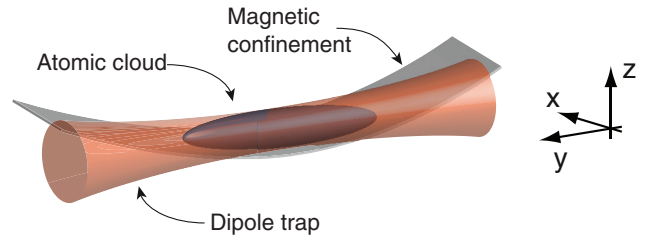

Figure 4. Trapping configuration. The dipole trap (red focused laser beam) creates the radial confinement, whereas the axial confinement (y direction) is created by the curvature of the Feshbach magnetic field.
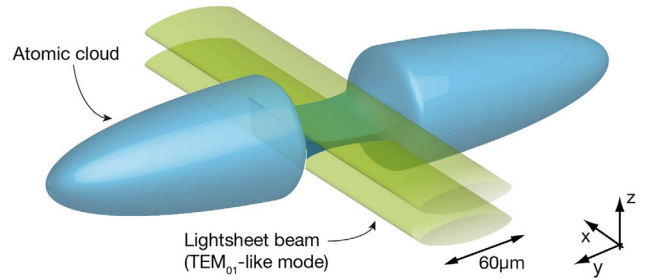

Figure 5. A blue-detuned TEM_{01}-like laser mode propagates along the x direction and is focused on the center of the cigar-shaped cloud. This defines a quasi-2D channel and two smoothly connected reservoirs.

the magnetic field and thus is slightly different between the weakly and strongly interacting regimes. The position of the minimum of the magnetic field is controlled by the addition of a magnetic field gradient.

This elongated cloud is the basis on which the two-terminal system is carved. To this end, a beam propagating along the x direction, having a nodal line oriented along y at its center, intersects the cloud, as presented in figure 5. This beam is produced using holographic techniques [92, 93] and approximates a TEM_{01} mode close to the center. Its wavelength is 532 nm, so that it expels atoms from the high intensity regions, thus creating a quasi-two-dimensional region at the center of the cloud. It has a waist of 30 μm in the y direction, which is much shorter than the size of the cloud (about 300 μm). The Gaussian nature of the beam ensures a smooth connection between the tightly confined region and the large, unperturbed regions at both sides. The number of atoms in the confined region is of the order of 10^3, which is very low compared to the population in the unperturbed regions at both sides. The separation of scales between the mesoscopic, tightly confined region and the large reservoirs consisting of large, unperturbed harmonic traps at both ends allows this system to be considered as a realization of the two-terminal configuration for transport.

The tightly confined region resides in the focal plane of two confocal microscope objectives [88]. This arrangement allows for the observation of the details of the atomic distributions. Furthermore, a wide range of potential landscapes can be projected onto the confined region, by sending light with a tailored intensity distribution through the microscopes. The high numerical aperture of the microscopes leads to potential
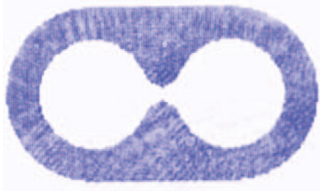
Figure 6. The potential pattern used to create an atomic capacitor, with two reservoirs connected by a channel. The transverse size of the channel is > 240 μm. The roughness in the potential distribution comes from optical imperfections. Reprinted by permission from Macmillan Publishers Ltd: [Scientific Reports] [94], Copyright (2013).

variations at the scale of micro-meter, which is the scale of the Fermi wavelength.

A conceptually similar system was realized at the same time for the classical atomic gases of laser-cooled atoms [94]. There, a cold atom cloud of ^{8}7Rb was trapped in a two-reservoir configuration produced using a spatial light modulator (SLM) producing a binary structure in the region of the atoms, as shown in figure 6. The use of an SLM provides a wide tenability for the structure, and the transverse size of the channel connecting the reservoirs was varied between 240 and 576 μm. The optical imperfections render the walls of the structure rough at the scale of 10 μm.

2.3. Initialization

In order to induce currents through the mesoscopic region, we introduce a bias between the two reservoirs. Three different procedures are used for the three kinds of biases used throughout our past experiments. These are summarized in figure 7.

2.3.1. Particle number imbalance.
A particle number difference between two reservoirs with the same geometry allows for the introduction of a chemical potential bias. Such a difference is produced by shifting the position of the center of the magnetic confinement along the transport direction (y), before the evaporation process, by applying an extra magnetic field gradient[5]. The subsequent evaporation produces a cold cloud with unequal populations, but with the same chemical potential, due to thermal equilibration during the evaporation process. Afterwards, a 'wall' beam is introduced, consisting of a blue detuned, elliptic beam creating a large repulsive potential barrier over the conductor, preventing any exchange between the reservoirs. The magnetic field gradient is then adiabatically reduced, restoring the symmetry between the geometry of the two reservoirs, but maintaining the population difference constant. The chemical potential bias can be finely adjusted by controlling the strength of the magnetic field gradient.

2.3.2. Temperature imbalance.
To introduce a temperature imbalance, a balanced situation with the same atom number and temperature is first produced, then a 'wall' beam, produced

using a blue detuned laser beam focused on the channel, is turned on, separating the two reservoirs. Another laser beam, which is red detuned from resonance, is then focused on one reservoir creating a perturbation. The power of this beam is then modulated at the frequency of the radial breathing mode of the cloud, thereby depositing energy into one reservoir by parametric heating. Controlling the duration and amplitude of the excitation allows for the precise adjustment of the heating.

2.3.3. Spin bias.
To create a spin bias, we build on a technique developed in [70]. One difficulty is that for the relevant cases where a high offset magnetic field is present, the different hyperfine components have the same magnetic moment. For weak magnetic field offsets, the densities and scattering lengths do not permit efficient evaporative cooling. We thus first produce a cold Fermi gas in a balanced mixture of states 1 and 2 at an offset field of 302 G, then ramp down the magnetic field to 52 G, where the spin components have different magnetic moments. A pulse of magnetic field gradient initiates the dipole oscillations, which have different frequencies due to the magnetic nature of the confinement along the transport direction. The dipole oscillations for the two components dephase with time, producing transiently a cloud centered in the trap but with finite displacement between the spin component. The oscillations are then abruptly interrupted by turning on a strong 'wall' beam, disconnecting the two sides of the cloud. The confinement at the center of the cloud is then ramped up together with the other beams producing the potential landscape in the conductor, and the offset field is ramped up to high values again. Atoms in state 2 are transferred to state 3 using a high efficiency Landau–Zener radio-frequency sweep. Finally, an extra step of evaporative cooling brings the reservoirs down to low temperatures allowing for superfluidity [25].

2.4. Transport measurements

Transport measurements are initiated by removing the 'wall' beam separating the reservoirs, which allows the reservoirs to exchange particles through the conductor. After an evolution time t, the wall beam is abruptly turned back on, and the laser beams producing the confinement in the conductor and the potential structures are adiabatically turned down. This turns the reservoirs into half-harmonic traps, where the atom number and temperatures can be estimated using the time-of-flight technique applied to the transverse direction.

In order to extract the conductance from the time evolution of the atom number in the two reservoirs, we make use of a simple linear resistor-capacitor (RC) model. This model captures the essential features of the measurements, and is very helpful for disentangling the effects that genuinely originate from transport from those reflecting the thermodynamics of the reservoirs. We introduce it here for the simple case of particle transport. The cases of heat and spin transport will be covered in dedicated sections below.

Consider two arbitrarily shaped atomic reservoirs connected by a channel characterized solely by its conductance G. It may have any dimension and an arbitrary shape, and the

---

[5] Note that in the relevant regimes where a large offset magnetic field is present, all hyperfine states have the same magnetic moment. Thus, the magnetic field gradient only couples to the density.
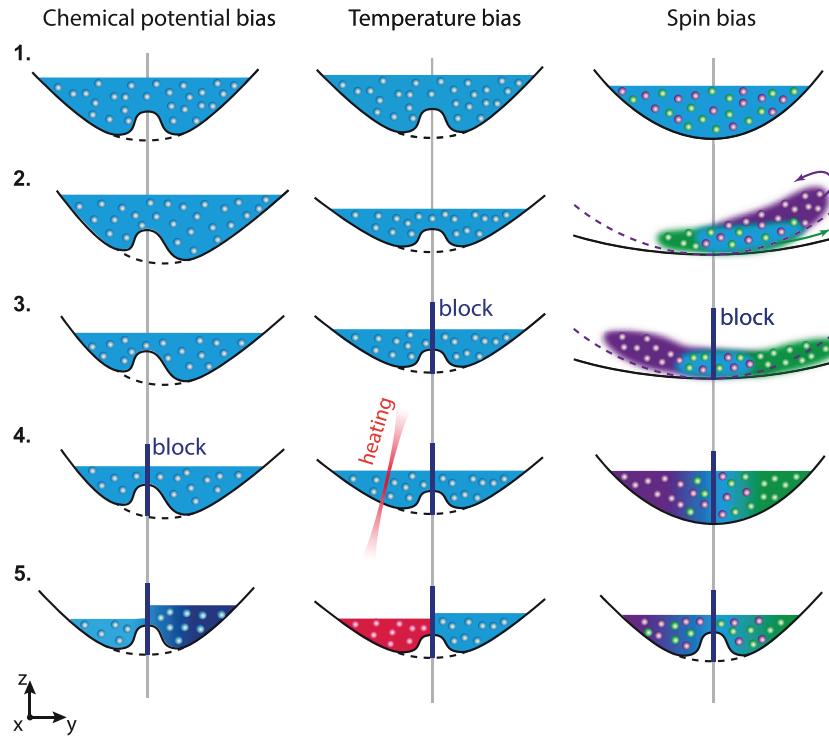
Figure 7. Biasing the reservoirs. The solid line represents the potential landscape combining a large parabolic trap and an extra confinement at the center; the level of the blue color represents the chemical potential. Left: creation of a chemical potential bias; middle: creation of a temperature bias; right: creation of a spin bias.

only requirement should be that it contains a negligible atom number compared to the reservoirs. This condition implies that G is low enough not to place the reservoirs out of equilibrium by emptying the reservoirs too fast. At equilibrium the reservoirs have the same chemical potential μ_0, but may contain, in general, a different number of atoms, $N_{L,0}$ and $N_{R,0}$, as sketched in figure 8(a). Imagine that we shuffle $\Delta\tilde{N}/2$ atoms from reservoir R to reservoir L, i.e.

$$N_L = N_{L,0} + \Delta\tilde{N}/2 \qquad (1)$$

$$N_R = N_{R,0} - \Delta\tilde{N}/2. \qquad (2)$$

This will change the chemical potential in each of the reservoirs to

$$\mu_{L(R)} = \mu_0 + \Delta\mu_{L(R)}. \qquad (3)$$

The changes in chemical potential can be expressed in linear response in terms of the compressibilities $C_{L(R)} = \partial N_{L(R)}/\partial \mu_{L(R)}$ of the reservoirs:

$$\Delta\mu_L = \frac{1}{C_L}\frac{\Delta\tilde{N}}{2} \qquad (4)$$

$$\Delta\mu_R = -\frac{1}{C_R}\frac{\Delta\tilde{N}}{2}. \qquad (5)$$

The difference in chemical potential or the chemical potential bias $\Delta\mu = \mu_L - \mu_R$ is thus given by

$$\Delta\mu = \left(\frac{1}{C_L} + \frac{1}{C_R}\right)\frac{\Delta\tilde{N}}{2} = \frac{1}{C_{eff}}\frac{\Delta\tilde{N}}{2}, \qquad (6)$$

where we have introduced an effective compressibility C_{eff}. To get the dynamics of the system we differentiate equation (6) with respect to time obtaining

$$\frac{d}{dt}\Delta\mu = \frac{1}{C_{eff}}\frac{d}{dt}\frac{\Delta\tilde{N}}{2} = -\frac{1}{C_{eff}}I = -\frac{G}{C_{eff}}\Delta\mu, \qquad (7)$$

where we used of the definition of the current $I = -\frac{d}{dt}\frac{\Delta\tilde{N}}{2}$, which is positive when the particle flow goes from reservoir L to reservoir R. Since we assumed linear response, $\Delta\mu$ is linearly related to $\Delta\tilde{N}$ by equation (6) and we obtain the same differential equation for $\Delta\tilde{N}$:

$$\frac{d}{dt}\Delta\tilde{N} = -\frac{G}{C_{eff}}\Delta\tilde{N}. \qquad (8)$$

The solution of equations (7) and (8) with the initial condition $\Delta\mu(t=0) = \Delta\mu_{ini}$ and $\Delta\tilde{N}(t=0) = \Delta\tilde{N}_{ini} \ (= 2C_{eff}\Delta\mu_{ini})$ is an exponential decay of the chemical potential bias or particle number imbalance as a function of time,

$$\Delta\mu(t) = \Delta\mu_{ini} \exp(-t/\tau) \qquad (9)$$

$$\Delta\tilde{N}(t) = \Delta\tilde{N}_{ini} \exp(-t/\tau), \qquad (10)$$

with a time constant $\tau = C_{eff}/G$. This is analogous to the discharge of a capacitor, having a capacitance $C_{eff} = \partial Q/\partial U$, through a resistor $R = 1/G$: the chemical potential difference $\Delta\mu$ is the analog of the voltage U across the capacitor and $\Delta\tilde{N}/2$ corresponds to the charge Q on the capacitor. More precisely, the capacitor corresponding to C_{eff} can be thought of as two capacitors in series, one corresponding to C_L and the other to C_R. The corresponding RC circuit is drawn in figure 8(b).
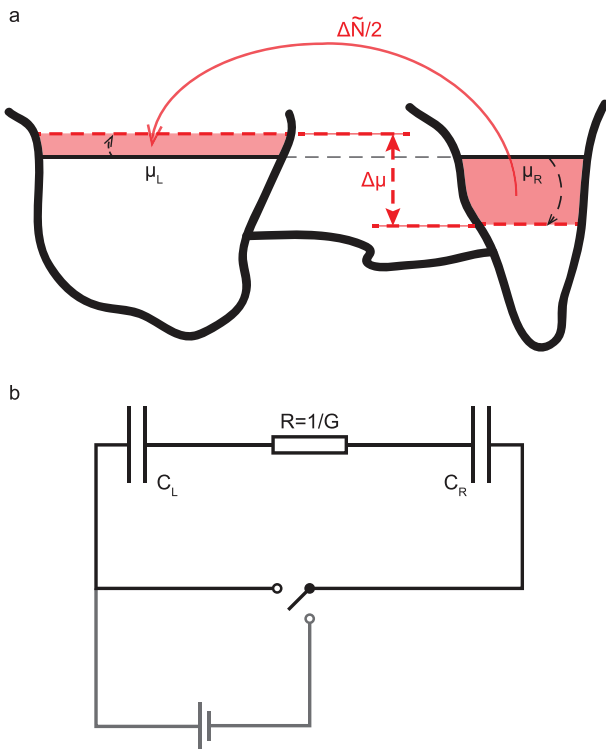
Figure 8. Generic two-terminal model. (a) Two reservoirs of different size and shape are connected by a transport channel. Upon transfer of $\Delta\tilde{N}/2$ particles from the right to the left reservoirs, a chemical potential bias $\Delta\mu$ arises. (b) The corresponding RC circuit: the left and right reservoir are represented each by a capacitor, with a capacitance C_L and C_L. They can be charged by moving the switch to the vertical position. A discharge through the resistor R is initiated by moving the switch to the horizontal position.

In the experiment, we rather measure the total atom number difference between both reservoirs

$$\Delta N = N_L - N_R = (N_{L,0} - N_{R,0}) + \Delta\tilde{N} = \Delta N_0 + \Delta\tilde{N}, \tag{11}$$

where ΔN_0 is the difference in atom number between the two reservoirs at equilibrium. Typically, $\Delta N_0/(N_L + N_R)$ is at the few per cent level and depends on the precise alignment of the channel with respect to the cigar-shaped cloud.

Using expression (11) in equation (10) we obtain the time evolution of ΔN,

$$\Delta N(t) = \Delta N_0 + \Delta\tilde{N}_{ini} \exp(-t/\tau). \tag{12}$$

This simple reasoning requires the following important remarks. First, the hypothesis underlying the reasoning is that the reservoirs maintain their internal equilibrium at each point in time, as necessary for the validity of the Landauer approach. In our experiment, this is ensured by the separation of length scales between large reservoirs and a small conductor. Currents through the conductor are weak enough for the corresponding perturbation on the reservoirs to be small. In particular, we operate in the regime where $\omega\tau \gg 1$, where ω is the typical trap frequency of the reservoirs, such that the current does not couple to the internal excitation modes of the reservoirs.

Second, the quantity which is experimentally accessible without any further assumption is the timescale τ, corresponding to the exponential decay of the initial perturbation. Such an exponential decay is typical for many cold atom experiments where dynamics following a quench is measured. The important difference introduced by operating with reservoirs connected to a mesoscopic system is that τ can now be decomposed into two contributions: a thermodynamic contribution—the compressibility—and a genuine transport coefficient G. In situations where a global relaxation of the system is observed, transport and thermodynamics occur at the same time and length scales, preventing the study of transport independently of the static properties.

Third, in our mesoscopic approach, the compressibility is a property of the reservoirs only. Thus, the conductance can be directly studied, either by just modifying the conductor and comparing the subsequent evolution of τ, or by directly modeling the reservoirs and calculating C_{eff}, allowing for the extraction of G. For noninteracting gases, accurate modeling of the reservoirs is available for any temperature and spin polarization, provided the shape of the potentials is known. For interacting gases, recent experiments have provided high-precision measurements of the equation of state of the homogenous Fermi gas [95–99], which can be used as an input to estimate G. For cases not covered by these measurements, one can rely on theoretical calculations, but without an experimental benchmark they can have systematic errors, which may be hard to estimate—in particular with strong interactions.

Fourth, the exponential decay of the initial imbalance is a direct consequence of the linear response hypothesis. Deviations from an exponential decay directly indicate the breakdown of linear response, which can be tracked down to a nonlinear current-bias relation. This is particularly expected for superfluids [24, 25]; see section 6.1.

In this reasoning, it is supposed that the currents are weak enough for no inductive effects to have to be taken into account. These typically arise due to the finite mass of the particles: the potential or interaction energy stored in the capacitive element can also be converted and stored in the form of the kinetic energy of the atoms. This is best illustrated by the trivial limiting case where the channel is absent. One is then left with a harmonic trap where an initial imbalance triggers undamped dipole oscillations. The parasitic inductance only makes a significant contribution when the relaxation timescale is comparable to or lower than the trap frequency along the transport direction. A possible model in this case is the RLC circuit, which was put forward in [94], where explicit expressions were derived for inductive terms. These effects are important in the case of superfluids where large currents can be driven, even through narrow channels.

The period of dipole oscillations is also a lower bound on the thermalization timescale of the reservoirs. As a result, in the presence of large currents the reservoirs cannot be considered at equilibrium at each point in time: among other issues, the instantaneous chemical potential ceases to have any meaning and the capacitive effect of the reservoirs is not given by the equilibrium compressibility anymore.

3. Transport in the multimode regime

We now examine transport experiments with weakly interacting Fermions, where the concepts described in the previous section are used to investigate ballistic and diffusive transport [18, 20]. This section is dedicated to experiments where transport takes place in a regime of weak transverse confinement in the channel, such that the transverse size of the channel is larger than the Fermi wavelength, or equivalently the Fermi energy is larger than the trap frequencies. In this case, the quantization of the motion of atoms along the transverse direction of the conductor does not play a strong role. These experiments have provided the first proof of principle for the two-terminal approach in cold atomic gases, demonstrating the potential of the technique. They are also used as a benchmark for the more intricate experimental situations explored in later sections.

3.1. Conduction

The two-terminal transport experiments reported in [18] were performed with Fermi gases at a scattering length of -145 a_0, in the weakly interacting regime and at a temperature of $0.36(18) T_F$. The estimated mean free path for interparticle collisions was $\simeq 1.3$ mm, which is larger than the typical size of the cloud ($\sim 300\ \mu$m). The collision rate in the reservoirs was estimated to be $\simeq 30$ ms, ensuring thermalization at this timescale[6].

In these experiments, the channel is defined solely by the tight vertical confinement of the TEM_{01}-like mode. The frequency along this direction was at most 3.9 kHz, which is lower than the temperature and the Fermi temperature, such that even along the tightly confined direction, several quantum mechanical modes are populated. The resulting transport thus takes place in a quasi-classical regime.

The decay of the initially prepared imbalance was observed to be exponential, as shown in figure 9(A), in agreement with the linear response hypothesis. The decay time τ is 170(14) ms, which is larger than the collision rate in the reservoirs, and much larger than the trap frequencies in the reservoirs, such that the decomposition of τ into reservoir compressibility and conductance for the channel is justified. Extracting the derivative of the decay curve at each point in time, using a linear fit to successive points, yields a set of measured currents, with the corresponding average particle number difference. The resulting data is presented in figure 9(B), representing the first observation of Ohm's law with cold atomic gases.

The microscopic origin of resistance in the case of ballistic transport is the highly restricted phase space available in the contact compared to the reservoirs, such that most of the atoms impinging on the channel are actually reflected elastically. This can be put on formal ground using the Landauer formalism, which will be presented in the next section. A consequence of the ballistic nature of transport in the channel is
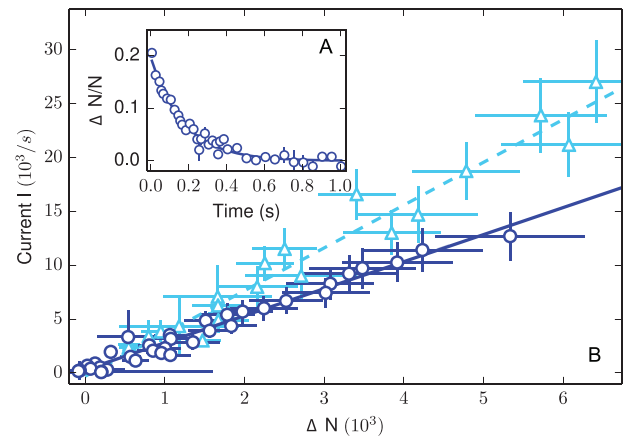
Figure 9. Observation of ohmic conduction. (A) The measured number difference between the two reservoirs as a function of time. The solid line is an exponential fit to the data. (B) The current as a function of the number difference between the two reservoirs, measured from the exponential fit of panel A, for two different confinements in the channel. A small offset obtained from the fits in panel A, which is due to a slight misalignment of the channel with respect to the center of the trap, has been subtracted. Circles: the maximum center frequency along z set to 3.9 kHz, triangles: 3.2 kHz. The lines are linear fits to the data. Figure adapted from [18]. Reprinted with permission from AAAS.

that the density inside it in the presence of a DC current is uniform. Thus, the variations of densities in the presence of the current are concentrated at the contacts between the channel and the reservoirs [100].

Absorption imaging was used in order to observe the density distribution across the channel in the presence of a current. Such a picture is shown in figure 10(A), where the two reservoirs can be seen on both sides of a low-density region of the channel. In the presence of a chemical potential difference between the reservoirs driving a current though the channel, the density distribution is slightly modified. The difference between the density distributions in the presence and in the absence of a current is shown in figure 10(B). Integration along the direction transverse to the channel yields a line density difference shown in figure 10(C). The plateau at zero, which is centered on the channel, demonstrates its ballistic character, while the drop in density is concentrated at the contacts.

These observations were repeated with a channel on which a strong disorder was imposed, using the potential induced by a laser speckle pattern [6]. The confinement along the vertical direction was reduced in order for the disordered channel to exhibit the same conductance as the ballistic one (the same bias applied to the reservoirs produced the same current). The corresponding line-density difference along the channel is shown in blue in figure 10(C), showing a linear decrease in density across the channel, as expected for a diffusive system.

The distribution of the density difference across the channel contains information about the local transport properties, such as mobility or resistivity. An important difficulty, however, lies in the nonequilibrium nature of the transport phenomena, preventing the unambiguous attribution of a chemical potential to a region of space from knowledge of the density. In the case of charged particles, this can be circumvented by referring to a

---

[6] In this experiment, no 'wall' beam was used to separate the clouds, but the slow timescale of transport compared to the switch-off time of the magnetic field gradient was used instead to initialize the transport.
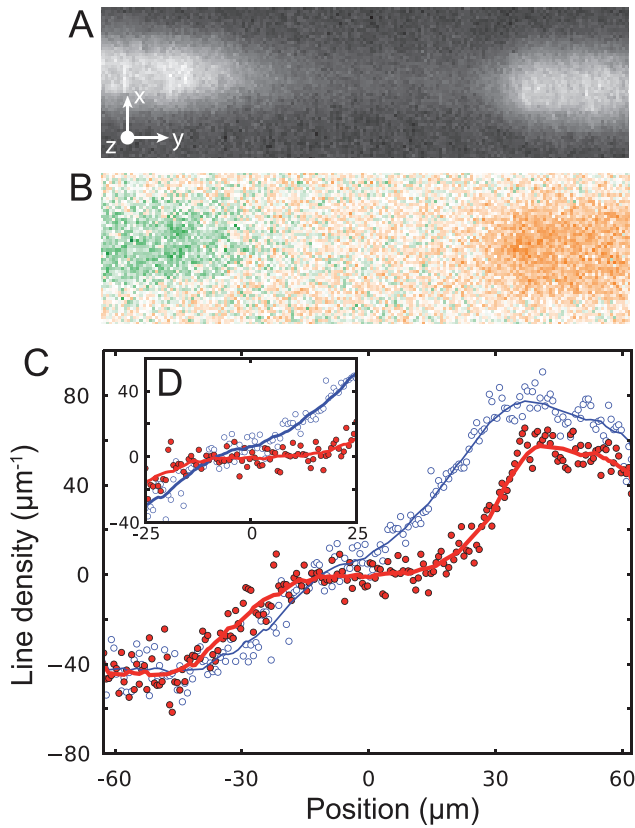
Figure 10. Investigation of ballistic and diffusive conduction using high-resolution imaging. (A) The absorption picture of the density in the channel, for a cloud at equilibrium (no current). (B) The difference between two pictures taken at equilibrium and with a current of $10^4 \, \mathrm{s}^{-1}$. The color is orange for a positive difference and green for negative. (C) The line-density difference obtained by accumulating B along the x-axis, for a ballistic channel (red full circles) and for a diffusive channel with the same conductance (blue open circles), in the presence of the same current. The solid lines are smoothed data to guide the eye. (D) Focus on the central part of the line density difference. Figure adapted from [18]. Reprinted with permission from AAAS.

local value of the electrical potential, which can always be well defined by solving Maxwell's equations, and connects to the chemical potential at equilibrium. For neutral particles, the distribution is not coupled to any field and thus cannot be related to a potential unless local equilibrium is achieved. A pragmatic solution suggested in [100] and used in [18] is to attribute a chemical potential to a point which would be required to achieve the corresponding density at equilibrium. This gives a meaning to the question 'where does the chemical potential drop?' However, one should keep in mind that this refers to a fictitious equilibrium situation, which is not the one actually realized in the experiments. Measurements in condensed matter systems have actually shown that the distribution is a long way from thermal inside a driven conductor [101, 102].

3.2. Thermoelectric effects

As the cold atoms are isolated from the environment, the energy is strictly conserved throughout the entire transport measurement. This gives an opportunity to investigate heat

transport in a situation where energy can only be carried from one reservoir to the other via particle exchange, in contrast to solid materials where phonons and other excitations can contribute. In addition, the direct imaging of the momentum distribution in the reservoirs gives direct access to the total entropy during the transport process and permits us to keep track of entropy exchange and creation, thus allowing the reversible processes to be isolated from the irreversible ones. These rather unique conditions are ideal test beds for the fundamental principles of thermoelectricity, and more generally heat engines, with a quantitative comparison that is possible with a microscopic theory.

In the quasi-classical regime with weakly interacting particles, the measurements of heat transport and thermoelectric power were performed and reported in [20] using the two-terminal configuration. The theoretical description parallels that of particle transport, except that the linear response relations take matrix forms with off-diagonal coefficients describing the coupling between heat and particle currents and the temperature and chemical potential bias.

The linear response transport is described within the linear response by the 'Onsager' matrix, connecting currents of extensive quantities to the gradients of the thermodynamically conjugated quantities:

$$\begin{pmatrix} I_N \\ I_S \end{pmatrix} = -G \begin{pmatrix} 1 & \alpha_{ch} \\ \alpha_{ch} & L + \alpha_{ch}^2 \end{pmatrix} \begin{pmatrix} \mu_c - \mu_h \\ T_c - T_h \end{pmatrix}. \tag{13}$$

where I_N and I_S are the particle and entropy currents, T_h, μ_h and T_c, μ_c refer to the temperature and chemical potentials of the hot and cold reservoirs respectively, and $\bar{T} = (T_h + T_c)/2$. G is the particle conductance, $L = \frac{G_T}{\bar{T}G}$ is the Lorenz number with G_T as the heat conductance, and α_{ch} is the thermopower of the channel. The symmetric nature of the matrix is a consequence of Onsager's relations [85].

Note that we formulate the problem in terms of the entropy currents rather than energy currents. The final results are the same but the use of entropy provides a more direct distinction between reversible and irreversible processes, which are of fundamental interest in assessing the thermodynamic efficiency [103].

Similarly, the reservoirs are characterized by a 'Maxwell' matrix, which is symmetric by virtue of the Maxwell relations

$$\begin{pmatrix} \Delta N \\ \Delta S \end{pmatrix} = \begin{pmatrix} \kappa & \kappa \alpha_r \\ \kappa \alpha_r & \frac{C_\mu}{T} \end{pmatrix} \begin{pmatrix} \Delta \mu \\ \Delta T \end{pmatrix}, \tag{14}$$

with $\kappa = \frac{\partial N}{\partial \mu}\big|_T$, $\alpha_r = \frac{\partial S}{\partial N}\big|_T = -\frac{\partial \mu}{\partial T}\big|_N$, $C_\mu = T \frac{\partial S}{\partial T}\big|_\mu$ as the compressibility, dilatation coefficient and specific heat of each reservoir respectively. Furthermore, we have written $\Delta \mu = \mu_c - \mu_h$ and $\Delta T = T_c - T_h$; all thermodynamic quantities are evaluated at the average temperature $\bar{T}$ and particle number $(N_c + N_h)/2$.

A reasoning similar to that of equation (8) yields the time evolution of the populations and temperatures of the reservoirs:
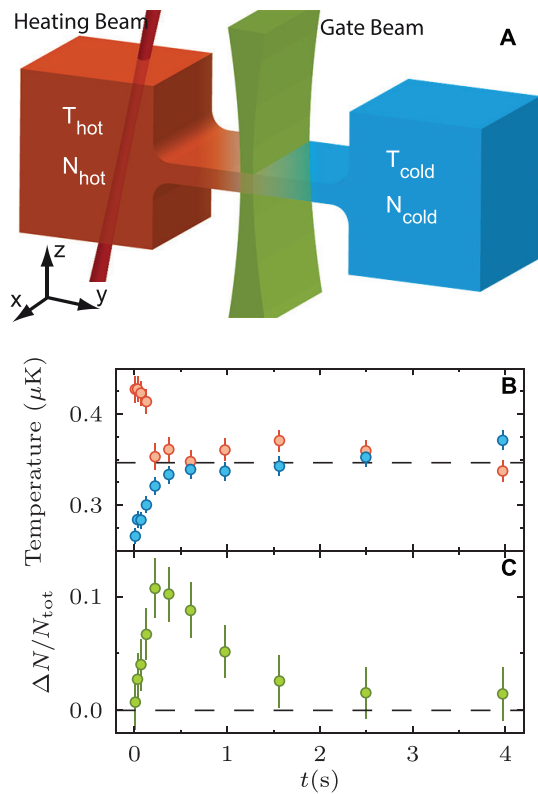
Figure 11. Thermoelectric transport experiment. (A): A quasi-two-dimensional channel connects two atomic reservoirs. A gate beam intersects with the channel and blocks particle and heat transport. A heating beam traverses the left reservoir and heats it in a controlled way. (B): T_h (red) and T_c (blue) as a function of time. Dashed line: $\bar{T}$ at the initial time. (C): $\Delta N/N_{tot}$ as a function of time. In the channel ν_z was set to 3.5 kHz with a disorder of average strength 542 nK (see text). Figure adapted from [20]. Reprinted with permission from AAAS.

$$\tau_0 \frac{\mathrm{d}}{\mathrm{d}t}\begin{pmatrix}\Delta N \\ \Delta T\end{pmatrix} = -\begin{pmatrix} 1 & -\kappa(\alpha_r - \alpha_{\mathrm{ch}}) \\ -\dfrac{\alpha_r - \alpha_{\mathrm{ch}}}{\ell\kappa} & \dfrac{L + (\alpha_r - \alpha_{\mathrm{ch}})^2}{\ell} \end{pmatrix}\begin{pmatrix}\Delta N \\ \Delta T\end{pmatrix}. \quad (15)$$

Here, $\ell = \frac{C_N}{\kappa\bar{T}}$ is an analog of the Lorenz number for the reservoirs, measuring the relative magnitude of the thermal fluctuations of entropy and atom number, and $\tau_0 = \kappa G^{-1}$ is the particle transport timescale identical to the decay constant for particle transport.

The experiments were performed in conditions similar to those of the previous section. Transport is initialized by introducing a temperature bias between the reservoirs, using a laser focused on one of the reservoirs, which is modulated to induce parametric heating, as depicted in figure 11(A). The subsequent evolution of the particle number and temperature in the reservoirs after various evolution times is presented in figures 11(B) and (C). It should be noted that measuring the temperatures separately in the two reservoirs is much more challenging than evaluating the atom numbers, and these experiments can only be performed at moderate temperatures where the atom numbers are large in each reservoir, and the signal to noise ratio for fitting the cloud profiles is not strongly reduced by Fermi statistics [104].

Temperatures in these reservoirs converge exponentially, reflecting the heat transport between them in a manner which is similar to particle transport in a simple RC model. That the convergence temperature is equal to the average of the initial temperatures of the reservoirs is a further indication that despite the large temperature difference, the evolution is still within the linear response. The atom number imbalance, initially zero, first increases linearly and then decreases back to zero. This transient effect represents the thermoelectric response of the system.

As highlighted in the previous sections, the response is a combination of two factors: the thermodynamic response of the reservoirs and the transport response from the channel. This is crucial in the context of thermoelectricity. Here, the thermodynamic part leads to a decrease of the chemical potential with increasing temperature at a fixed particle number, as is well known in cold atom physics. This leads to a temperature-induced chemical potential bias, which induces a particle current. This effect has nothing to do with thermoelectric effects; it would be present even with a purely diagonal Onsager matrix.

The genuine thermoelectric response of the system, contained in the off-diagonal elements of the Onsager matrix, creates an additional contribution to transport which depends on the details of the channel geometry. In the experiments of [20], it turns out to be positive, i.e. directed from a high temperature to a low temperature. As a result, the thermoelectric and thermodynamic contributions compete with each other. The positive current in figure 11(C) indicates that the thermoelectric effects dominate.

An important consequence of this particular combination is that the current is driven from the low chemical potential reservoir to the high chemical potential reservoir, i.e. against the bias. In other words, the channel operates like a heat engine, generating work in the form of current flowing against the bias out of the connection of a hot and cold reservoir. Because of its isolated nature, the engine is not able to perform cycles since the heat inserted into the reservoir remains in the system. However, the cycle is closed up to a global increase of temperature, as analyzed in [20].

The strength of the thermoelectric response was quantified experimentally using a figure of merit $\mathcal{R} = (\Delta N/N_{\mathrm{tot}})/(\Delta T_0/T_{\mathrm{F}})$, with ΔT_0 as the initial temperature imbalance. Upon increasing the confinement in the channel, the thermoelectric response and the time scale τ characterizing the particle transport increases.

The experiments were repeated in the presence of disorder in the channel, where transport crosses over from ballistic to diffusive. Also in this case, the transport timescale and thermoelectric response were seen to increase together. The thermoelectric response is presented in figure 12 as a function of the measured τ for both the ballistic and diffusive cases. Interestingly, for a given τ, i.e. for a given resistance of the channel, the disordered channel is seen to have a much higher thermoelectric response—up to three times higher than the ballistic channel.

The physical reason is the much stronger dependence on energy of the rate of particle transport across the channel,
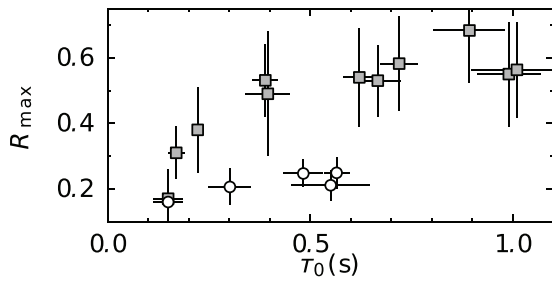
Figure 12. Thermoelectricity in the ballistic to diffusive crossover. $\mathcal{R}_{max}$ versus timescale τ_0 for the diffusive (gray squares) and ballistic case (open circles). Figure adapted from [20]. Reprinted with permission from AAAS.

compared to ballistic transport. In the ballistic case, the dependence in energy comes from the variations in density of the modes with energy. In the case of disordered channels, transport typically proceeds by random walks, modified by the wave nature of matter. Typical distributions of the random potential, like the speckle patterns used in most experiments with cold atoms, yield mean free paths that have very strong energy dependance. These variations lead to a strong asymmetry around the Fermi level between high-energy particles predominantly emitted by the hot reservoir and low-energy particles emitted by the cold one (or equivalently between particles and holes), leading to enhanced thermoelectric response [105].

A theoretical model for the reservoirs and channel was used in [20] in order to extract the transport coefficients from the time evolution of temperatures and atom number differences. For the case of ballistic transport, good agreement was found between the predications, based on the Landauer theory, ideal gas thermodynamics and the observations. The case of a disordered channel was modeled using a heuristic interpolation formula, allowing us to describe the crossover from ballistic to diffusive [100]. To model the diffusive transport, a power law dependance of the scattering time on the disorder strength was fitted to the data, showing good agreement.

The microscopic understanding of the transport of cold atoms in realistic speckle potentials is a topic on its own, far beyond the specific case of two-terminal transport (see [106] for a systematic treatment). We only point out the fact that the energy dependence of the transport properties is a general feature of disordered systems, which is likely to be key for the interpretation of the new generation of experiments studying high-temperature transport in closed systems [107].

In the same spirit, the coupling of spin and heat transport in Fermi gases was analyzed theoretically [108, 109] following the spin diffusion experiments [70, 110]. By introducing a spin polarization in a Fermi gas, one creates an energy mismatch between the Fermi surfaces of the minority and majority populations. As polarization gradients or temperature differences are introduced, currents of heat or spin arise as a result of the differential relaxation of the high-energy atoms with respect to the low-energy ones, similarly to the thermoelectric effects described above. As interactions are varied in the vicinity of the Feshbach resonance, the interaction cross section between the two spin components changes from hardcore, energy insensitive in the weakly interacting limit to unitary with an

inverse square dependence on momentum. This yields qualitative changes in the spin-Seebeck coefficients. [108, 109].

The operation of the channel as a heat engine, evidenced by the driving of currents against the chemical potential bias, provides perspectives for the use of transport in order to cool down Fermi gases, using the Peltier effect. This was theoretically investigated in detail in [111]. The idea is to design a channel that can filter out some classes of energy, i.e. having a peaked transmission as a function of energy. By biasing the channel with a well-chosen energy transmission band it is possible to inject low-entropy atoms into one of the reservoirs in order to 'rectify' the energy distribution and lower the entropy per particle. Importantly, it was shown that this process is intrinsically more efficient than plain evaporative cooling—especially in the degenerate regime—raising exciting perspectives for quantum simulation in the low-temperature regime with Fermi gases. More details on possible applications are described in the recent review [112]. The strong energy dependence of the density of states is also a feature of BCS superfluids. The thermoelectric effect in these systems is a topic of general interest in condensed matter, and the case of superfluid Fermi gases in the two-terminal configuration was recently investigated theoretically [113].

The operation of complete heat engines with cold atoms, and more recently with individual trapped ions [114], opens the perspective for a fundamental understanding of thermodynamics at the quantum level—in particular, the exploration of the microscopic origins of irreversibility and the operation of quantum-enhanced heat engines [115].

4. Single-mode regime and quantum point contacts

In the experiments presented in the previous section, the energy scales of temperature and bias are large compared to the spacing between the transverse modes in the channel, such that the quantization of motion was not relevant. Most traps for atomic gases operate in this regime, where the trapping frequencies are much smaller than the chemical potential, so that the chemical potential can be treated in the local density approximation. This corresponds to a situation in which the de Broglie wavelength of particles, or healing length for superfluids, is much smaller than the length scales of the potential variations [116]. To study quantum gases in low dimensions, atomic ensembles were strongly confined along one or two directions, such that the respective trapping frequencies exceeded the chemical potential and temperature. The properties of these low-dimensional gases were indeed found to strongly deviate from their three-dimensional counterparts [2, 117].

As far as transport is concerned, the regime where confinement in the channel is large enough to separate transverse vibrational states on the relevant energy scale is of fundamental importance, both as a conceptually simple case, and also because of the phenomena observed in various solid-state physics experiments. Prominent examples are the quantum Hall effect—where the one-dimensional character arises from the edge state [1]—and the quantized conductance observed
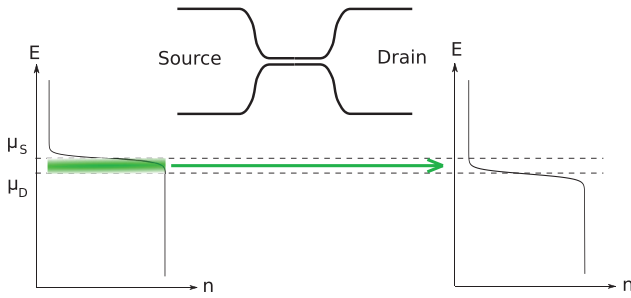
Figure 13. Two-terminal Landauer configuration. Source and drain reservoirs are contacted by a ballistic one-dimensional channel. A chemical potential difference is introduced between them, and a net current of particles is driven from the source as a result of the excess of particles above the Fermi level of the drain.

in quantum point contacts. However, the concept of two-terminal transport still requires reservoirs which in most cases are two- or three-dimensional[7]. The investigation of transport in low-dimensional conductors thus leads naturally to the realization of a *hybrid* dimensional system, with different parts of the system having different dimensionality. To our knowledge, such systems have not been considered in cold atoms. More generally, this provides an example of the type of physics that emerges from a device approach to quantum gases, where interfaces are a central topic. The particular case of the dimensional crossover at the reservoir-conductor interface in cold atoms has been very recently theoretically analyzed [120].

In this section, we introduce the Landauer theory of conductance quantization in tightly confined conductors, with an emphasis on the physical hypothesis and their relation to cold atom experiments, and derive the quantization of conductance. We then describe in detail the experimental observation of this phenomenon with cold gases and perspectives for future studies.

4.1. Landauer formula

The derivation of the Landauer formula, as presented in many standard textbooks and reviews of mesoscopic physics [1, 100, 121], can be directly adapted to atomic systems. In short, consider the situation depicted in figure 13. A one-dimensional system is connected smoothly to large particle reservoirs described by the Fermi–Dirac distributions $f(\mu_i, T)$, where μ_i is the chemical potential of the reservoir i, $i = L, R$ and T is temperature.

Because the channel is ballistic, the atoms traveling through it with positive (respectively negative) momentum follow the energy distribution in the left (respectively right) reservoir. The total current inside the channel thus reads

$$I = \int d\epsilon v(\epsilon) g(\epsilon)(f(\epsilon; \mu_L, T) - f(\epsilon; \mu_R, T)) \qquad (16)$$

---

[7] While this is de facto the case for condensed matter systems connected to leads, cold gases could in principle realize purely one-dimensional reservoirs without being connected to higher dimensional systems. This case would deserve particular treatment as most of the properties expected from reservoirs in the Landauer formulation are questionable in one dimension—in particular, the ability to efficiently reach thermal equilibrium [118, 119].

with $v(\epsilon)$ being the group velocity and $g(\epsilon)$ the density of states. In one dimension, $g(\epsilon) = 1/hv(\epsilon)$ and the two terms cancel, leaving

$$I = \frac{1}{h} \int (f(\epsilon; \mu_L, T) - f(\epsilon; \mu_R, T)) d\epsilon \qquad (17)$$

where h is Planck's constant. The formula reduces to $I = \Delta\mu/h$ with $\Delta\mu = \mu_L - \mu_R$ in the low-temperature linear response limit. Thus, the conductance is equal to one over Planck's constant.

It may seem at first sight that the exact cancellation of the group velocity with the density of states in one dimension is a fortuitous effect that could be disturbed by many experimental imperfections. This is not the case, however, as can be seen from the following argument [122, 123]. Consider the Fermi distributions in the two reservoirs, as depicted in figure 13. As mentioned in the first section, at low temperature the net current originates from the particles populating the energy states between μ_L and μ_R. Let us operate a unitary change of basis for these states and consider their representation in the time domain. Fourier transforming the square window in energy leads to a discrete set of wavelets with a *sinc* shape, and separated in time by $\Delta t = h/(\mu_L - \mu_R)$. This is nothing but a statement of the Heisenberg principle. Consider now the zero temperature limit, where all these energy states in the left reservoirs are populated by one and only one particle, as required by Fermi–Dirac statistics. Then, after the unitary transformation to the time domain, each wavelet carries one and only one particle. Counting now the number of particles per unit time gives rise to the net current and we directly obtain the Landauer result $I = 1/\Delta t = (\mu_L - \mu_R)/h$.

The case where several modes can independently contribute to transport is a straightforward extension, where a sum over the transverse modes has to be added to the reasoning. Each mode contributes to the transport by the same amount, provided it is energetically accessible. As a result, the expected conductance at low temperature is N/h, where $N = \sum_n \theta(\mu - E_n)$ is the number of transverse modes which is energetically accessible, μ is the average chemical potential of the reservoirs, θ is the step function and E_n is the energy of the mode n, obtained by solving Schrödinger's equation in the transverse directions in the channel.

In the presence of an obstacle in the channel capable of reflecting particles, the formula for the current includes the energy-dependent intensity transmission coefficient $t(\epsilon)$:

$$I = \frac{1}{h} \int t(\epsilon)(f(\epsilon; \mu_L, T) - f(\epsilon; \mu_R, T)) d\epsilon. \qquad (18)$$

For charge currents measured in ampere and bias measured in volts, an overall charge factor e appears in front of the current and the bias reads $\Delta\mu = -eV$, where V is the voltage. This merely represents a choice of units (voltage for the bias and amperes for the current), which yields a conductance quantum of e^2/h. A factor of two for spin degeneracy is usually also included, since conductance measurements in condensed matter physics are not spin-resolved. In contrast, measurements based on optical imaging with atomic gases are
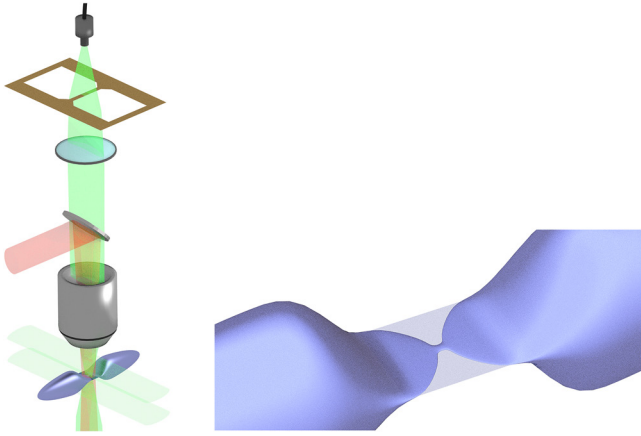
Figure 14. Quantum point contact. Left: schematic of the experimental setup. A binary mask is imaged onto the channel using a microscope objective. Right: an artist's view of the contact region connecting the two reservoirs. Reprinted by permission from Macmillan Publishers Ltd: Nature [22], Copyright (2015).

spin-resolved; thus all currents are to be understood per spin states, and the factor for spin degeneracy is left out.

4.2. Reservoirs

As already mentioned earlier, a crucial advantage of the Landauer approach is that it separates the channel, which is a quantum coherent and elastic system, from the reservoirs where all the inelastic processes are taking place, without the need to describe them precisely. Cold atomic gases offer a situation where the physics of the reservoirs can be investigated directly, and their properties can be tuned. The validity of the Landauer approach as a function of the size of the reservoirs has been investigated theoretically and deviations at short timescales were predicted, which could be tested in the future [124, 125]. In particular, the dynamics associated with the onset of a quasi-steady state where the transport is described by the Landauer is expected to be observable in future experiments.

4.3. Experimental observation in cold atoms

We now come to the experimental observations reported in [22] using the two-terminal configuration. There, a binary mask featuring a narrow opaque line was imaged onto the two-dimensional channel through a high-resolution microscope objective, using blue detuned light, generating a repulsive potential. A schematic view of the setup and the resulting structure is presented in figure 14. This produces a split gate structure similar to that used in mesoscopic electronics.

Along the transverse direction (x), the high resolution of the microscope allows for very tight confinements, with typical transverse sizes of 1.5 μm. With the laser power available, the oscillation frequency reaches up to 50 kHz at the center of the structure. Along the direction of transport (y), the envelope of the structure is Gaussian, corresponding to the shape of the laser beam used for the imaging. The confinement therefore smoothly evolves from very weak in the wings of the beam, i.e. at the entrance and exit of the QPC, to very strong at the
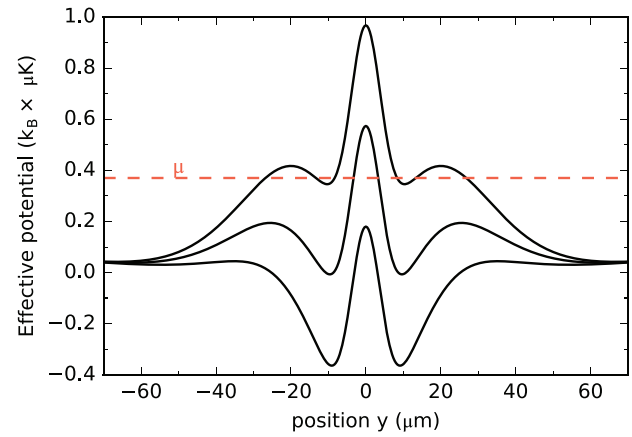

Figure 15. Semi-classical potential landscape, for the three lowest transverse modes with a gate potential of 0.78 μK. Here only the lowest transverse mode is below the chemical potential (dashed orange line).

center. Geometrically, this length scale is determined by the beam waist which is 5.5 μm in this experiment.

Additionally, a red detuned laser beam with a larger Gaussian envelope is superimposed onto the structure. This beam attracts atoms towards the center of the QPC, hence controlling the density in the QPC and its entrance and exit regions. The potential created by this beam is called gate potential, by analogy with top gates in semiconductor structures, and its strength at the center of the QPC is denoted V_g. This beam only affects the channel, and unless its power is very large it does not deform the reservoirs significantly.

The combination of laser beams creating a potential landscape is quite complex, but allows us to fulfill the apparently contradictory constraints for the observation of quantized conductance: (i) tight confinement, with frequencies much larger than the temperature, (ii) a high degree of quantum degeneracy and low temperatures and (iii) a controllable chemical potential, independent of temperature. Criteria (i) is met through the use of tightly focused beams for lateral confinements, and criteria (ii) is met through evaporative cooling and adiabatic decompression of the trap, yielding temperatures and chemical potentials that are lower than the transverse mode spacing: the QPC is empty due to the zero point motion. Criteria (iii) is met using the gate potential, which forces atoms into the QPC region, while keeping the temperature imposed by the reservoirs unchanged.

In order to understand transport through the structure, consider a semi-classical picture where motion along the transverse direction is quantized, leading to a longitudinal potential landscape for each transverse mode where atoms propagate quasi-classically. Such a quasi-classical potential landscape is presented in figure 15. This results in a one-dimensional problem where the energy resulting from the transverse confinement $E_\perp(y) = \frac{1}{2}h\nu_x f_x(y) + \frac{1}{2}h\nu_z f_z(y)$ acts as an additional potential, with $f_{x,z}(y)$ describing the spatial variation of the trapping frequencies of the QPC. Further contributions arise from the spatial profile of the gate potential $V_g(y) = -V_g f_g(y)$, and the underlying harmonic trapping potential extending over the entire cloud $V_{\text{trap}}(y) = \frac{1}{2}m\omega_y^2 y^2$.

Table 1. Envelope functions determining the effective potential.

Envelope function	Waist (μm)	Description
$f_x(y) = \exp(-y^2/w_x^2)$	$w_x = 5.6(6)$	QPC, x conf.
$f_z(y) = \exp(-y^2/w_z^2)$	$w_z = 30(1)$	QPC, z conf.
$f_g(y) = \exp(-2y^2/w_g^2)$	$w_g = 25(1)$	Gate potential

Table 2. Energy scales of interest for transport through our QPC.

Parameter	Typical value (kHz)	Description
ω_x	$2\pi \times 30$	Horizontal QPC confinement
ω_z	$2\pi \times 10$	Vertical QPC confinement
$\Omega_{y,n_x=0}$	$2\pi \times 1.3$	QPC curvature arising from split gate
$\Omega_{y,n_z=0}$	$2\pi \times 0.1$	QPC curvature arising from 2D confinement
$E_F/\hbar$	$2\pi \times 8.0$	Fermi energy
$\mu/\hbar$	$2\pi \times 7.7$	Chemical potential
$\Delta\mu/\hbar$	$2\pi \times 2.0$	Chemical potential bias
$k_B T/\hbar$	$2\pi \times 0.9$	Temperature

$$V_{\text{eff}} = E_\perp + V_g + V_{\text{trap}} + E_{\text{resid}}. \tag{19}$$

Extra contributions resulting from experimental imperfections, such as the finite contrast of the projected structures, can also be included and calibrated by independent transport measurements. The envelope functions are listed in table 1.

The finite length of the QPC is controlled by the curvature of the semi-classical potential around the center of the contact, modeled as an inverse harmonic oscillator. The typical parameters of the QPC are presented in table 2. Importantly, temperature is typically an order of magnitude lower than the lowest trap frequency at the center of the QPC, allowing for the resolution of individual transverse modes in the transport experiment.

The experimental measurement of the conductance of the QPC as a function of the gate potential and horizontal confinement are presented in figures 16 and 17 respectively. For the largest confinement at a fixed gate potential, or the lowest gate potential at a fixed confinement, the chemical potential in the channel is lower than the energy of the lowest mode of the QPC, hence the QPC is empty and the conductance is zero. As the gate potential is increased, or confinement is decreased, the conductance increases up to 1/h and saturates, forming a conductance plateau, until the second mode becomes available leading to another plateau of conductance.

These observations are compared with the predictions of the Landauer formula, which account for the semi-classical potential landscape, finite temperature and the finite bias, as shown with the solid lines in figures 16 and 17. The agreement is very good; in particular, the width and height of the plateaus agree very well, as well as the width of the transition region between plateaus, which is well accounted for by temperature. For the largest gate potentials, the deformations of the potential landscape are significant and transverse modes do not open at the center of the structure anymore, but
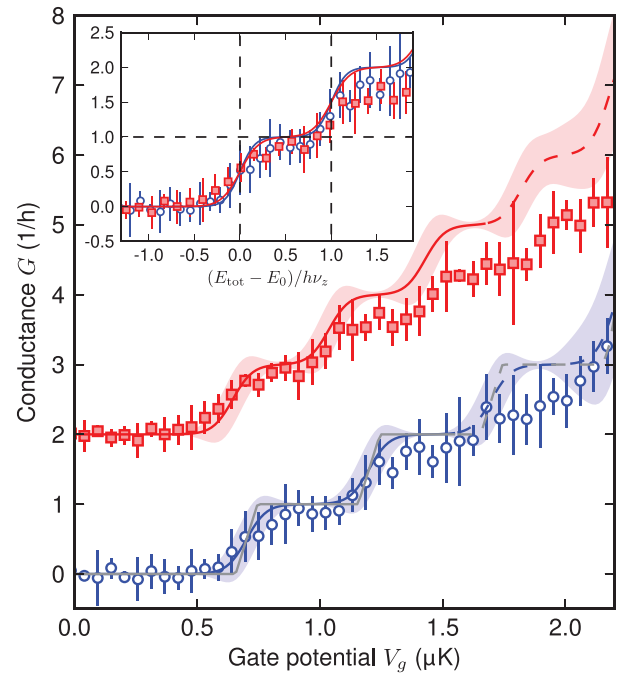

Figure 16. Conductance as a function of gate potential. Open blue circles correspond to a vertical confinement of $\nu_z = 10.4$ kHz. Filled red squares correspond to $\nu_z = 8.2$ kHz and are vertically shifted by two units for clarity. Each data point represents the mean of six measurements and the error bars indicate one standard deviation. Solid lines are theoretical predictions based on the Landauer formula of conductance. The shaded regions reflect the uncertainties in the input parameters (see text). Dashed lines are continuations of the solid lines and correspond to a change in the effective potential. Inset: first conductance plateau as a function of reduced energy, showing universal scaling. Vertical dashed lines indicate the width of the first plateau, whereas the horizontal dashed line indicates the universal conductance value 1/h. Reprinted by permission from Macmillan Publishers Ltd: Nature [22], Copyright (2015).

rather at the entrance and exit, leading to strong deviations compared to the calculations. The quantization is robust, and can be observed for reduced confinements along the vertical direction, as shown in red in the figures. While the data is compared here to independently measured quantities such as the trap frequencies, these measurements, being absolute, provide a useful calibration for the geometry of the QPC and have been used as such for the most recent experiments.

Compared to its condensed matter counterpart, the quantum point contact for atoms is rather long. The geometric length ($1/e^2$ radius of the beam) is about 5.6 μm, compared to the length scale associated with tunneling through the structure $\sqrt{\hbar/m\,\Omega} \sim 1.1$ μm. Hence, the width of the transitions between successive plateaus is entirely attributed to the finite temperature, rather than the tunneling, as is the case for mesoscopic structures in electronic systems.

Another important difference is the nature of the reservoirs. These are strictly isolated, and actually no dissipative process is taking place inside them: the potential is strictly conservative, the spontaneous emission from the dipole trap is negligible, and so are the atom losses. Interparticle scattering allows for the thermalization of the incoming particles, but the scattering mean free path for collisions in the reservoirs is about 12 mm,
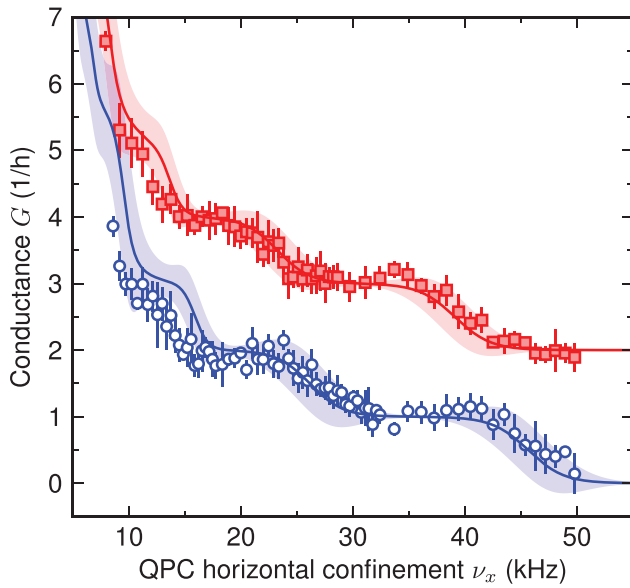
Figure 17. Conductance as a function of horizontal confinement. Open blue circles correspond to a vertical confinement of $\nu_z = 10.9$ kHz and a gate potential of $V_g = 1.0(1)$ μK. Filled red squares correspond to $\nu_z = 9.2$ kHz and $V_g = 0.8(1)$ μK, and are vertically shifted by two units for clarity. Solid lines are theoretical predictions based on the Landauer formula of conductance. The shaded regions reflect the uncertainties in the input parameters (see text). The error bars are the same as in figure 16. Reprinted by permission from Macmillan Publishers Ltd: Nature [22], Copyright (2015).

Figure 18. A theoretical comparison of quantized conductance for Fermions (A) and noncondensed bosons (B). Conductance is presented in units of $1/h$ as a function of the gate potential. ω_0 is the transverse trap frequency, ΔE_G denotes the width of the transition region and T_B is the critical temperature for Bose condensation in the reservoirs. Reprinted figure with permission from [129], Copyright (2016) by the American Physical Society.

quantum properties of transport can be predicted, including the transient establishment of the steady state or the current noise. The effects of a fixed atom number or finite extensions of the reservoirs can be modeled, and shown to influence many transport properties including the noise spectrum of the current or the thermoelectric response.

4.5. Role of quantum statistics

In the derivation of the Landauer formula, the role of quantum statistics in the conductance quantization appears in setting the occupation of the energetically available modes. This raises the question of the observations of quantized conductance for cold bosonic atoms. The fact that the group velocity and the density of states cancel in the derivation of the Landauer formula is a single-particle property. A first proposal was actually written for the transmission of a beam of cold atoms through a tight magnetic waveguide [128] regardless of the statistics of the atoms.

In the case of actual particle reservoirs containing bosons at thermal equilibrium, the situation is more complex, since at low temperatures Bose–Einstein condensation renders the reservoir phase coherent and superfluid (see section 5). The situation of reservoirs above the critical temperature was analyzed in detail in [129]. Because of bosonic stimulation for the low-energy states in the channel, the height of the conductance plateau is strongly enhanced, even with noncondensed reservoirs, up to a nonuniversal, temperature-dependant value. The shape of the transition from insulating to conducting as the first channel opens is also very different for bosons, again due to bosonic stimulation effects leading to sharper transitions. The predictions are presented in figure 18.

4.6. Other neutral particles

The first generalization of the concepts underlying the Landauer approach to neutral particles was the case of

which is much larger than the size of the reservoir. Thus energy relaxation is entirely nonlocal. The effects of collisions in the reservoirs were further investigated by reducing the scattering length in order to entirely suppress energy relaxation on the timescale of transport. The conductance measured with the very same protocol was found to be identical within experimental uncertainties [22]. This counterintuitive result can be explained by the fact that even though particles that are incident from the channel into the reservoirs do not release their energy, the three-dimensional, nonharmonic shape of the reservoirs most likely makes them chaotic. Thus, the probability that the incident atom can come back to the channel and reduce the measured current is very small, even in the absence of collisions.

4.4. Quantum interference in transport

Even though the conductance is quantized in units of $1/h$, the motion of atoms along the transport direction remains semi-classical. In the presence of more complex structures in the channel, such as fine-grained disorder or any set of partially transmitting obstacles, transport is strongly modified by quantum interference. The description of this phenomenon in the condensed matter context is a major topic of research and goes far beyond the present paper. We refer the readers to the standard textbooks for a description of these effects in condensed matter physics [1].

In the context of cold atoms, theoretical studies have been conducted which consider canonical examples of one-dimensional Hubbard chains or single state quantum dots weakly coupled to reservoirs [126, 127]. In these cases, the genuinely
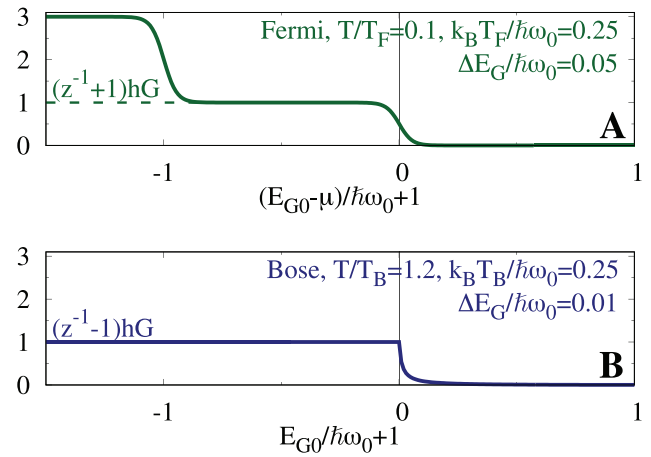
photons. In this situation, there is no counterpart to the chemical potential, and thus no chemical potential bias, as the number of photons is not conserved. Nevertheless, the transmission probability through narrow apertures also increases stepwise as the aperture is opened, as was observed in [130]. The crucial ingredient in observing this effect is to mimic incoherent reservoirs, which populate every energetically accessible mode while keeping monochromatic light to mimic the low-temperature case, and to integrate symmetrical detectors over all possible momenta for the photons emerging from the channel. This was achieved using diffuse illumination and an integrating sphere for detection. Jumps in the transmission occur with a spacing of $\lambda/2$. No quantum effects are involved in the experiment, highlighting the fundamental role of the wave character of matter for massive particles.

The case of phonons in solid-state systems is conceptually similar, but of much more fundamental interest due to its connection with heat transport. For dielectric narrow wires where heat is only carried by phonons, the Landauer approach yields a universal heat conductance quantum equal to $k_{\rm B}^2 \pi^2 T / 3h$, where T is the average temperature of the system, in the low temperature limit [131]. Experiments conducted on suspended nanostructures have shown saturation of the heat conductance at low temperatures compatible with this bound [132]. Quite remarkably, the quantum of heat conductance is actually a universal bound, not restricted to phonon transmission. It is rooted in Shannon's theorem stating the upper bound for the amount of information that a single channel can carry [133]. Recently, a new set of experiments has measured the quantum of heat conductance associated with electrons in a mesoscopic structure in the quantum Hall regime, showing good agreement with the universal limit [134].

Quantized transport measurements were also proposed for dilute mixtures of ^{3}He in ^{4}He. For very dilute mixtures at the lowest temperatures, ^{3}He behaves like an ideal Fermi gas with a very long mean free path of several tens of micrometers. An array of nanopores was then proposed as a connection between two tanks of helium, with holes on the order of 10 nm, which is compatible with the Fermi wavelength of ^{3}He [135, 136].

5. Superfluid transport in Bose–Einstein condensates

The results that were presented in the previous sections concerned weakly interacting Fermi gases, and the physics was that of ideal gases. In the presence of interactions between particles, the gases can turn superfluid in part, if not all of the system. This is the case for low-temperature bosons, and low-temperature Fermions in the presence of attractive interactions. Both cases are realized in cold atom experiments, and transport in the two-terminal setup has been studied under these conditions.

In contrast to normal currents, which are driven by chemical potential gradients, superfluid currents are driven by gradients in the phase ϕ of the superfluid order parameter $\psi = |\psi| e^{i\phi}$. More precisely, the superfluid velocity is given

by $v_s = \frac{\hbar}{m} \nabla \phi$. Most of the dynamical properties of superfluids can be understood based on the principle contained in the Josephson–Anderson equation [137–141]:

$$\hbar \frac{\mathrm{d}\phi}{\mathrm{d}t} = \mu \qquad (20)$$

where μ is the chemical potential. In the two-terminal configuration, this reduces to the usual Josephson relation, but it has a very general validity for both bosonic and fermionic superfluids, weak and strongly interacting, and explains a wide range of phenomena such as vortex motion and nucleation.

For a general superfluid system such as helium, the relation between the superfluid order parameter and the microscopic parameters of the system is a very involved problem, since the densities are large and the interactions are strong [140]. In contrast, cold atoms are often weakly interacting systems for which a mean-field theory based on the microscopic Hamiltonian provides an accurate description. The Gross–Pitaevskii equation for Bose–Einstein condensates identifies the macroscopically populated single-particle wave function with the superfluid order parameter, allowing for simple and transparent derivation of the Anderson equation from the microscopic model [26, 140]. In the case of attractively interacting Fermions, the BCS mean-field model provides a similarly simple description, identifying the pairing gap with the amplitude of the order parameter [140]. However, in contrast to the Gross–Pitaevskii equation for bosons, this description of fermionic superfluids is usually only qualitatively correct for dilute atomic gases, as the strength of interactions necessary to produce superfluid Fermi gases at the temperatures achievable in the experiments is usually too strong for mean-field theory to be quantitatively correct. Nevertheless, in both cases, most of the phenomenology can be captured by the Anderson equation, which provides a unified picture of superfluidity.

Cold atom experiments have provided a wide playground for superfluid transport measurements, where the phase coherence plays a key role [142, 143]. Like in the previous section, coupling a device with universal transport properties to a reservoir allows the system to be driven and the transport coefficients to be measured. A general feature throughout these experiments is also the combination of the universal Josephson–Anderson equation, with a reservoir dynamics that depends on the geometry and the details of the setup.

5.1. Superfluid flow

The question of the superfluid nature of the Bose–Einstein condensates has been thoroughly investigated in experiments over decades following the realization of Bose–Einstein condensation in dilute gases. Contrary to long range order, which is directly probed at equilibrium using time-of-flight or more elaborate interferometric techniques, superfluidity is a dynamic property that requires the system to be set in motion. The existence of a critical velocity for the creation of excitations in a cloud is usually regarded as demonstrating superfluidity. Such experiments have been realized by steering
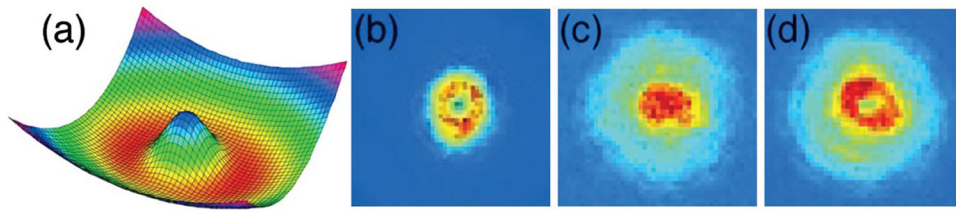
Figure 19. Bose–Einstein condensate in a ring trap. (a) The potential landscape produced by the combination of a magnetic trap and a repulsive optical plug at the center; (b) an *in situ* absorption image of the condensate in the ring trap; (c) and (d) time-of-flight images of the condensate released from the ring trap in the absence (c) and presence (d) of rotation. Reprinted figure with permission from [60], Copyright (2007) by the American Physical Society.

an obstacle inside a condensate and probing the heating rates [144–146], or imprinting a moving optical lattice and measuring heating as a function of velocity [147].

A set of experiments has been performed using connected geometries, created by placing a Bose–Einstein condensate in a ring-shaped trap [60–63]. An example of such an experiment is presented in figure 19, extracted from [60]. Such a configuration realizes a minimal version of a circuit for atoms, and has a lot of similarities with superconducting quantum interference devices [148] and superfluid helium gyroscopes [139, 141].

The dynamics in such systems is probed by injecting angular momentum into them. This can be achieved using Raman transitions, by which a cloud that is initially at rest in one internal state is coherently transferred into a different internal state, using a pair of laser beams with a frequency difference matching the energy difference between internal states [60]. During this process the relative phase of the two laser beams is imprinted onto the atoms. Choosing a Laguerre–Gaussian profile for one of the laser beams, a phase circulation is coherently imprinted, effectively transferring one quanta of angular momentum from the beam to each atom. The persistence of the rotation is a direct consequence of the existence of the macroscopic order parameter Ψ whose phase gradient gives the superfluid current. Indeed, for Ψ to be single-valued, the number of phase windings around the ring can only vary by integer units. Any unwinding event has to occur via the creation of vortices within the ring, which represents an energy cost whenever $|\Psi|$ takes a macroscopic value. This can be seen as a macroscopic free energy barrier that prevents the relaxation of the current to the ground state.

Currents in the ring are inferred from time-of-flight measurements: the trap is turned off, allowing the ring to be filled due to the expansion of the condensate in the radial direction. In the presence of a net circulation in the ring, corresponding to a phase winding of 2π around it, the hole is seen to persist after expansion. This can be understood by considering that atoms emerging from opposite sides of the ring interfere destructively at the center, leaving a hole in the far field. Equivalently, one can consider that the circulation in the ring is equivalent to a vortex trapped in the zero density region inside it. Upon changing the trap configuration, this vortex will remain at the center of the cloud and be revealed upon increasing the density.

The stability of persistent currents depends, in practice, on many parameters of the experiments, such as the smoothness and stability of the potentials used to trap the atoms. It was

observed that currents injected into these rings persisted for several tens of seconds or even minutes. Remarkably, the lifetime of these currents was longer than the lifetime of the cold gas itself, such that even condensates that lost a large fraction of their initial atom number would maintain their rotation, providing a striking demonstration of persistent currents [62].

The decay of super currents was investigated thoroughly in the presence of a controlled weak link [61]. An elliptic laser beam, producing a repulsive barrier, was focused onto a small portion of the ring trap. The length of the weak link was greater than the healing length of the condensate, such that its main effect was to reduce the local density, and hence the speed of sound and condensate fraction. It was observed that the current was stable until the height of the barrier reached a certain fraction of the chemical potential of the condensate. This constituted direct evidence for the existence of a critical velocity. However, the critical velocity was different from the speed of sound, as predicted by the Landau theory, showing that the currents did not decay via the emission of single-particle excitations. The creation of vortices within the ring was identified as the decaying mechanism, following Feynman's original arguments [149], and confirmed using direct numerical simulations.

The reverse operation of creating rotation using a rotating barrier was later investigated [150]. This is qualitatively equivalent to the decay of rotation up to a change of reference frame from the lab frame to that moving with the barrier. Accordingly, stepwise changes in the winding were observed upon increasing the rotation velocity. This technique, however, is not restricted to imprinting one quantum of angular momentum, but can be used to introduce larger angular momentum in the system. Because of the large free energy barriers that need to be crossed to vary the angular momentum in the ring, the circulation presents hysteresic behavior when trying to increase and decrease the rotation, which was directly demonstrated in [151]. This is reminiscent of the persistent character of the currents and represents a hallmark of superfluid circuits.

5.2. Two reservoir experiments with Bose–Einstein condensates

The first experimental realization of a weak connection between two cold atom clouds was realized in Heidelberg in 2004 [66]. Earlier experiments were performed by placing a condensate in a one-dimensional optical lattice, so as to form a chain of coupled condensates [35, 65]. The evolution of phase coherence and the number of fluctuations in particular was

measured in [64], which was a precursor of the superfluid-to-Mott insulator transition in 3D optical lattices [152].

In the Heidelberg experiment, a condensate loaded into a small harmonic trap was split in two in a controlled way, allowing for the preparation of initial population imbalances. The key to the dynamics of this system is the phase coherence between the two reservoirs[8].

The outcomes of such an experiment were first predicted using a two-mode model by which the internal dynamics within the two coupled condensates is neglected [153]. The evolution is captured by a two-component Gross–Pitaevskii equation, describing the condensate in each well and a coherent tunneling term coupling the condensate wave functions of the two condensates. Introducing canonically conjugated variables for the phase difference between the two condensates ϕ and the atom number difference between the two wells $z = \frac{N_{\rm L} - N_{\rm R}}{N_{\rm L} + N_{\rm R}}$, one obtains two coupled nonlinear equations [153]

$$\dot{z} = -\sqrt{1 - z^2}\, \sin(\phi) \tag{21}$$

$$\dot{\phi} = \Lambda z + \Delta E + \frac{z}{\sqrt{1 - z^2}} \cos(\phi) \tag{22}$$

where ΔE controls the asymmetry in the trap, and Λ controls the interaction strength between the particles, which is the equivalent of a charging energy for capacitive Josephson junctions. These equations predict a regime of 'Josephson' oscillations, where a small initial population imbalance oscillates between the two wells at the plasma frequency $\omega_{\rm J} = \sqrt{E_{\rm C} E_{\rm J}}$ determined by both the coupling between the wells, controlled by the coupling strength $E_{\rm J}$ and the strength of the repulsive interactions, yielding an effective inverse-compressibility measured by $E_{\rm C}$. The phase difference oscillates in quadrature. These oscillations are reminiscent of the AC Josephson effect in superconductors, but the trapped nature of the system sets them at a nonuniversal frequency. This regime is observed in the experiments; see figure 20. A direct observation of the Josephson oscillations at a frequency equal to the bias was reported in a later experiment [67].

With stronger initial imbalance between the two wells, the equations predict a 'self-trapping' regime, where the populations in the two wells show weak oscillations around their initial value, and the phase difference increases linearly. This regime is reached when the initial particle number difference, or more generally the initial internal energy difference between the two wells, is large compared to the coupling between the condensates. Except for the weak oscillatory behavior, the dynamics is that of decoupled condensates with different chemical potentials and follows directly from the Josephson–Anderson equation. This dynamical decoupling was also observed in the experiment, as shown in figure 20.

Rather than starting from a two-mode model, adapted to large barriers or weak connection, one can start from a single condensate and study the evolution of the dynamics as a tunnel barrier is raised. Theory and experiment in this regime has been
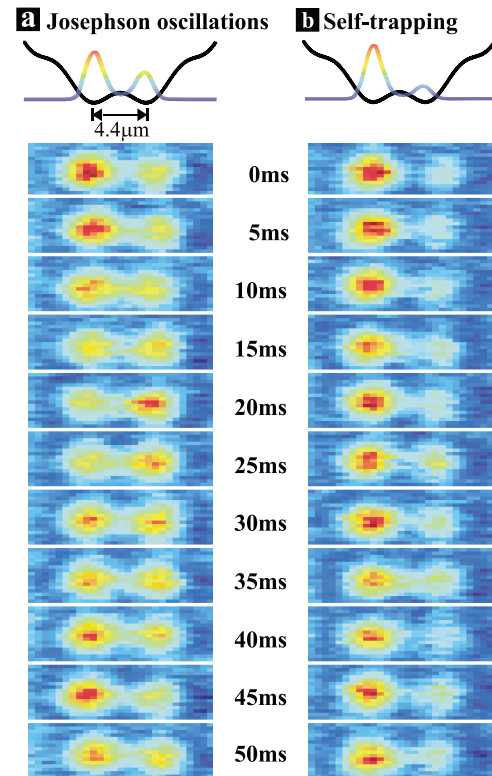
Figure 20. Tunneling in Josephson-coupled Bose–Einstein condensates. A Bose–Einstein condensate is placed in a symmetric double well potential with an initial population imbalance, and left to evolve freely, either with a weak initial population imbalance (left) or a strong imbalance (right). The resulting dynamics shows either plasma oscillations or self-trapping, respectively. Reprinted figure with permission from [66], Copyright (2005) by the American Physical Society.

reported in [68]. In the absence of a tunnel barrier, the cloud performs dipole oscillations. The uniform velocity within the cloud translates to a uniform phase gradient: the phase difference across the cloud oscillates in quadrature with the population. As the barrier is raised, the oscillation frequency decreases and smoothly connects to the plasma frequency in the regime of large barriers. Qualitatively, the phase gradient, which was linear in the absence of the barrier, steepens in the low-density region of the barrier, leading to flatter phase profiles inside the wells and a steep phase drop in the junction. A theoretical model explicitly accounting for the coupling between the oscillating mode and other excitation modes in the condensates was found to successfully reproduce the data. In particular, the beating of several frequencies was observed experimentally in the population dynamics as a result of this coupling.

A qualitative interpretation for the role of the harmonic trap is a harmonic oscillator, such as an LC circuit, coupled in series to the Josephson junction. In the weak barrier regime, the junction merely renormalizes the resonance frequency by enhancing the inductive effect. In the strong barrier regime with weak population imbalance, the low currents lead to weak effects of the inductance L, such that the dynamics is that of a capacitive Josephson junction with its plasma mode. Eventually, the self-trapping regime is reached for stronger imbalances, where the high-frequency Josephson oscillations
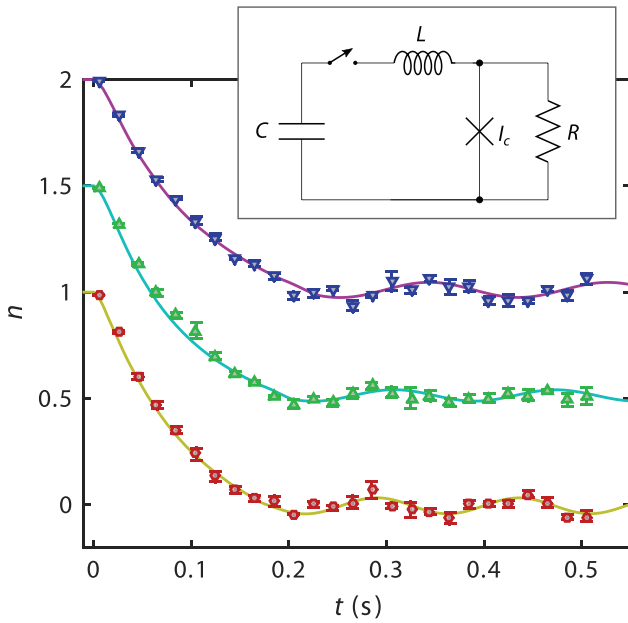
Figure 21. The evolution of populations in a strongly imbalanced two-terminal setup with Bose–Einstein condensates connected by a few-mode quantum wire. After the initial exponential decay, the imbalance oscillates. The three colors represent the increasing densities in the channel 599(17) μm^{-1} (blue), 665(16) μm^{-1} (green), 790(25) μm^{-1} (red). The inset presents a lump element model for the dynamics capturing the dissipative, reactive and Josephson dynamics expected in this circuit. Reprinted figure with permission from [154], Copyright (2016) by the American Physical Society.

essentially decouple from the harmonic trap. At the time scale of LC oscillations, the current in the junction averages out to zero and the population imbalance is constant.

Recently, a long quantum wire connecting two Bose–Einstein condensates was realized [154] following experiments with thermal bosons in [94]. A very large population imbalance was imposed and the evolution was observed to cross over from an initial exponential decay for large imbalance to oscillating behavior, interpreted as the LC oscillations of the populations, as shown in figure 21. This dynamics was successfully reproduced using an LC circuit coupled to a resistively shunted Josephson junction, where the initial decay of the population imbalance results from the resistive element, while the oscillating behavior represents LC oscillations. Interestingly, the magnitude of the resistance was found to be extremely low—two orders of magnitude lower than expected from the Landauer formula for free particles—highlighting the key role played by superfluidity. The microscopic mechanism for resistive flow was identified to be vortex nucleation at the exit of the channel, and vortex-like excitations were directly identified in the low-density reservoir.

Rather than using two traps as reservoirs, it is possible to locally deplete one well in an optical lattice in order to mimic the drain reservoir, as performed in [80]. There, one site of the lattice was depleted by more than 90%, the subsequent refilling of the site was measured, and a direct analogy with a two-reservoir configuration was drawn. An interesting feature of this experiment is the existence of a regime of large chemical potential bias where the current decreases with increasing

bias, hence denoting negative differential conductivity. This phenomenon was attributed to density-dependent tunneling: the transverse profile of the condensate depends on its density, so do the matrix elements for hopping between filled and empty sites.

6. Two-terminal transport in superfluid Fermi gases

Using the control offered by Feshbach resonances (see section 2), it is possible to create attractive interactions between Fermions in different spin (hyperfine) states that are strong enough for the Cooper pairing and superfluidity to appear. A Fermi gas in the vicinity of a broad Feshbach resonance realizes the crossover from the Bose–Einstein condensate of molecules to BCS superfluidity, as the magnetic field is varied across the resonance. Across the resonance, the system crosses the strongly interacting regime where the scattering length is larger than interparticle spacing. Superfluidity was demonstrated at a low temperature in the entire crossover, and the thermodynamic properties of the system are now experimentally known with great accuracy (see [4] for a recent review). The body of knowledge gathered on such a strongly correlated superfluid is indeed used as a benchmark for numerical techniques aimed at treating strongly correlated Fermions.

Superfluids are ideal test beds for transport measurements, since the variations in conductance upon crossing the transition are expected to be very large. Since superfluidity mainly occurs on the Fermi surface, transport directly addresses the fraction of atoms which experiences strong quantum correlations in the superfluid phase. This contrasts with the density distribution observed in absorption imaging, which observes the entire Fermi gas, where most of the signal comes from atoms deep in the Fermi sea, where no correlations appear at the phase transition[9]. High-precision measurements of the density profiles can be used to reveal a jump in the compressibility of the gas characteristic of the superfluid transition [99]. In the case of BCS superfluids, well known in condensed matter physics, the actual equation of state is actually unchanged, hence no density variations are expected, even though the resistance is reduced to zero. This was a major motivation for the investigation of transport in the two-terminal configuration in strongly attractive Fermi gases.

6.1. Superfluid Fermions in the multimode regime

Following the realization of the two-terminal system for weakly interacting Fermions, the very same configuration was used to investigate the unitary fermionic superfluids produced in the vicinity of the Feshbach resonance [19]. A measurement protocol identical to that described in section 3 was applied, allowing for a direct comparison between weakly interacting gases and the unitary Fermi gas in the same experimental conditions.

---

[9] In the case of spin-imbalanced Fermi gases, a first order transition between the paired and polarized superfluid takes place, and the density profile acquires a distinctive kink that was used to identify the superfluid transition [155, 156].
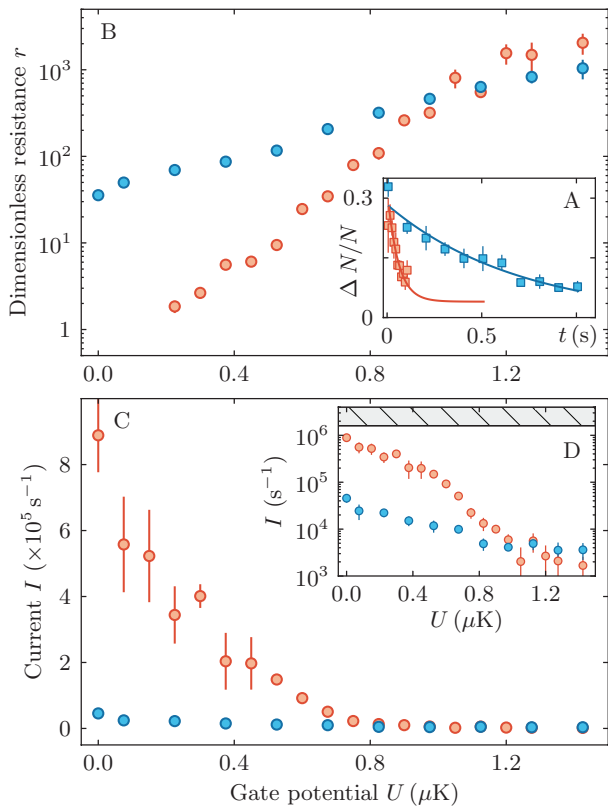
Figure 22. Conduction properties through the channel. Red and blue data points correspond to the strongly and weakly interacting gas, respectively. (A): The decay of the relative atom number imbalance between the source and drain as a function of time with a gate potential $U = 525(50)$ nK. The solid lines are exponential fits with a fixed offset of 0.04 for the red curve to account for a small remaining imbalance in the reservoirs. (B): Dimensionless resistance r as a function of the gate potential. The data points that are shown are those for which the decay is exponential. (C): The atom current as a function of the gate potential U. A large increase of the current appears for the strongly interacting gas below $U \approx 0.7\ \mu$K. (D): The atom current on a logarithmic scale. The dashed region indicates the maximum current allowed by the internal dynamics of the reservoirs (see text). The error bars show the statistical errors (one standard deviation). Reprinted by permission from Macmillan Publishers Ltd: Nature [19], Copyright (2012).

As a control parameter, a repulsive gate potential was applied to the two-dimensional channel, in the form of a Gaussian beam propagating along the vertical direction. This beam has a waist of 18 μm, covering the center of the transport channel and allowing for a local reduction of the chemical potential (or equivalently the local density). The main advantage of this control parameter is that it only affects the channel and leaves the reservoirs unchanged. Therefore, the thermodynamic properties of the reservoirs do not need to be accounted for precisely in order to interpret the evolution of transport. Later experiments with a similar setup use detailed knowledge of the equation of state to infer the precise thermodynamics of the reservoirs, even in the strongly interacting state.

A decay of the initially prepared bias ΔN was observed for both the unitary Fermi gas and the weakly interacting Fermi gas at a low temperature as a function of the gate potential. It was found that this decay follows exponential behavior (see

figure 22(A)), at least down to low values of the gate potential, justifying an RC model description similar to that introduced in section 2. The decay constant τ was normalized to the underlying trap frequency ω_y along the transport direction, measured by dipole oscillations in the absence of any channel or gate potentials at the center, yielding a dimensionless resistance $r = \tau\omega_y$.

The variations of r with the gate potential are presented in figure 22(B). For the largest gate potentials—or lowest densities—r is of the same order for both weakly and strongly interacting systems, but as the gate is reduced, r drops very quickly and reaches values about 50 times lower than for the weakly interacting system exposed to the same gate potential strength. The lowest measurable resistance is also one order of magnitude lower than that of the weakly interacting gas without any gate potential.

For gate potentials below 0.2 μK, the decay of ΔN was found to deviate from the exponential behavior, in the form of residual oscillations of the populations, at frequencies close to the underlying dipole mode along the transport direction. In this regime, the assumption of thermal equilibrium of the reservoirs no longer appears to be valid. For such low gate potentials, an observable independent of the reservoir equilibration is the current through the channel observed during the early stage of the decay. This initial current keeps increasing down to zero gate potential, as can be seen in figure 22(C). Interestingly, the order of magnitude of the current is similar to that expected for free dipole oscillations in the absence of any channel or gate, which represents the upper limit on currents due to energy conservation: indeed, the dipole mode represents the full, periodic conversion of potential energy into kinetic energy. Figure 22(D) shows the measured currents together with this limit, where the measurements for the unitary gas approach the limit within a factor of two.

These observations are in line with the qualitative expectations for a superfluid system, i.e. the ability to flow with very little resistance through narrow apertures which efficiently stop any other normal fluids, discovered with superfluid helium by Allen and Miesner, and Kapitza in 1938 [157, 158], and for which the word superfluid was introduced [159].

Beyond these qualitative observations concerning the drop in resistance in the case of unitary superfluids, more insight can be extracted by combining the current measurements with local observations of the distribution of particles in the channel, using high-resolution absorption imaging. Two main points are extracted:

- The density distribution at equilibrium, i.e. in the absence of current, can be used to extract the thermodynamic potential Ω at the center of the channel, based on the local density approximation and the Gibbs–Duhem relation, following the procedure described in [99]. Comparing this with the thermodynamic potential and an ideal Fermi gas at the same density, we form a quantity Ω/Ω_0 that can be used to quantify the degree of quantum degeneracy and relate it to the transport properties.
- The line density in the channel obtained by integration of the measured density along the transverse direction.
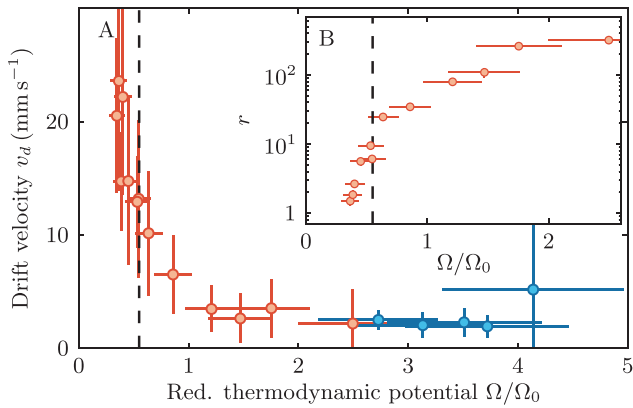
Figure 23. Conduction properties as a function of thermodynamic potential. (A): The drift velocity as a function of the reduced thermodynamic potential Ω/Ω_0 for the strongly interacting (red) and weakly interacting (blue) Fermi gas. (B): The dimensionless resistance as a function of Ω/Ω_0 on a logarithmic scale for the strongly interacting gas, showing the drop in resistance. The dashed black lines at $\Omega/\Omega_0 = 0.55$ indicate the position where the superfluid transition occurs in three dimensions. Error bars represent statistical errors (one standard deviation). Reprinted by permission from Macmillan Publishers Ltd: Nature [19], Copyright (2012).

Normalizing the current measured using the two-reservoir configuration by the measured line density, we obtain a drift velocity that measures the transport properties independently of the density of particles.

The refined observations are presented in figure 23, and confirm the order of magnitude increase in velocity for the unitary gas in the quantum degenerate regime. Since in the case of superfluid reservoirs current is driven by the phase gradient, owing to the Josephson–Anderson equation, the observation of resistive behavior implies the onset of a dissipative mechanism, which allows the decay of superfluid flow. Vortex nucleation is compatible with the observations, in contrast with the simple estimates for single-particle excitations provided by the Landau argument. This situation is similar to that of smooth weak links in BECs in the ring geometry, where such mechanism is backed by strong numerical and experimental evidence.

That such a mechanism leads to resistive behavior for sufficiently large velocities was explicitly demonstrated by separating a ring trap in two reservoirs using two distinct links [160]. Moving both links in opposite directions at a fixed velocity amounts to imposing a constant flow, and the onset of dissipation is observed as a density difference builds up between the two parts.

6.2. Interplay with disorder

A very attractive aspect of cold atomic gases is the ability to introduce fully characterized, controlled disorder. The effects of disorder on superfluidity have been investigated in the context of cold atomic gases for about a decade [6, 161]. The main focus so far has been the investigation of the phase diagram of a disordered system, in particular the observation of the elusive Bose–Glass phase [33, 162–168], predicted by

theory [169–171] and for which clear experimental demonstration has proven difficult. Several experiments have used phase coherence measurements and transport generated by a homogeneous magnetic field gradient as evidence for disorder-induced localization, finding, in general, that sufficiently strong disorder is capable of destroying superfluidity. The main motivation for extending these studies to transport measurements was to use the high sensitivity of transport to superfluidity in order to provide further insight into the mechanisms that destroy superfluidity in disordered systems. This problem is still open in the context of condensed matter to a great extent.

In the two-terminal configuration, the effects of disorder were investigated by replacing the homogeneous gate potential used to tune the density of atoms locally by the disordered potential produced using a speckle pattern [21]. The potential was repulsive, consisting of a random distribution of hills with an average strength $\bar{V}$. In addition to its average strength, disorder is also characterized by its correlation length $\sigma = 290(90)$ nm, which is the half width at half maximum of the power spectral density of the potential, directly measured *in situ*. The correlation length plays a key role in the physics of Anderson localization for single particles, since it determines the scattering mean free paths and localization lengths.

The simple situation of a Bose–Einstein condensate was first investigated using a gas of tightly bound molecules produced in the molecular regime of a broad Feshbach resonance. The magnetic field was chosen such that the s-wave scattering length was 3545 a_0, where a_0 is Bohr's radius, and the binding energy of the molecules was $E_b = 2.3$ μK. In comparison, all the other energy scales, such as the correlation energy $E_\sigma = \hbar^2/2m\sigma^2$ and $\bar{V}$, are weak. As a consequence, a description of the system in terms of the Bose–Einstein condensate is adequate. In this framework, the relevant length scale for the effects of disorder on superfluidity is the healing length, which in this experiment is typically $\xi \simeq 230$ nm, of the order of the correlation length of the disorder, such that disorder does not simply reduce to a smooth modulation of the condensate profile but can deplete the condensate directly.

Similar to experiments with a smooth gate potential, the measurements were repeated using a weakly interacting Fermi gas under the same conditions, in order to provide a comparison point where superfluidity is absent. This is of particular interest in the case of disordered systems, since the single-particle problem is already a pretty involved problem in the regime where disorder is not perturbative. In particular, the transport properties change dramatically with disorder strength without the need to invoke localization or many-body properties, which makes it hard to identify the genuine effects of superfluidity.

Figure 24 presents the ratio of resistances measured for the BEC and the weakly interacting system. We identify a strongly disordered regime where the ratio is constant and of order one. In this case, a simple interpretation is that disorder dominates over all the other processes and no phase coherence or superfluid effects contribute to transport. Upon reducing the disorder strength, a strong reduction of resistance for the BEC shows up and for the weakest disorder, the large currents
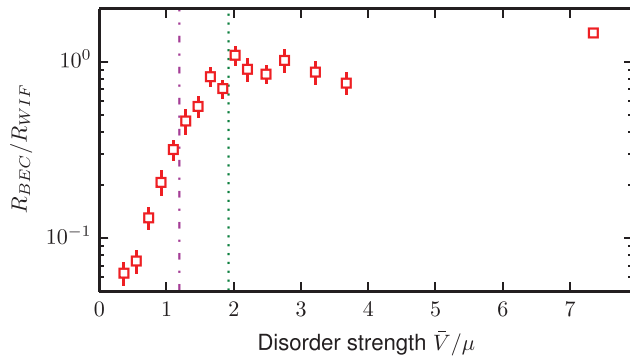
Figure 24. The ratio of resistances of the BEC and the weakly interacting Fermi gas (WIF) as a function of disorder strength. The disorder strength V_0 is normalized to the chemical potential of the BEC μ. The green dotted line represents the percolation threshold of the speckle potential, and coincides with the change of behavior from superfluid to single-particle transport. The dash-dotted line shows the correlation energy E_σ. Error bars represent statistical errors. Reprinted with permission from [172], Copyright (2014) by the American Physical Society.

involved prevent thermalization in the reservoirs and no resistance can actually be attributed, as observed already in the clean case [19].

The transition between the two regimes takes place for a disorder strength of the order of twice the chemical potential of the BEC. This is actually the position of the expected percolation threshold of the potential [173, 174]: a classical particle with energy below $V_{th} = 0.52\bar{V}$ is typically trapped in a finite region of the disordered landscape, with a probability approaching one for large systems, while a particle with energy higher than V_{th} can diffuse. This corresponds to a classical phase transition from metal to insulator. For the case of a BEC, the condition $\mu > V_{th}$ corresponds to having a connected superfluid pierced by disorder hills, which we expect to support a finite superfluid flow. Conversely, $\mu > V_{th}$ corresponds to disconnected superfluid islands.

This picture agrees with the observation for the position of the observed threshold. However, we only expect it to hold qualitatively as it disregards several important ingredients: (i) tunneling through the disorder barriers can be significant, since the correlation energy is rather large compared to μ. Since such processes can maintain phase coherence, the picture of disconnected superfluid islands does not prevent macroscopic phase coherence or superfluidity. (ii) Anderson localization due to wave interference certainly strongly modifies the percolation picture, by further localizing particles that would classically diffuse. The interplay between localized single-particle states and interaction-induced hybridization has been shown to lead to delocalization [164].

Regarding the nature of the strongly disordered state, further information was gathered using *in situ* absorption imaging, allowing the compressibility of the system to be estimated. This is an important observable, as finite compressibility together with an insulating character is a feature of the Bose–Glass phase. The compressibility was indeed observed to remain finite over the whole range of disorder strength explored, providing further hints that the strongly disordered regime has a lot in common with that of the Bose–Glass.

These qualitative findings were found to be very robust when varying the interaction strength in the BEC-BCS crossover, with the existence of the two regimes of low disorder and high disorder characterized by their resistance compared to the weakly interacting Fermi gas, and the fact that the compressibility remains finite. Very similar findings were also reported using the unitary Fermi gas and disorder with a longer correlation length [23]. In the latter case, the correlation length of the disorder was $\sigma = 0.72(5)$ μm, which is large enough for individual modulations of the disordered potential to be resolved by direct optical imaging.

Such images are shown in figures 25(a)–(e) for increasing disorder strength, and figure 25(f) shows the underlying disorder potential landscape. The fragmentation of the density profile is obvious from the evolution with increasing disorder. The amount of modulations in the density profile was measured and seen to saturate (figure 25(h)) above $\bar{V} \sim \mu$, where μ is the chemical potential here for unitary gas in the reservoirs. This was also the point were the transport properties entered the strongly disordered regime where they are equal to that of the weakly interacting Fermi gas. This threshold actually corresponds to the percolation threshold for *pairs* composed of two particles, thus seeing disorder which was twice as strong. These pictures were analyzed in terms of the continuous percolation of the density distribution, forming paths connecting the two reservoirs at lower densities with increasing disorder.

The systems of superfluid Fermions in the presence of disorder have been thoroughly investigated in condensed matter physics, in particular since the 90s in thin superconductors, where a superconductor-to-insulator transition was observed [175, 176]. The situation of superfluid Fermion pairs in the presence of disorder with a thin film configuration has a lot in common with superconducting films, with a few important differences. First the finite correlation length of the disorder introduces a new length scale in the problem, such that the results obtained have a lower degree of universality than homogeneously disordered films. In this respect, the situation is more similar to granular systems. Second, since atoms are neutral particles, no mechanism analogous to Coulomb repulsion can lead to the pair breaking, and nothing prevents pairs from forming more and more localized compounds with a strong overlap between the two constituents. This was indeed the interpretation proposed in [23] for Fermi superfluids forming a percolated phase of pairs in the two-terminal measurements, even though the pairs in the clean system extend over distances that are larger than the correlation length of the disorder.

The last difference, which has been the focus of a lot of attention in recent years, is the isolated nature of atomic gases. This raises the question of the mechanisms by which a system reaches thermal equilibrium. In a situation where single-particle states are localized over a large range of energies, like in strongly disordered systems, the phenomenon of many-body localization can localize the system in the Hilbert space, where even in a steady state, some observable will strongly differ from the expected values at thermal equilibrium [177–180]. The first evidence of nonthermal states emerging in strongly disordered atomic gases was reported very recently
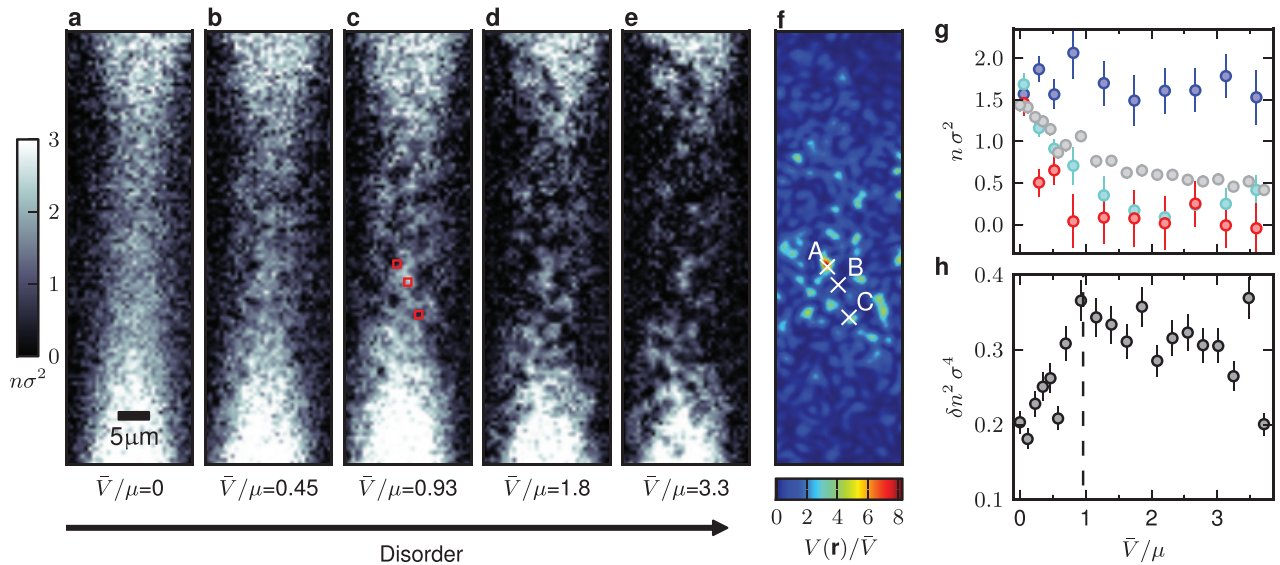
Figure 25. The evolution of the column density n (in units of σ^{-2}) as the disorder strength is increased. (a)–(e) High-resolution images of size $21\ \mu\text{m} \times 72\ \mu\text{m}$ of the *in situ* density distribution in the channel for increasing $\bar{V}/\mu$. The saturated column density on the top and bottom marks the beginning of the reservoirs, which extend far beyond the field of view. The systematic uncertainty in $\bar{V}/\mu$ is estimated to be 25%. (f) An image of the projected speckle pattern; the density ripples, which gradually appear from panels (a)–(e), can be matched one to one to the bright (potential hills) and dark spots (potential valleys) in the image. (g) The local column density as a function of disorder strength for three specific points indicated in the potential landscape of panel (f) (point A: red, point B: blue, point C: cyan), each computed within a region of size $1.2\ \mu\text{m} \times 1.2\ \mu\text{m}$ marked as red squares in image (c). The gray data points are the mean column density in the channel, computed in a central region of size $18\ \mu\text{m} \times 7\ \mu\text{m}$. (h) Variance of the density computed in the same central region; the dashed line represents the theoretical percolation threshold for the potential seen by point-like pairs. Reprinted with permission from [23], Copyright (2015) by the American Physical Society.

[181]. It should, however, be emphasized that slow equilibration or hysteric behavior is a general feature of systems that have bad transport properties, even for purely classical reasons, as is well known for glassy systems. Distinguishing such behavior from genuine many-body effects is a very challenging question that remains open to a large extent, both from experimental and theoretical points of view.

6.3. Josephson oscillations in fermionic superfluids

The relation between the superfluid phase and the current, as well as the Josephson–Anderson equation, is a feature that is independent of the bosonic or fermionic nature of the superfluid. In a two-reservoir situation similar to that of the two-mode BEC, fermionic superfluids should thus exhibit plasma oscillations like their bosonic counterpart, whenever the channel operates in a configuration that is close to the tunneling regime. Such an experiment was performed recently in Florence by the group of Giacomo Roati [69], using a thin multimode channel.

The system studied consists of an elongated Fermi gas produced in a crossed optical dipole trap, with an elongated shape and an aspect ratio of 10. The Fermi gas is rendered superfluid by working in the vicinity of the broad Feshbach resonance, realizing the BEC-BCS crossover. Rather than imprinting a two-dimensional channel, a very thin barrier with a short waist of $2\ \mu\text{m}$ and a controlled height was introduced at the center of the cloud, using a highly anisotropic laser beam. While this barrier is thicker than the coherence length of the superfluid in the BEC-BCS crossover regime, it was thin enough for no significant superfluid dynamics to take place in the transverse

directions inside the barrier, thus realizing a Josephson junction, as shown in figure 26(A).

The experiments were initiated by introducing an atom number imbalance $z = \Delta N/N$ between the two sides of the junction. The key to the measurement was the use of a very low atom number imbalance of $z = 0.03(1)$, such that the currents were low enough for the phases in the reservoirs to adjust and the single-mode description to remain valid. A second very important tool was the use of the rapid ramp technique to measure the relative phase of the two sides, using atomic interference after time-of-flight, as shown in figure 26(C). Without this technique, interference fringes cannot be observed away from the BEC regime, as seen in earlier attempts to observe Josephson dynamics with strongly interacting Fermi gases [182].

The dynamics of both the atom number difference and the phase difference is shown in figure 27. It is very similar to that observed with Bose–Einstein condensates in a double well configuration shown in figure 20, and in the case of the molecular regime shown in figure 27(A), these are strictly identical. Qualitatively, this effect was seen to persist over the whole BEC-BCS crossover, highlighting the universality of the Josephson–Anderson equation. Following the model derived for bosons, the observed oscillation frequency is given by $\omega_{\text{J}} = \sqrt{E_{\text{C}}E_{\text{J}}}$, with the charging energy E_{C} arising from the reservoir compressibility and the Josephson coupling strength E_{J}. Calculating the thermodynamic properties of the reservoirs using the measured trap frequencies, and extracting E_{C}, it was possible to directly extract E_{J} across the BEC-BCS crossover. It was found that E_{J} presents a broad maximum at unitarity when measured as a function of scattering length at
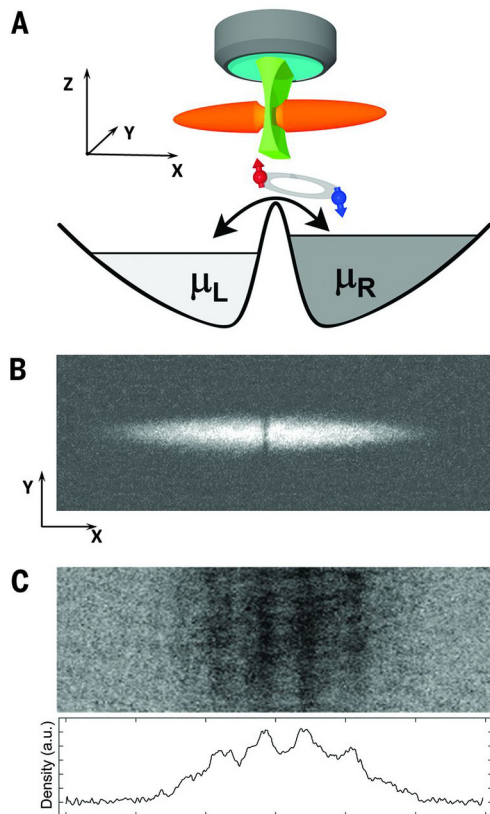
Figure 26. The Josephson junction for superfluid Fermi gases. (A): A schematic of the experimental configuration. (B): The typical absorption picture of a cloud in the presence of a thin barrier. (C): The fringe pattern observed after a rapid ramp and time-of-flight, showing the phase difference between the two sides and allowing the relative phase to be determined. Figure from [69]. Reprinted with permission from AAAS.

a fixed total atom number and the fixed height of the barrier. It arises due to the competition between the increase of the chemical potential when going from the BEC to the BCS side, which decreases the relative strength of the barrier, and the reduction of the paired fraction associated with the reduction of the strength of attractive interactions when going towards the BCS regime.

When using larger initial imbalances or higher barriers, the system was seen to enter a regime of exponential decay of the initial imbalance, qualitatively similar to that of [19] and presented in section 6.1. In this regime, phase coherence was maintained inside the reservoirs, as proved by the survival of the interference contrast observed in the time-of-flight, as shown in figure 28(A). The onset of resistive flow leading to the exponential regime was attributed to vortex nucleation. Direct evidence for the vortices inside the reservoirs was observed in some experimental pictures in this regime. The probability of vortex occurrence in the measurements was measured as a function of the height of the barrier in the unitary regime, showing a threshold above a critical height of about $1.5E_F$ with $E_F = \hbar\bar{\omega}(6N)^{1/3}$ the Fermi energy of the trapped gas. The findings in this regime are presented in figure 28(B). A full map of the onset of dissipation in the BEC-BCS crossover was obtained as a function of both barrier height and interaction strength, and presented in figure 28(D).

The dissipative regime observed in this experiment is the counterpart of the self-trapping regime observed in the case of a small Bose–Einstein condensate in the double well configuration. The qualitative difference between the two experiments is the geometry used, with much larger reservoirs and weaker trapping in the case of the Fermi gas. This allows for a breakdown of the two-mode approximation, with the possibility of a phase dynamics to take place inside the junction, where the vortices are nucleated and later move inside the fluid, generating dissipation.

Despite the wide differences in geometry, in interaction strength and even in the quantum statistical nature of the particles, the similarities between the Bose–Einstein condensate superfluid circuits in the ring geometry and the double well, multimode configuration are striking. The unifying concept of phase coherence and the existence of the superfluid order parameter covering both Bose and Fermi superfluids, together with the fundamental Josephson–Anderson equation are very powerful tools for describing complex geometries and non-equilibrium dynamics. This adds to the very large body of evidence for the universality of these concepts, which has already been collected in the context of superfluid helium [139, 141].

6.4. Superfluid Fermions in the single-mode regime

The fact that the phenomenology of superfluid weak links, such as the Josephson effect, does not depend on the bosonic or fermionic nature of the underlying particles, is a remarkable feature. This has actually played an important role in the history of the understanding of the physics of superfluidity [159, 183]. Except for the quantitative evolution of the coupling constants, the observations of the Florence group [69] indeed demonstrate the universal character of superfluid dynamics from the Bose–Einstein condensate regime to the BCS regime.

An important question is therefore whether some transport phenomena could reveal the fermionic or bosonic character of superfluids, beyond the Josephson–Anderson relation. For BCS superfluids, pair-breaking excitations have no bosonic counterparts, and play a central role in situations where part of the system is in the normal state and exchanges particles with the superfluid. The case of metallic weak links in superconductors is emblematic of this situation [184, 185] (see [186] for a recent review). We now present an experiment where such effects have been probed using superfluid Fermi gases contacted via a quantum point contact [24].

This experiment uses a setup which realizes the quantum point contact (QPC) used for the observation of quantized conductance presented in section 4, but uses atoms in the unitary regime. In particular, the use of an attractive gate potential (with strength V_g) in the QPC region allows for independent control over the chemical potential relevant to transport, at the fixed temperature imposed by the reservoirs. The unitary gas is a particularly simple situation, despite the large interactions, since all the energy scales are universal functions of the fugacity, and at low temperature are just proportional to the Fermi energy. This allows, in particular, for reliable thermometry
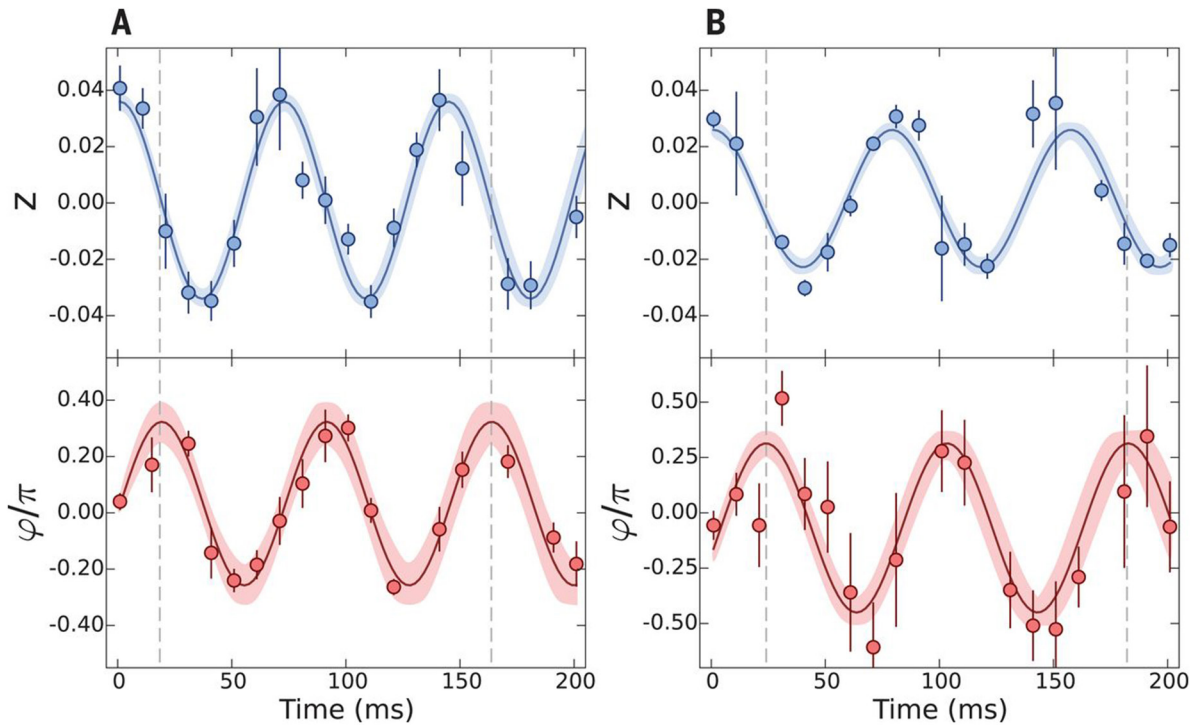
Figure 27. Plasma oscillations in a superfluid Fermi gas. The population imbalance oscillations (top row) and phase difference (bottom row) oscillations in quadrature, on the BEC side of the resonance $1/k_F a = 4.3$ (A) and at unitarity (B). The height of the thin barriers is equal to μ and $1.1\,\mu$ respectively. Extracted from [69]. Reprinted with permission from AAAS.

thanks to detailed knowledge of the temperature-dependent equation of state [95, 97, 99].

The main finding is that in the single-mode or few-mode configuration of the QPC, the linear response breaks down and a nonlinear relation between the current and bias emerges. This is presented in figure 29, where the time evolution of the atom number imbalance is presented as a function of time, showing an obvious nonexponential decay of imbalance for all strengths of the gate potential. Differentiating this data, a current-to-bias relation is obtained confirming the nonlinearity. In order to facilitate the comparison with a microscopic model, the current-to-bias relation is normalized to the estimated value of the pairing gap Δ at the center of the QPC [187], based on the potential landscape and neglecting quantum corrections due to the tight confinement inside the QPC and in the confined region. This model describes multiple Andreev reflections in the QPC leading to a finite DC current, which drops sharply at very low bias, signaling the crossover to the Josephson regime, which was not observed in this experiment. The theory (solid lines in figure 29) reproduces the data with the transmission coefficient for each channel as a free parameter.

The physics of multiple Andreev reflections in a QPC can be understood as the coherent tunneling of several pairs across the quantum point contact. In the presence of a finite bias $\Delta\mu$, which is small compared to the pairing gap, the energy acquired by a pair upon crossing the contact is $2\Delta\mu$. Due to the gap, this energy cannot be released into the bulk of the reservoirs, and thus unitary evolution drives the system back to its initial state after a time $\sim \hbar/\Delta\mu$, i.e. the system performs Josephson oscillations. However, coherently combining

$n/2$ pair tunneling events yields an energy gain of $n\Delta\mu$. For any finite bias, there exists an n for the nth order process to yield enough energy to create a pair-breaking excitation above the gas. This process is called multiple Andreev reflection of order n, and it can yield a DC current through the QPC, as opposed to Josephson oscillations where the current averages to zero over one cycle. It is conceptually similar to Doppleron resonances in the physics of laser cooling [188], or to Wannier–Stark resonances in optical lattices [189]. Whenever the transmission probability α is smaller than one, the nth order process has a probability of order α^n, thus the DC current through the QPC is exponentially suppressed at low bias. The order of Andreev reflections at which the DC drops gives indications of the value of α. In the experiment, this is the way α is fitted on each curve using the theory. The fitted values are presented as insets in figure 29, showing very large values, compatible with the observation of quantized conductance in the noninteracting case.

The agreement with the data provides indirect evidence of multiple Andreev reflections in the cold atom context, where interactions are very strong[10]. More direct observations of multiple Andreev reflections have been observed in solid-state superconductors, in the form of resonances at biases that are equal to integer fractions of the pairing gap [185, 192]. This structure is not visible in the data on cold atoms, because the large transmission probabilities make it very weak, and the signal to noise ratio for current measurements is too low.

---

[10] Andreev bound states were invoked to explain measurements on solitons in the BEC-BCS crossover in [190], but dismissed in later measurements [191].
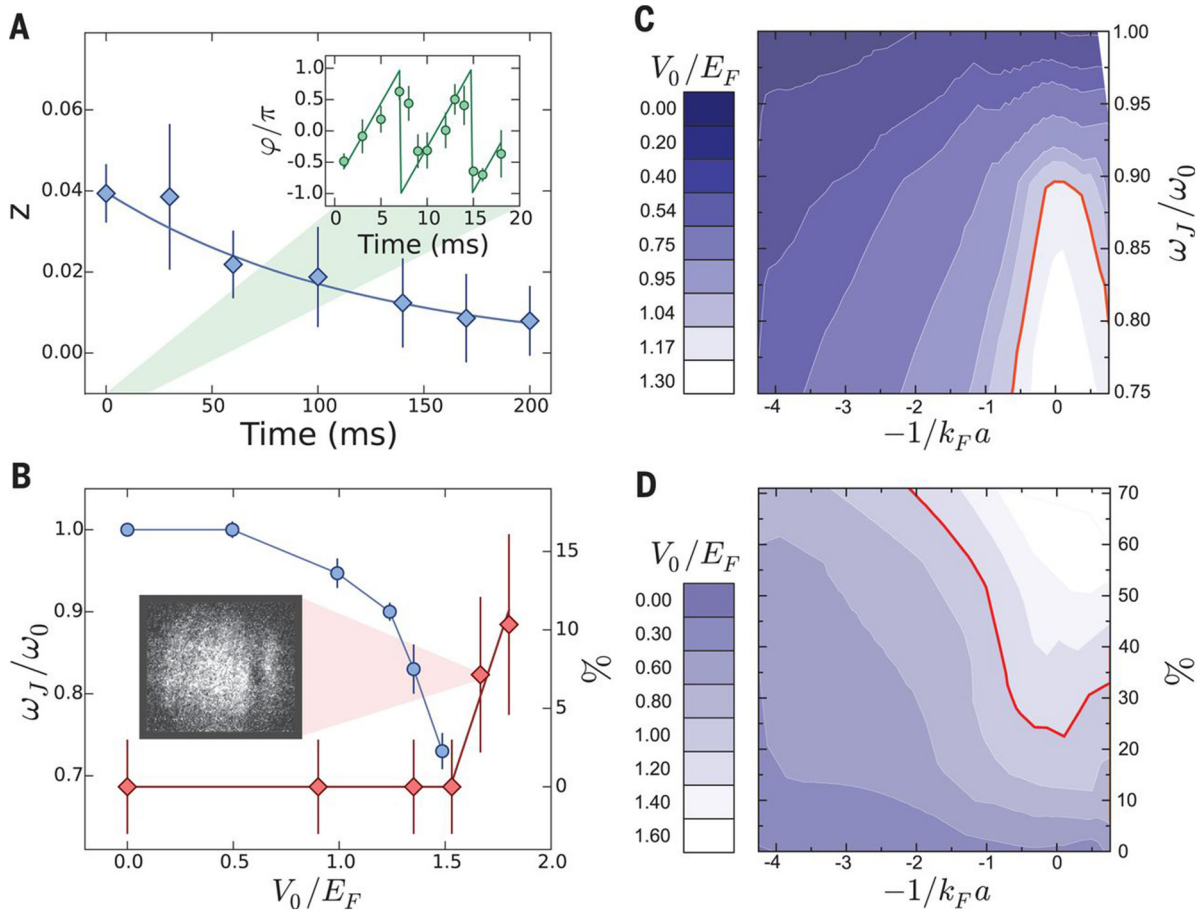
Figure 28. The onset of dissipation. (A) The time evolution of the population imbalance for a large initial imbalance (blue diamonds) with an exponential fit to the data. The inset shows the time evolution of the phase for the same initial parameters. (B) The vortex occurrence probability, evaluated over a collection of 40 independent time-of-flight images (red diamonds, right axis), and a normalized plasma frequency (blue circles, left axis) as a function of relative barrier height at unitarity, for an initial imbalance of 0.04. The inset shows a typical image of one vortex, recorded after a 10 ms time-of-flight expansion. (C) The contour plot of the relative plasma frequency versus interaction strength for different barrier heights. (D) as in (C), but for the probability of vortex occurrence. Extracted from [69]. Reprinted with permission from AAAS.

The indications of Andreev states in cold atomic gases is an important step, since they are one of the simplest nontrivial bound states to appear at the interface between normal and superfluid phases. For more complex structures, such as spin-dependent or spin–orbit coupled contacts, more exotic states can appear such as Shiba [193] or Majorana states [194, 195].

6.5. Superfluid transition and the intermediate interaction regime

Besides the two special cases of noninteracting particles and unitary limited scattering, which have been described above, the general question of the interplay of quantized conductance with many-body correlations can be approached using the control offered by cold atom settings. The cases of intermediate interactions and finite temperature are more difficult both from the conceptual and experimental point of view, because the addition of energy scales or length scales to the problem reduces the degree of universality, making it more difficult to draw general conclusions from the particular experimental conditions. Nevertheless, starting with the well-understood situations of universal conductance quantization or nonlinear superfluid flow described by multiple Andreev reflections,

one can introduce deviations in a systematic way and observe the outcomes on the transport properties. This was performed again using the single-mode QPC.

The first set of measurements used the unitary Fermi gas, where the multiple Andreev reflection picture holds at low temperature, and the temperature was increased up to the expected critical temperature [24]. The results are presented in figure 30. Upon increasing the temperature, the nonlinear current-to-bias relation was observed to disappear and a linear regime was recovered. The measurements were, however, found to deviate strongly from the finite temperature mean-field theory that was successfully used to reproduce the low-temperature superfluid data. In particular, even in the linear regime, the conductance of the channel was much larger than expected from the mean-field theory, i.e. the predictions of the Landauer formula for noninteracting particles. On the one hand, this is not surprising, since even in the nonsuperfluid phase, the system remains strongly interacting. On the other hand, it gives indications that in the normal phase, the correlations remain strong enough to prevent a description in terms of noninteracting fermionic quasiparticles.

A second set of experiments was performed at a low temperature as a function of interaction strength, covering the
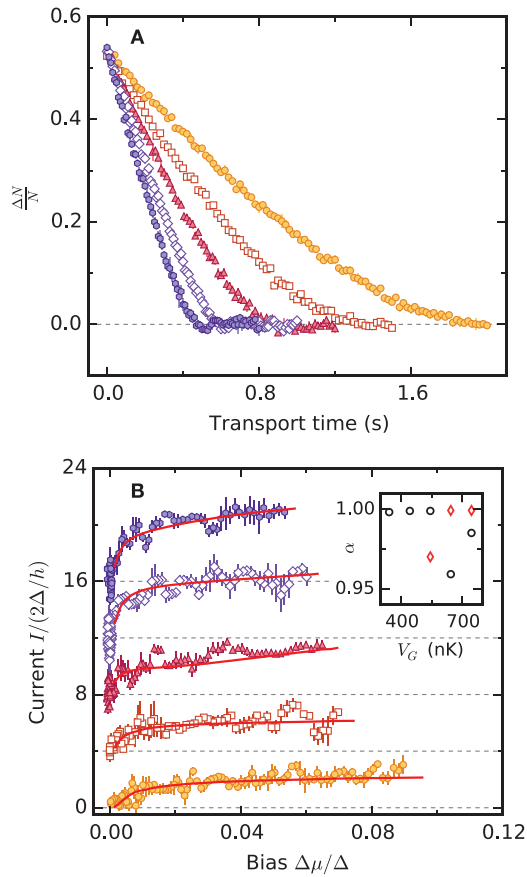
Figure 29. The nonlinear characteristic of the QPC. (A) The time evolution of the particle imbalance $\Delta N/N$ for the gate potentials $V_g = 341$ nK (filled circle), 443 nK (open square), 544 nK (filled triangle), 645 nK (open diamond) and 747 nK (filled hexagon). (B) Current-bias characteristics normalized with respect to the superfluid pairing gap Δ. The error bars represent the variation of three averaged data sets. The negative values of the current are artifacts from the numerical derivation process. The red lines show the result of Keldysh calculations with the transparency α of the QPC as the only free parameter. For clarity, the curves are shifted vertically by four units; temperature is 100(4) nK for all data sets. Inset: the fitted transparency α for the various gate potentials; black circles refer to the lowest mode, and red diamonds refer to the next two degenerate modes, when present.

regime from unitarity to weak attraction, where the low but finite temperature leads to a normal phase [25]. For the weakest attractions, quantized conductance is observed with a plateau at $1/h$, in agreement with the expectations of the Landauer formula, including a mean-field effect reducing the length of the plateau. Upon increasing the strength of attractive interactions, the plateau was preserved but it was observed to continuously shift to higher conductances. These observations are presented in figure 31. For large densities or stronger interactions, the plateau fully disappeared and a nonlinear current-bias relation was recovered, as expected from multiple Andreev reflections in the contact.

One difficulty in interpreting this data is the fact that the equation of state changes as the interactions are varied across the BEC-BCS crossover. In particular, the finite temperature effects have to be evaluated in order to obtain a faithful estimate of the critical temperature and the part of the parameter
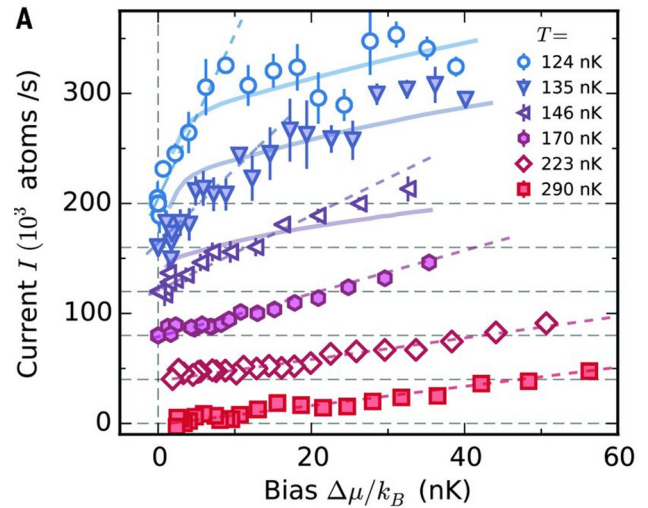

Figure 30. Nonlinear current-bias relation for increasing temperatures. The temperature is increased from 124 nK up to 290 nK. The nonlinearity, which is evident at low temperatures, disappears with an increasing temperature. The multiple Andreev reflection theory at a finite temperature is presented in solid lines, already showing strong deviations at 146 nK. The dashed line is a fit to the initial part of the curve to guide the eye. Figure extracted from [24]. Reprinted with permission from AAAS.

space where the system is expected to be superfluid. This was done using state-of-the-art theoretical calculations for the critical point [196], the measured ground state equation of state in the BEC-BCS crossover [98] and the finite temperature corrections to the first order in the interactions, extrapolated to the strongly interacting case where perturbation theory was breaking down. Applying this procedure allowed for the extraction of the conductance in the single-mode regime (the center of the plateau in the weakly interacting case) as a function of T/T_c, where T_c is evaluated from the theory [196] at the entrance and exit of the QPC where the density is the highest, using the equation of state [98]. The result is presented in figure 32, where the systematic deviation of the conductance from $1/h$ is obvious, even way above the expected transition temperature.

Two interpretations of these deviations from the conductance quantum predicted by the Landauer formula have been formulated.

(i) The first explanation put forward in [197–199] focuses on the physics of the reservoirs, pointing out that even above the superfluid transition, the strongly attractive Fermi gas can still show deviations from the conventional Fermi liquid picture, as seen in previous experiments in the BEC-BCS crossover [200, 201]. Some superfluid correlations can persist over a finite but long range, in particular in the vicinity of the transition. The critical regime, with the slow power law decay of the superfluid correlations, extends up to $2T_c$ [202, 203]. To explain why such slowly decaying (power law) superfluid correlations could influence the conductance, one can compare them with another system with such power law correlations—namely the Luttinger liquid in one dimension—where the physics that gives rise to the power law superfluid correlations also gives rise to enhanced conductance compared to $1/h$ [204].
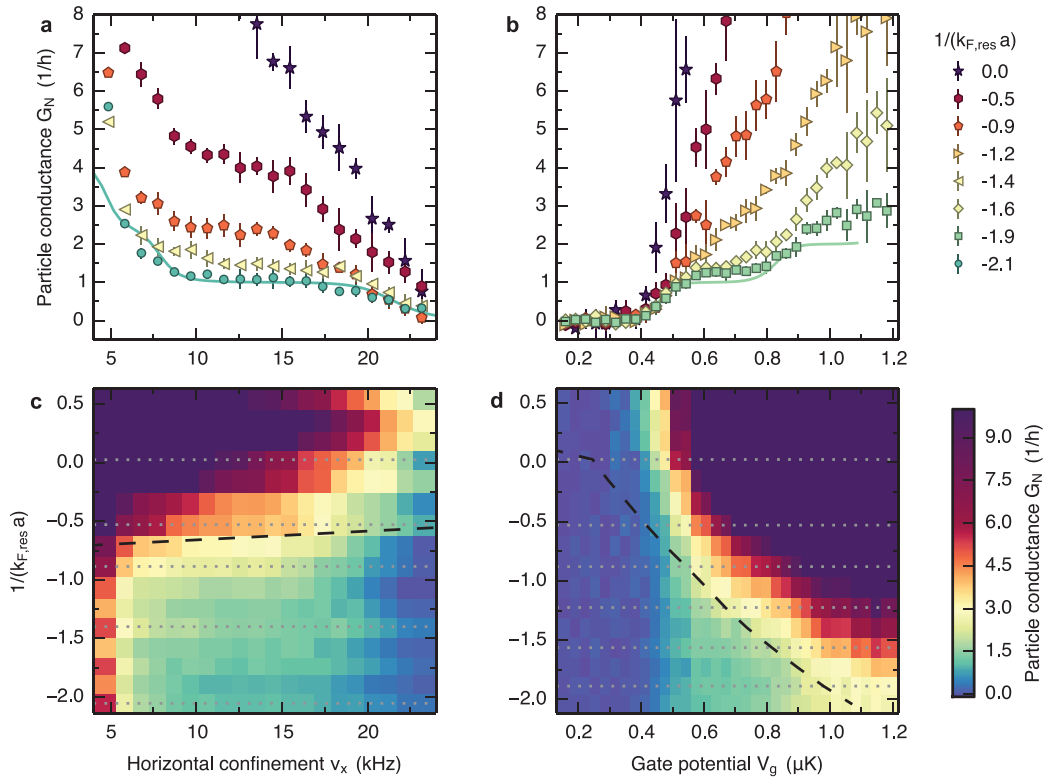
Figure 31. Particle conductance of the attractively interacting Fermi gas. (a) Particle conductance G_N as a function of the horizontal confinement frequency ν_x of the QPC, at a fixed gate potential $V_g = 0.42\ \mu$K; and (b) as a function of the gate potential V_g at a fixed confinement frequency $\nu_x = 23.2$kHz, for different interaction strengths $1/(k_{F,res}a)$ in the reservoirs. The solid lines are theoretical predictions for $1/(k_{F,res}a) = 2.1$ and 1.9 respectively, based on the Landauer formula including mean-field attraction (methods). Each data point represents the mean over five measurements and the error bars indicate one standard deviation. (c) and (d) A two-dimensional color plot of G_N as a function of interaction strength $1/(k_{F,res}a)$ and horizontal confinement (c) or gate potential (d). Both plots contain the cuts of (a) and (b) (gray dotted lines), and an estimation of the local superfluid transition at the QPC exits (dashed black line). Reproduced with permission from [25].

(ii) The second explanation, described in [120], focuses on the physics of the channel, in particular the fact that confinement enhances the attraction inside the channel compared to the reservoirs, which leads at finite temperatures to a situation where the reservoirs are in a normal state, but superfluidity persists inside the QPC. Then, Andreev reflection processes take place at the entrance and exit of the QPC, leading to enhanced conductance up to a factor of two. The key to explaining the continuous increase of the conductance up to higher values is to realize that the position at which the superfluid to the normal interface exists can be outside the single-mode region, and thus Andreev reflections take place in several channels in parallel.

The very different nature of these explanations illustrates the richness of the physics of cold gases in mesoscopic structures. Whilst the signal-to-noise ratio is smaller than in state-of-the-art condensed matter physics experiments, the microscopic Hamiltonian is known *a priori*, and unexpected features can arise due to the interplay of strong interactions with finite size and nonequilibrium.

6.6. Spin transport in interacting Fermi gases

The spin degree of freedom plays a fundamental role in the physics of Fermions, since it is the degree of freedom that allows for interactions between particles. There is a fundamental difference between the spin and particle currents regarding the effects of interactions: since scattering conserves the total momentum, the total current of particles is not expected to be affected by the interactions. In contrast, scattering does not conserve spin currents and is thus damped by interactions, as observed already in the early experiments on Fermi gases [205, 206].

Several experiments have investigated spin transport in interacting Fermi gases, using configurations close to the two-terminal setup. In particular, in the seminal experiment [70] a two-component Fermi gas is first cooled to low temperatures, then the two spin components are separated in the absence of interactions, using dipole oscillations in a spin-dependent harmonic trap produced at a low magnetic field. When the two parts oscillate in phase opposition, interactions are restored by ramping up the magnetic field in the vicinity of the Feshbach resonance. The relative motion of one component with respect to the other is monitored as a function of time. For short times the two spin components keep oscillating and bounce on each other. In this regime, the dynamics is dominated by the oscillations in the reservoirs, and interactions prevent the two spins from diffusing through each other. On longer time scales, the oscillations damp, and an exponential decay of the spin-dipole is observed, corresponding to the slow diffusion of one component through the other. This is illustrated in figure 33.
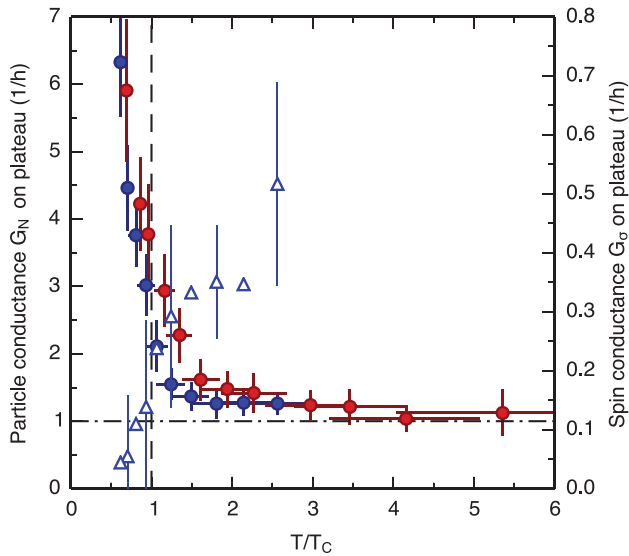
Figure 32. Particle and spin conductance in the single-mode regime. G_N (closed circles) and G_σ (open triangles, every second error bar displayed) for various interaction strengths are presented as a function of the reduced temperature T/T_c, which varies due to the dependence of T_c on density and scattering length. Blue data points are obtained from the measurements shown in figure 31(d) and figures 35, for $V_g = 0.64$ μK and $\nu_x = 23.2$ kHz. Red data points are obtained from the measurements shown in figures 31(a), for $V_g = 0.42$ μK and $\nu_x = 14.5$ kHz. G_N tends to the conductance quantum $1/h$ (horizontal dash-dotted line) for weak interactions ($T/T_c \gg 1$). The error bars contain statistical and systematic errors. Reproduced with permission from [25].

Using the average spin current extracted from the dynamics of the center of mass of the clouds, divided by the measured spin gradient in the region where the two components merge, a spin diffusion coefficient was estimated for the unitary Fermi gas as a function of temperature. These results are presented in figure 34. In the high-temperature regime, the evolution of the diffusion coefficient is controlled by the velocity dependence of the scattering cross-section, which is inversely proportional to the square of the relative momentum in the unitary limit, leading to a dependence like $T^{2/3}$. In the degenerate regime, the diffusion coefficient saturates to $1.11\hbar/m$, as the Pauli suppression of collisions gradually cancels the increase of the scattering cross section.

In the homogeneous unitary Fermi gas, dimensional analysis implies that the diffusion coefficient is a universal number multiplied by $\hbar/m$. Indeed, the only length scale is $1/k_F$, so the mean free path has to be a number divided by k_F, and the only velocity scale is the Fermi velocity. However, the measured number is likely to depend on the experimental situation, in particular since the density variations across the trap lead to a position-dependent diffusion coefficient, which cannot be recovered based on a local density approximation only (since the direction of the current density cannot be inferred from the distribution only). Direct experimental evidence of the effect of the trapping potential was found when these experiments where reproduced in the presence of a spin imbalance, where a paired core forms at the center of the trap with the excess particles repelled at the side where they form a ballistic shell. The paired core was observed to move through the unpaired atoms [110].
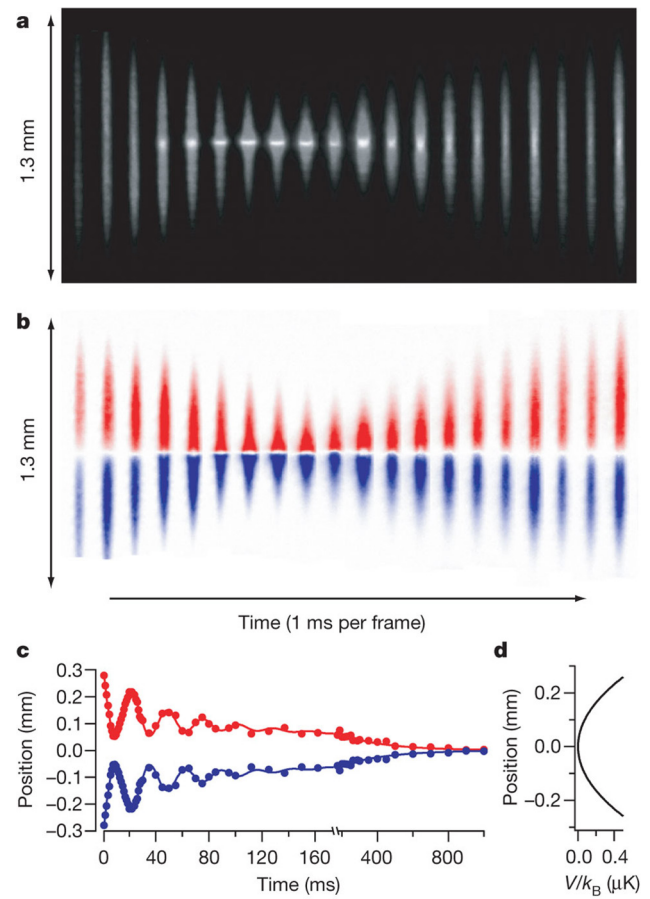

Figure 33. Observation of spin transport in the collision of two spin-polarized clouds. The total column density (a) and difference in column density (b) as a function of time. (c) The time evolution of the average position of the spin-up and spin-down atoms, showing a transient oscillating regime followed by slow diffusion. (d) Trapping potential. Reprinted by permission from Macmillan Publishers Ltd: Nature [70], Copyright (2011).
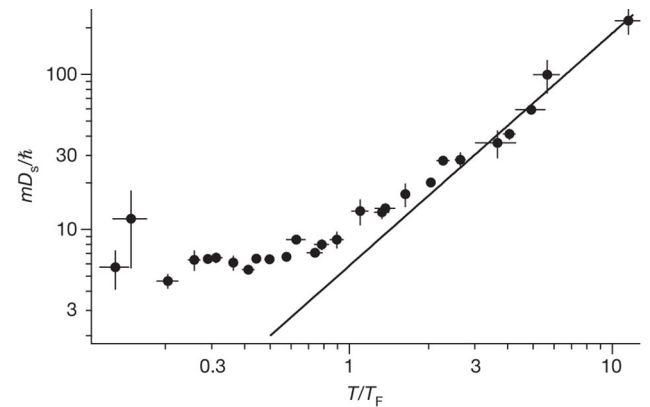

Figure 34. Spin diffusion coefficient for the trapped gas, as a function of temperature, for the unitary Fermi gas. The solid line shows a $T^{3/2}$ trend expected at a high temperature. For a low temperature, the diffusion coefficient approaches a constant limit. Reprinted by permission from Macmillan Publishers Ltd: Nature [70], Copyright (2011).

These experiments raised two important questions regarding spin transport. The first one is the long-standing question of the possible ferromagnetic instability on the molecular side of the Feshbach resonance. Indeed, as the two clouds collide,
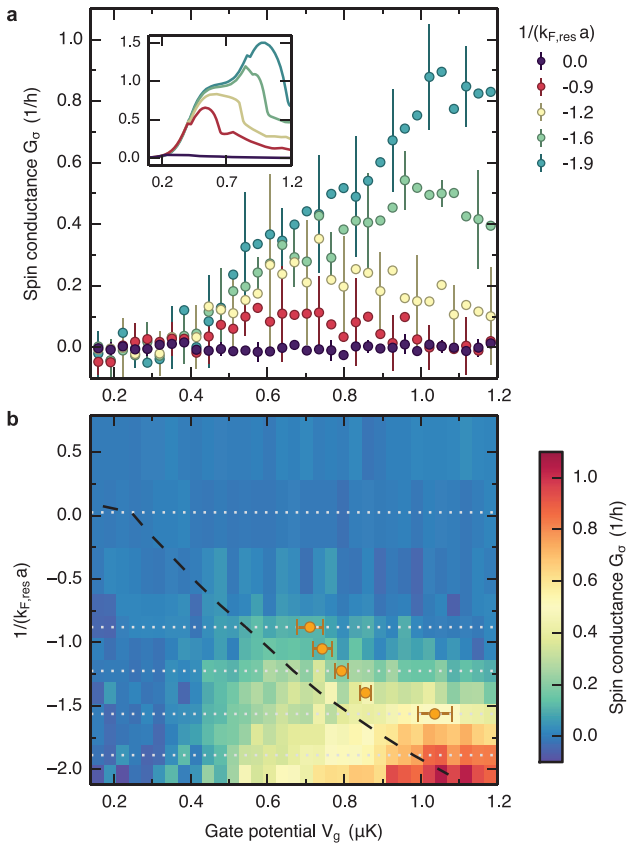
Figure 35. Spin conductance of the attractively interacting Fermi gas. (a) Spin conductance G_σ as a function of the gate potential V_g for different interaction strengths $1/(k_{F,res}a)$ in the reservoirs. Each data point represents the mean over nine measurements, and error bars indicate one standard deviation plotted for every third point. Inset: G_σ obtained from a mean-field phenomenological model, reproducing the nonmonotonic behavior of the experimental data. (b) A two-dimensional color plot of G_σ as a function of $1/(k_{F,res}a)$, with cuts of (a) indicated as gray dotted lines. The points where G_σ is maximum, obtained from a parabolic fit along V_g, are displayed as orange circles for comparison. The dashed black line represents the superfluid critical line estimated at the entrance and exit regions of the QPC, using the results of [196]. Reproduced with permission from [25].

atoms explore the upper branch of the Feshbach resonance, leading to repulsive interactions before three-body recombinations allow the formation of bound molecules. Very similar spin transport measurements were performed recently with the goal of studying the possible metastable ferromagnetic state emerging in the molecular regime of the Feshbach resonance. Several pieces of evidence were gathered, in particular, the softening of the spin dipole mode—even though the dynamics remains dominated by the underlying molecule formation [207].

The second question is the effect of pairing on spin transport. This was indirectly observed in [110], where the spin separation followed by relaxation was reproduced in the presence of a partial spin polarization, and at low temperatures. Due to the inhomogeneous nature of the system, the spin currents consisted of unpaired particles expelled from the center of the trap [155, 208] and flowing in the wings of the cloud.

These effects have been investigated using the two-terminal configuration with the quantum point contact in [25], exploring the low-temperature regime with varying interaction strengths in conditions identical to those of the conductance at the emergence of superfluidity in the previous section. A partial spin separation is produced following a procedure similar to that of [70], yielding reservoirs with identical chemical potential but opposite spin polarization. The crucial difference with [70, 110] is the fact that in the presence of superfluidity, the point contact geometry forces the spin current to occur at the center of the cloud, along the longitudinal direction only, forcing the spin current *through* the superfluid.

The analysis follows the linear response model of section 2. The spin current is written within the linear response as $I_\sigma = G_\sigma \Delta b$, with $\Delta b = (\Delta\mu_\uparrow - \Delta\mu_\downarrow)/2$ as the difference between the chemical potential bias for the two spin components. In the absence of net magnetization, symmetry imposes that the spin bias does not couple to particle currents, and the response is only described by the spin conductance G_σ. The evolution of G_σ is presented in figure 35 as a function of gate potential and interactions. For the weakest interactions, spin conductance grows with an increasing gate potential, but with stronger attraction a broad maximum develops, and for the largest gate potentials G_σ decreases with the gate potential, indicating spin-insulating behavior. With increasing interactions G_σ decreases earlier, and is entirely suppressed upon approaching unitarity. For the fixed temperature of the reservoirs, increasing the gate potential increases the density, which brings the system into the superfluid phase beyond a critical value. This transition line was estimated using a theory like that for particle transport, with the boundary shown in figure 35(b). The regime of vanishing spin conductance coincides with the expected superfluid regime, where very large particle transport is observed (see figure 31).

The spin-insulating character of the BCS superfluid is expected as a result of the spin-singlet character of the pairs. The pairing gap acts as a spin-gap-separating singlet from triplet excitations. In this sense, the QPC in the superfluid regime acts as an efficient singlet filter. As a consequence, within the BCS framework, the magnetization is exclusively carried by excitations above the gap, which are the Bogolyubov quasiparticles. They form a ballistic, free Fermi gas, for which a Landauer formula can be written. In a semi-classical approximation, the large pairing gap in the QPC region acts like a repulsive barrier for the excitations, effectively closing the contact and thus suppressing spin transport. Based on such a model, the spin conductance was estimated (see inset in figure 35(a)), with a qualitative agreement with the data. A better agreement was found using the sophisticated model of [120], which also reproduces the anomalous conductance plateau for particle transport.

These spin transport experiments are focused on magnetization transport, i.e. longitudinal spin transport; the case of transverse spin diffusion, focusing on the decoherence of spin textures imprinted on the atomic cloud, is different, and is not studied using the two-terminal configuration, but rather as a quench experiment [72, 73, 75].

7. Perspectives

The investigations of mesoscopic transport phenomena using cold atoms is only in its infancy. The experiments are so far at the status of proofs of principle. Nevertheless, several new insights have already been gathered about transport physics, including a few novel features that were not anticipated based on the existing knowledge of the condensed matter physics community. The extension of cold atoms into the field of mesoscopic transport is a very exciting perspective, and we expect that the interaction between the two fields will lead to important progress in the next few years. We now present a list of challenges and perspectives for future developments. This is by no means exhaustive, and reflects our main interests at the time of the writing.

7.1. Technical developments

Experimental techniques are improving fast, in particular in the variety of mesoscopic structures that can be produced and investigated. In this respect, the growing use of holographic projection techniques in cold atom experiments opens perspectives for fully programmable potential landscapes, implemented using computer-programmed holograms that even provide dynamical control [209]. In the near future, this will allow the projection of the tunnel barrier, and short scale potentials with large interference effects, such as quantum dots or mesoscopic lattices. The progress in detecting atoms at the single-atom and single-site level in optical lattices could also be used in order to investigate the details of atomic distribution inside driven mesoscopic structures [9–14]. Combining these high-resolution techniques with automated processes for the optical control of potential landscapes could lead to fully integrated simulation machines, taking as input Hamiltonian parameters and allowing the transport coefficients to be read out, similar to a high-performance simulation facility. This would indeed come close to the practical implementation of a quantum simulator as envisioned by Richard Feynman [210, 211].

A major limitation of the currently used systems is the difficulty in measuring very low currents—below 1000 atoms per second—expected when the atoms in the channel are in an insulating state. The main problem is the reproducibility of the preparation of the system: first, atom number fluctuations are on the order of a few percent, then the separation in two reservoirs also introduces extra noise. Therefore, the outcome of atom number measurements in the reservoirs fluctuates by typically a thousand atoms from one realization to the next. Upon averaging, this yields to the typical error bars shown in figure 17. In addition, drifts inherent to long-term, systematic measurements limit the number of consecutive data sets that can be acquired and compared with each other before recalibration is required. In our setup, it was possible to take measurements over five consecutive days for the spin conductance measurements, with realignments approximately every hour. Improving on the preparation techniques could reduce the errors, but eventually the technical stability of the setup is

likely to be insufficient. Remarkably, the preparation of initial bias in a small ensemble of atoms out of a Mott insulator using quantum gas microscopes reaches limitations in the reproducibility of the same order [107].

Here, techniques based on quantum nondemolition measurements can track the population inside the reservoirs in real time with very high precision, using, for example, a high-finesse cavity as a detector [212, 213]. This opens the perspective of an atom-by-atom measurement of currents, allowing for a full counting analysis of currents in mesoscopic structures [214, 215]. This would also allow two-terminal measurements to be performed with optical lattices in the Hubbard regime. Indeed, placing the atoms in a lattice increases the effective mass of the particles, slowing down the dynamics of the reservoirs, and thus the time scale where meaningful conductance measurements can be performed. In addition, the current is limited by the band width which is exponentially reduced in the Hubbard regime [3]. Because of the relevance of lattice systems to condensed matter physics, and the ability they have to operate in the strongly repulsive regime, the extension of conductance measurements to lattices would be an important breakthrough.

7.2. Transport at quantum phase transitions

Thanks to the control of the experimental parameters, cold atoms can be precisely tuned at quantum critical points, such as the superfluid-to-Mott insulator transition [152]. On the one hand, the universal character of the physics in the vicinity of such a transition makes it of interest, in particular, for comparison with theory and across different fields of physics, but on the other hand, the lack of a quasi-particle description of the excitations makes the system challenging to describe (see [216] and references therein).

A two-terminal configuration allows for the direct measurement of conductance for a mesoscopic system tuned at a critical point, such as a two-dimensional system of bosons close to the superfluid-to-Mott insulator transition [217, 218]. Connecting this system to large reservoirs can be done as described in section 4, and the conductance in the critical regime can be directly accessed, providing a direct testbed for theoretical predictions. Of particular interest would be the ability to make quantitative predictions, controlling the effects of finite size. This can be performed using programmed, controlled potentials, which allow a finite size scaling analysis, extraction of the intrinsic length scales from the size dependence of the conductance, and extrapolation to an infinite size limit.

7.3. Emergent states at the interfaces

The interplay of the connection to reservoirs with interactions inside the contact, as provided by mesoscopic cold atomic gases, is a natural environment for studying the effects of interfaces. An archetype of such a state is the Andreev bound state inside a quantum point contact connected to superfluids (see appendix for more details). Such a system is the subject

of ongoing research in condensed matter physics, in particular, as a resource for quantum information processing [219]. For more complex structures, which could include spin–orbit coupling or artificial gauge fields in the contact for instance, the emerging states can have nontrivial topological properties [195]. The use of a contact with large reservoirs may be useful in mitigating some of the heating effects in existing protocols for the implementation of gauge structures with atoms.

Emergent quantum states have been invoked to explain some features observed in electronic systems known as the 0.7 anomaly [220–223]. A cold atomic gas can be used as quantum simulator with tunable interactions in order to investigate these phenomena. In particular, the use of charged neutral particles with short-range interactions, the ability to measure spin conductances, spin drag or thermopower, and the use of attractive or repulsive interactions would be an interesting test-bed for existing theories.

At the same time, the emergent state in the contact could provide cold atom physicists with access to strongly correlated physics like the Kondo effect or quantum magnetism, forming a starting point for the engineering of complex quantum systems with cold atoms.

Acknowledgments

Appendix A. Andreev reflections

The case of a single-mode point contact in between two weakly correlated superfluids is a textbook example of mesoscopic physics, and provides an elegant link between the macroscopic Josephson effect, described by the Josephson–Anderson equation, and the microscopic (even though effective) description of the contact [224] (see [186] for a recent overview).

Consider first a one-dimensional situation with an interface between a superfluid and a normal region located around $z = 0$. Consider now a particle wave packet incident from $-\infty$ with energy ϵ_k above the Fermi energy E_F, such that to first order $\epsilon_k = \hbar k v_F$, with $v_F = \hbar k_F/m$, k_F is the Fermi momentum
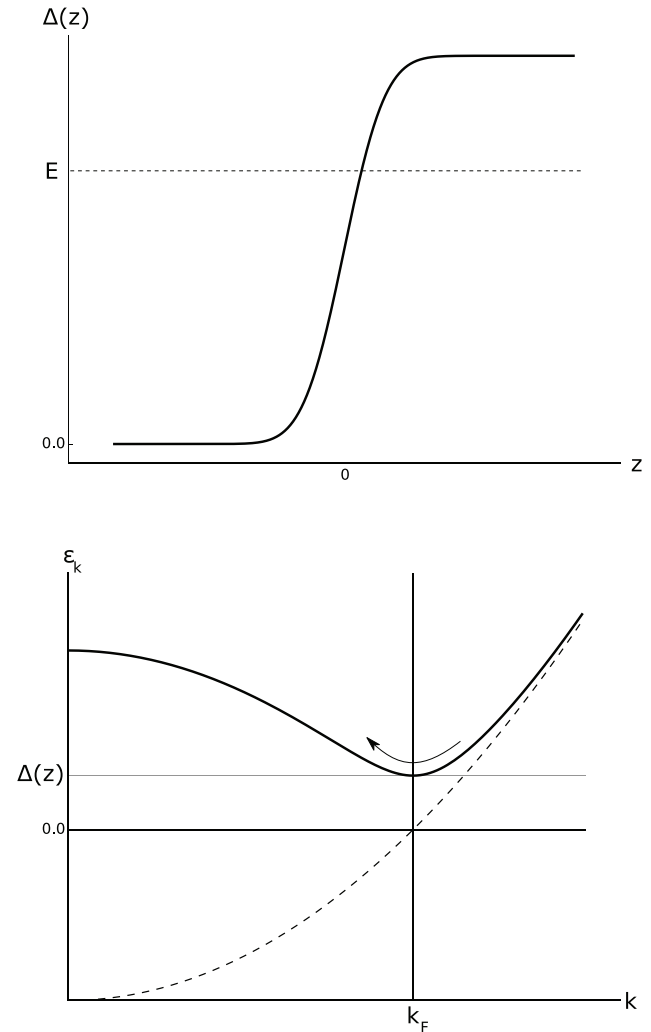

Figure A1. A schematic picture of Andreev reflection. Up: real space variations of the gap with a normal-superfluid interface at $z = 0$. Down: BCS dispersion relation of the quasi-particles at position z for which the gap is $\Delta(z)$.

and the total momentum is $k_F + k$. The total energy of the incident particle is supposed to be lower than $\Delta(+\infty)$, as illustrated in figure A1. We suppose that the gap $\Delta(z)$ varies with position much more slowly than k_F^{-1}, which is consistent with the BCS framework where the fastest variations of Δ are of the order $\xi = \hbar\Delta/v_F$. Thus, we describe the motion of the incident particle semiclassically with a local momentum $k_F + k(z)$ and a local energy $E(z) = \sqrt{\epsilon_k^2 + \Delta(z)^2}$.

The equations of motion for the wave packet are readily obtained:

$$\frac{dz(t)}{dt} = \frac{1}{\hbar}\frac{\partial E}{\partial k} = \frac{\hbar v_F^2}{E}k(t) \tag{A.1}$$

$$\frac{dk(t)}{dt} = -\frac{1}{\hbar}\frac{\partial E}{\partial z} = -\frac{\Delta}{\hbar}\frac{\partial\Delta}{\partial z}. \tag{A.2}$$

The incident wave packet moves at the local group velocity, with a momentum constrained by energy conservation. Since $\Delta \geqslant 0$ and $\frac{\partial\Delta}{\partial z} \geqslant 0$ everywhere, momentum monotonically

decreases during the whole evolution. The group velocity, which is positive when the particle is at $z \ll 0$, cancels at the 'turning point' set by $E(z) = \Delta(z)$. At this point, the momentum of the wave packet is exactly the Fermi momentum, and the quasi particle is an equal mixture of a particle and a hole. The momentum then keeps decreasing and the group velocity becomes negative. The corresponding wave packet still has an overall *positive* momentum (slightly below k_F) and a negative group velocity, thus a hole-like character. In the limit $t \to \infty$, the position of the wave packet goes to $-\infty$ and the wave packet turns into a pure hole-like excitation.

In the frame of the wave packet, the Andreev reflection is equivalent to a Landau–Zener transition, which is well known in quantum optics. The wave packet sees a growing 'driving', represented by Δ, which coherently couples particles and holes of a given momentum, with a resonance at k_F. The semiclassical motion of the wave packet amounts to a slow sweep of momentum across k_F.

It is important to realize that in this process, no actual backscattering takes place: all processes happen in a thin momentum window around $+k_F$, while actual backscattering would connect $+k_F$ to $-k_F$. Since the order parameter cannot vary on the length scale of k_F^{-1} such processes have to originate from another mechanism, such as a sharp jump in the electron density at an oxide interface in condensed matter. Of course the reverse process also takes place, by which a hole is coherently converted into a particle. As usual, the equilibrium situation represents the equilibrium between the particle and hole reflection processes. Accounting for the spin degree of freedom, the hole is reflected with the opposite spin.

Within this description, the total number of particles is only conserved up to the addition or subtraction of any number of pairs in a ground state, which is consistent with the usual mean-field BCS theory. The conversion of a particle into a hole by Andreev reflection is accompanied by the creation of one pair in the condensate in the superfluid part, in the same way as a Landau–Zener transition is accompanied by the absorption of one photon. This also means that an incident pair from the superfluid side is actually coherently converted into a particle–hole pair with conjugated momenta and opposite spin.

This picture does not depend on the details of the connection between the normal part and the superfluid. The normal state does not actually need to be normal—it could just be a region where the gap is lower, and we consider an excitation that has enough energy to live in the low gap region but not in the other.

Appendix B. Andreev bound state

Let us now consider the situation of a weak link between two superfluids. Inside the weak link, a particle incident to a superfluid contact is coherently converted into a hole, which is then coherently converted back into a particle at the other interface. Each of such cycles coherently adds a pair to one contact and destroys one in the other, a process which is sometimes
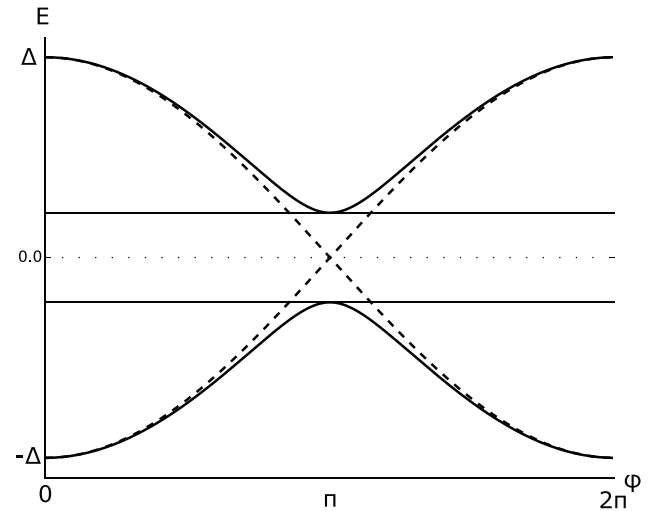

Figure B1. Andreev bound states. The energy of the Andreev bound states as a function of phase difference, without (dashed line) and with (solid line) backscattering mechanisms.

referred to as the 'Andreev pump'. There is, however, a fundamental extra ingredient, namely the relative phase between the two superfluids.

Indeed, following the analogy with a Landau–Zener process, the phase of the superfluid is imprinted onto the outgoing hole upon Andreev reflection. When the hole is converted back into a particle upon Andreev reflection on the second contact, the phase difference is imprinted onto the excitation, and interference with the original state takes place.

Writing down the condition for constructive interference inside the weak link, one obtains a pair of eigenenergies $E_\rightarrow(\phi)$ and $E_\leftarrow(\phi)$, which lie below the pairing gap, corresponding to two bound states $| \rightarrow \rangle$ and $| \leftarrow \rangle$, which depend on ϕ, the phase difference between the two superfluids $E_\rightarrow(\phi) = -\Delta \cos\frac{\phi}{2}$, and $E_\leftarrow(\phi) = -E_\rightarrow(\phi)$. Here we have supposed that the length of the weak link is shorter than the coherence length of the superfluid, such that the phase accumulated due to free space propagation inside the link is negligible. These carry a current $I_j = -\frac{2}{\hbar}\frac{\partial E_j}{\partial \phi}$, $j = \leftarrow, \rightarrow$. For $\phi < \pi$, the ground state is $| \rightarrow \rangle$, which carries a positive current, and for $\phi > \pi$ the ground state is $| \leftarrow \rangle$ carrying a negative current. This corresponds to the idea that the current is directed in the direction of the phase gradient. The two states $| \rightarrow \rangle$ and $| \leftarrow \rangle$ are associated with wave packets, performing oscillations around $+k_F$ and $-k_F$ respectively. For $\phi = \pi$, the two states are degenerate.

In the presence of a backscattering mechanism, yielding a transparency for the weak link $\alpha < 1$, the two states $| \rightarrow \rangle$ and $| \leftarrow \rangle$ are coupled. Inside the weak link, a left-propagating particle can be coherently backscattered into a right-propagating particle with a probability of $1 - \alpha$. This coherent coupling lifts the degeneracy of the $| \rightarrow \rangle$ and $| \leftarrow \rangle$ states around $\phi = \pi$. The new eigenstates are $|+\rangle$ and $|-\rangle$ with energies $E_\pm = \pm \Delta \sqrt{1 - \alpha \sin^2(\frac{\phi}{2})}$, as presented in figure B1.

In the presence of a weak tunnel barrier, $\alpha \ll 1$, this model reproduces the Josephson effect, where to the first order the current exhibits sinusoidal oscillations. In the presence of a bias between the two reservoirs, the phase difference increases linearly in time. When the bias is smaller than the gap, the systems evolves adiabatically along the state $|-\rangle$, which is the ground state of the system. This yields an oscillating current as an admixture of $|\rightarrow\rangle$, and $|\leftarrow\rangle$ oscillates in time. Using the relation $I = -\frac{2}{\hbar}\frac{\partial E}{\partial \phi}$ we obtain the Ambegaokar–Baratoff formula for the maximum current sustained by the junction $I_c = \frac{\pi\Delta}{2}G_n$, with $G_n = \frac{2}{h}\alpha$ as the conductance in the normal state given by the Landauer formula[11]. Remarkably, adding several channels in parallel with difference transmissions does not alter the phenomena, since the phase difference and the frequency is identical for all channels. This explains the robustness of the Josephson oscillations to trap averaging and other imperfections.

Appendix C. Multiple Andreev reflections and dissipative flow

In the absence of dissipation, i.e. in the fully adiabatic limit, applying a bias to the junction yields Josephson oscillations that average out to zero in the DC limit, leading to zero DC conductance. However, with a finite bias, there is a nonzero probability of performing a Landau–Zener transition from the ground Andreev state to the excited one, which then leads to a finite current in the DC limit. Upon sweeping the phase, one single particle excitation is taken at $-\Delta$ and 'lifted up' above the gap via the Andreev bound states and the Landau–Zener transition, creating one excitation. The probability of a non-adiabatic transition is given by the Landau–Zener formula $p = e^{-\frac{\pi(1-\alpha)\Delta}{\Delta\mu}}$, where $\Delta\mu$ is the bias. A crossover from adiabatic Josephson oscillations and dissipative current occurs when $\Delta\mu \sim \pi(1-\alpha)\Delta$. For very good contacts with $\alpha \leqslant 0.95$, like in our experiment, this crossover takes place for a very low bias.

Dissipation and DC currents also occur via a resonance mechanism named multiple Andreev reflections. This can be understood by considering the energy needed to create one single-particle excitation. When $\Delta\mu < 2\Delta$, the bias is not large enough to directly break the pairs. However, upon transferring one pair from the high chemical potential lead to the low chemical potential one, an energy of $2\Delta\mu$ is acquired. Coherently adding $n/2$ pair transfer events can create a single-particle excitation provided $\Delta\mu \leqslant \frac{2\Delta}{n}$, where n here is the number of Andreev reflections involved in the process, or the order of the process. Since each Andreev reflection involves the transmission of a particle or a hole through the weak link, an nth order process occurs with a probability of α^n. Upon reducing the bias, the current drops sharply at $\Delta\mu < 2\Delta/n$ for each integer number n, corresponding to the closing of the Andreev reflections of the order of n, leading to a cusp in the current-bias relation, as observed in superconducting point contacts.

[11] Note the factor of 2 due to spin degeneracy, which follows the condensed matter convention in contrast to the discussions of the Landauer formula in the main text.

This process is formally analogous to Wannier–Stark resonances in optical lattices. Consider the conjugated variable to ϕ, namely the pair population difference N. States with a given N are analogous to sites of an optical lattice, and ϕ is the counterpart of the quasi-momentum measuring the phase difference between neighboring sites. The two Andreev bound states, then, are the counterparts of two bands of the lattice. Introducing a bias $\Delta\mu$, leads to an offset $\Delta\mu$ between neighboring sites. When the bias is equal to a fraction of the gap between the two states 2Δ, resonant tunneling can take place from the ground band to the excited band across several sites.

In contrast to the Josephson oscillations, multiple Andreev reflections or the adiabatic-to-dissipative crossover described by the Landau–Zener formula is specific to a single-mode junction. In the multimode case, a different order of reflections take place in the different channels, and the crossover to dissipative currents takes place for a different bias in each channel, depending on its transmission.

References

[1] Ihn T X 2010 *Semiconductor Nanostructures: Quantum states and electronic transport* (Oxford: Oxford University Press)

[2] Bloch I, Dalibard J and Zwerger W 2008 Many-body physics with ultracold gases *Rev. Mod. Phys.* **80** 885–964

[3] Esslinger T 2010 Fermi–Hubbard physics with atoms in an optical lattice *Ann. Rev. Condens. Matter Phys.* **1** 129–52

[4] Zwerger W 2011 *The BCS-BEC Crossover and the Unitary Fermi Gas* vol 836 (Berlin: Springer)

[5] Goldman N, Budich J C and Zoller P 2016 Topological quantum matter with ultracold gases in optical lattices *Nat. Phys.* **12** 639–45

[6] Shapiro B 2012 Cold atoms in the presence of disorder *J. Phys. A: Math. Theor.* **45** 143001

[7] Bakr W S, Gillen J I, Peng A, Fölling S and Greiner M 2009 A quantum gas microscope for detecting single atoms in a Hubbard-regime optical lattice *Nature* **462** 74–7

[8] Sherson J F, Weitenberg C, Endres M, Cheneau M, Bloch I and Kuhr S 2010 Single-atom-resolved fluorescence imaging of an atomic Mott insulator *Nature* **467** 68–72

[9] Parsons M F, Huber F, Mazurenko A, Chiu C S, Setiawan W, Wooley-Brown K, Blatt S and Greiner M 2015 Site-resolved imaging of fermionic ^{6}Li in an optical lattice *Phys. Rev. Lett.* **114** 213002

[10] Cheuk L W, Nichols M A, Okan M, Gersdorf T, Ramasesh V V, Bakr W S, Lompe T and Zwierlein M W 2015 Quantum-gas microscope for fermionic atoms *Phys. Rev. Lett.* **114** 193001

[11] Haller E, Hudson J, Kelly A, Cotta D A, Peaudecerf B, Bruce G D and Kuhr S 2015 Single-atom imaging of fermions in a quantum-gas microscope *Nat. Phys.* **11** 738–42

[12] Yamamoto R, Kobayashi J, Kuno T, Kato K and Takahashi Y 2015 An ytterbium quantum gas microscope with narrow-line laser cooling *New J. Phys.* **18** 023016

[13] Edge G J A, Anderson R, Jervis D, McKay D C, Day R, Trotzky S and Thywissen J H 2015 Imaging and addressing of individual fermionic atoms in an optical lattice *Phys. Rev. A* **92** 063406

[14] Omran A, Boll M, Hilker T A, Kleinlein K, Salomon G, Bloch I and Gross C 2015 Microscopic observation of Pauli blocking in degenerate fermionic lattice gases *Phys. Rev. Lett.* **115** 263001

[15] Ketterle W and Zwierlein M W 2008 Making, probing and understanding ultracold Fermi gases *Nuovo Cimento Riv. Ser.* **31** 247–422

[16] Ott H, de Mirandes E, Ferlaino F, Roati G, Modugno G and Inguscio M 2004 Collisionally induced transport in periodic potentials *Phys. Rev. Lett.* **92** 160601

[17] Schneider U *et al* 2012 Fermionic transport and out-of-equilibrium dynamics in a homogeneous Hubbard model with ultracold atoms *Nat. Phys.* **8** 213–8

[18] Brantut J-P, Meineke J, Stadler D, Krinner S and Esslinger T 2012 Conduction of ultracold fermions through a mesoscopic channel *Science* **337** 1069–71

[19] Stadler D, Krinner S, Meineke J, Brantut J-P and Esslinger T 2012 Observing the drop of resistance in the flow of a superfluid Fermi gas *Nature* **491** 736–9

[20] Brantut J-P, Grenier C, Meineke J, Stadler D, Krinner S, Kollath C, Esslinger T and Georges A 2013 A thermoelectric heat engine with ultracold atoms *Science* **342** 713–5

[21] Krinner S, Stadler D, Meineke J, Brantut J-P and Esslinger T 2013 Superfluidity with disorder in a thin film of quantum gas *Phys. Rev. Lett.* **110** 100601

[22] Krinner S, Stadler D, Husmann D, Brantut J-P and Esslinger T 2015 Observation of quantized conductance in neutral matter *Nature* **517** 64–7

[23] Krinner S, Stadler D, Meineke J, Brantut J-P and Esslinger T 2015 Observation of a fragmented, strongly interacting Fermi gas *Phys. Rev. Lett.* **115** 045302

[24] Husmann D, Uchino S, Krinner S, Lebrat M, Giamarchi T, Esslinger T and Brantut J-P 2015 Connecting strongly correlated superfluids by a quantum point contact *Science* **350** 1498–501

[25] Krinner S, Lebrat M, Husmann D, Grenier C, Brantut J-P and Esslinger T 2016 Mapping out spin and particle conductances in a quantum point contact *Proc. Natl Acad. Sci.* **113** 8144–9

[26] Dalfovo F, Giorgini S, Pitaevskii L P and Stringari S 1999 Theory of Bose–Einstein condensation in trapped gases *Rev. Mod. Phys.* **71** 463–512

[27] Ferlaino F, Maddaloni P, Burger S, Cataliotti F S, Fort C, Modugno M and Inguscio M 2002 Dynamics of a Bose–Einstein condensate at finite temperature in an atom-optical coherence filter *Phys. Rev.* A **66** 011604

[28] Modugno G, Ferlaino F, Heidemann R, Roati G and Inguscio M 2003 Production of a Fermi gas of atoms in an optical lattice *Phys. Rev.* A **68** 011601

[29] Pezzè L, Pitaevskii L, Smerzi A, Stringari S, Modugno G, de Mirandes E, Ferlaino F, Ott H, Roati G and Inguscio M 2004 Insulating behavior of a trapped ideal Fermi gas *Phys. Rev. Lett.* **93** 120401

[30] Fertig C D, O'Hara K M, Huckans J H, Rolston S L, Phillips W D and Porto J V 2005 Strongly inhibited transport of a degenerate 1D Bose gas in a lattice *Phys. Rev. Lett.* **94** 120403

[31] Lye J E, Fallani L, Modugno M, Wiersma D S, Fort C and Inguscio M 2005 Bose–Einstein condensate in a random potential *Phys. Rev. Lett.* **95** 070401

[32] Strohmaier N, Takasu Y, Günter K, Jördens R, Köhl M, Moritz H and Esslinger T 2007 Interaction-controlled transport of an ultracold Fermi gas *Phys. Rev. Lett.* **99** 220601

[33] Chen Y P, Hitchcock J, Dries D, Junker M, Welford C and Hulet R G 2008 Phase coherence and superfluid-insulator transition in a disordered Bose–Einstein condensate *Phys. Rev.* A **77** 033632

[34] Ben Dahan M, Peik E, Reichel J, Castin Y and Salomon C 1996 Bloch oscillations of atoms in an optical potential *Phys. Rev. Lett.* **76** 4508–11

[35] Anderson B P and Kasevich M A 1998 Macroscopic quantum interference from atomic tunnel arrays *Science* **282** 1686–9

[36] Morsch O, Müller J H, Cristiani M, Ciampini D and Arimondo E 2001 Bloch oscillations and mean-field effects of Bose–Einstein condensates in 1D optical lattices *Phys. Rev. Lett.* **87** 140402

[37] Roati G, de Mirandes E, Ferlaino F, Ott H, Modugno G and Inguscio M 2004 Atom interferometry with trapped Fermi gases *Phys. Rev. Lett.* **92** 230402

[38] Gustavsson M, Haller E, Mark M J, Danzl J G, Rojas-Kopeinig G and Nägerl H-C 2008 Control of interaction-induced dephasing of Bloch oscillations *Phys. Rev. Lett.* **100** 080404

[39] Fattori M, D'Errico C, Roati G, Zaccanti M, Jona-Lasinio M, Modugno M, Inguscio M and Modugno G 2008 Atom interferometry with a weakly interacting Bose–Einstein condensate *Phys. Rev. Lett.* **100** 080405

[40] Drenkelforth S, Kleine Büning G, Will J, Schulte T, Murray N, Ertmer W, Santos L and Arlt J J 2008 Damped Bloch oscillations of Bose–Einstein condensates in disordered potential gradients *New J. Phys.* **10** 045027

[41] Eckstein M and Werner P 2011 Damping of Bloch oscillations in the Hubbard model *Phys. Rev. Lett.* **107** 186406

[42] Fort C, Fallani L, Guarrera V, Lye J E, Modugno M, Wiersma D S and Inguscio M 2005 Effect of optical disorder and single defects on the expansion of a Bose–Einstein condensate in a one-dimensional waveguide *Phys. Rev. Lett.* **95** 170410

[43] Clément D, Varón A F, Hugbart M, Retter J A, Bouyer P, Sanchez-Palencia L, Gangardt D M, Shlyapnikov G V and Aspect A 2005 Suppression of transport of an interacting elongated Bose–Einstein condensate in a random potential *Phys. Rev. Lett.* **95** 170409

[44] Roati G, D'Errico C, Fallani L, Fattori M, Fort C, Zaccanti M, Modugno G, Modugno M and Inguscio M 2008 Anderson localization of a non-interacting Bose–Einstein condensate *Nature* **453** 895–8

[45] Billy J, Josse V, Zuo Z, Bernard A, Hambrecht B, Lugan P, Clément D, Sanchez-Palencia L, Bouyer P and Aspect A 2008 Direct observation of Anderson localization of matter waves in a controlled disorder *Nature* **453** 891–4

[46] Robert-de Saint-Vincent M, Brantut J-P, Allard B, Plisson T, Pezzé L, Sanchez-Palencia L, Aspect A, Bourdel T and Bouyer P 2010 Anisotropic 2D diffusive expansion of ultracold atoms in a disordered potential *Phys. Rev. Lett.* **104** 220602

[47] Kondov S S, McGehee W R, Zirbel J J and DeMarco B 2011 Three-dimensional Anderson localization of ultracold matter *Science* **334** 66–8

[48] Jendrzejewski F, Bernard A, Muller K, Cheinet P, Josse V, Piraud M, Pezze L, Sanchez-Palencia L, Aspect A and Bouyer P 2012 Three-dimensional localization of ultracold atoms in an optical disordered potential *Nat. Phys.* **8** 398–403

[49] Ronzheimer J P, Schreiber M, Braun S, Hodgman S S, Langer S, McCulloch I P, Heidrich-Meisner F, Bloch I and Schneider U 2013 Expansion dynamics of interacting bosons in homogeneous lattices in one and two dimensions *Phys. Rev. Lett.* **110** 205301

[50] Hagley E W, Deng L, Kozuma M, Wen J, Helmerson K, Rolston S L and Phillips W D 1999 A well-collimated quasi-continuous atom laser *Science* **283** 1706–9

[51] Bloch I, Hänsch T W and Esslinger T 1999 Atom laser with a CW output coupler *Phys. Rev. Lett.* **82** 3008–11

[52] Guerin W, Riou J-F, Gaebler J P, Josse V, Bouyer P and Aspect A 2006 Guided quasicontinuous atom laser *Phys. Rev. Lett.* **97** 200402

[53] Couvert A, Jeppesen M, Kawalec T, Reinaudi G, Mathevet R and Guéry-Odelin D 2008 A quasi-monomode guided atom laser from an all-optical Bose–Einstein condensate *Eur. Phys. Lett.* **83** 5001

[54] Robins N P, Figl C, Jeppesen M, Dennis G R and Close J D 2008 A pumped atom laser *Nat. Phys.* **4** 731–6

[55] Vidmar L, Ronzheimer J P, Schreiber M, Braun S, Hodgman S S, Langer S, Heidrich-Meisner F, Bloch I and Schneider U 2015 *Phys. Rev. Lett.* **115** 175301

[56] Cao C, Elliott E, Wu H and Thomas J E 2011 Searching for perfect fluids: quantum viscosity in a universal Fermi gas *New J. Phys.* **13** 075007

[57] Cao C, Elliott E, Joseph J, Wu H, Petricka J, Schäfer T and Thomas J E 2011 Universal quantum viscosity in a unitary Fermi gas *Science* **331** 58–61

[58] Fetter A L 2008 Rotating trapped Bose–Einstein condensates *Laser Physics* **18** 1–11

[59] Cooper N R 2008 Rapidly rotating atomic gases *Adv. Phys.* **57** 539–616

[60] Ryu C, Andersen M F, Cladé P, Natarajan V, Helmerson K and Phillips W D 2007 Observation of persistent flow of a Bose–Einstein condensate in a toroidal trap *Phys. Rev. Lett.* **99** 260401

[61] Ramanathan A, Wright K C, Muniz S R, Zelan M, Hill W T, Lobb C J, Helmerson K, Phillips W D and Campbell G K 2011 Superflow in a toroidal Bose–Einstein condensate: an atom circuit with a tunable weak link *Phys. Rev. Lett.* **106** 130401

[62] Beattie S, Moulder S, Fletcher R J and Hadzibabic Z 2013 Persistent currents in spinor condensates *Phys. Rev. Lett.* **110** 025301

[63] Ryu C, Blackburn P W, Blinova A A and Boshier M G 2013 Experimental realization of Josephson junctions for an atom squid *Phys. Rev. Lett.* **111** 205301

[64] Orzel C, Tuchman A K, Fenselau M L, Yasuda M and Kasevich M A 2001 Squeezed states in a Bose–Einstein condensate *Science* **291** 2386–90

[65] Cataliotti F S, Burger S, Fort C, Maddaloni P, Minardi F, Trombettoni A, Smerzi A and Inguscio M 2001 Josephson junction arrays with Bose–Einstein condensates *Science* **293** 843–6

[66] Albiez M, Gati R, Fölling J, Hunsmann S, Cristiani M and Oberthaler M K 2005 Direct observation of tunneling and nonlinear self-trapping in a single bosonic Josephson junction *Phys. Rev. Lett.* **95** 010402

[67] Levy S, Lahoud E, Shomroni I and Steinhauer J 2007 The a.c. and d.c. Josephson effects in a Bose–Einstein condensate *Nature* **449** 579–83

[68] LeBlanc L J, Bardon A B, McKeever J, Extavour M H T, Jervis D, Thywissen J H, Piazza F and Smerzi A 2011 Dynamics of a tunable superfluid junction *Phys. Rev. Lett.* **106** 025302

[69] Valtolina G *et al* 2015 Josephson effect in fermionic superfluids across the BEC-BCS crossover *Science* **350** 1505–8

[70] Sommer A, Ku M, Roati G and Zwierlein M W 2011 Universal spin transport in a strongly interacting Fermi gas *Nature* **472** 201–4

[71] Fukuhara T *et al* 2013 Quantum dynamics of a mobile spin impurity *Nat. Phys.* **9** 235–41

[72] Koschorreck M, Pertot D, Vogt E and Kohl M 2013 Universal spin dynamics in two-dimensional Fermi gases *Nat. Phys.* **9** 405–9

[73] Bardon A B *et al* 2014 Transverse demagnetization dynamics of a unitary Fermi gas *Science* **344** 722–4

[74] Hild S, Fukuhara T, Schauß P, Zeiher J, Knap M, Demler E, Bloch I and Gross C 2014 Far-from-equilibrium spin transport in Heisenberg quantum magnets *Phys. Rev. Lett.* **113** 147205

[75] Trotzky S, Beattie S, Luciuk C, Smale S, Bardon B, Enss T A, Taylor E, Zhang S and Thywissen H J 2015 Observation of the Leggett–Rice effect in a unitary Fermi gas *Phys. Rev. Lett.* **114** 015301

[76] Meppelink R, van Rooij R, Vogels J M and van der Straten P 2009 Enhanced heat flow in the hydrodynamic collisionless regime *Phys. Rev. Lett.* **103** 095301

[77] Hazlett E L, Ha L-C and Chin C 2013 Anomalous thermoelectric transport in two-dimensional Bose gas (arXiv:1306.4018)

[78] Sidorenkov L A, Tey M K, Grimm R, Hou Y-H, Pitaevskii L and Stringari S 2013 Second sound and the superfluid fraction in a Fermi gas with resonant interactions *Nature* **498** 78–81

[79] Barontini G, Labouvie R, Stubenrauch F, Vogler A, Guarrera V and Ott H 2013 Controlling the dynamics of an open many-body quantum system with localized dissipation *Phys. Rev. Lett.* **110** 035302

[80] Labouvie R, Santra B, Heun S, Wimberger S and Ott H 2015 Negative differential conductivity in an interacting quantum gas *Phys. Rev. Lett.* **115** 050601

[81] Chin C, Bartenstein M, Altmeyer A, Riedl S, Jochim S, Denschlag J H and Grimm R 2004 Observation of the pairing gap in a strongly interacting Fermi gas *Science* **305** 1128–31

[82] Törmä P and Sengstock K 2014 *Quantum Gas Experiments: Exploring Many-Body States* vol 3 (Singapore: World Scientific)

[83] Stenger J, Inouye S, Chikkatur A P, Stamper-Kurn D M, Pritchard D E and Ketterle W 1999 Bragg spectroscopy of a Bose–Einstein condensate *Phys. Rev. Lett.* **82** 4569–73

[84] Veeravalli G, Kuhnle E, Dyke P and Vale C J 2008 Bragg Spectroscopy of a strongly interacting Fermi gas *Phys. Rev. Lett.* **101** 250403

[85] Onsager L 1931 Reciprocal relations in irreversible processes. I *Phys. Rev.* **37** 405–26

[86] Callen H B 1948 The application of Onsager's reciprocal relations to thermoelectric, thermomagnetic and galvanomagnetic effects *Phys. Rev.* **73** 1349–58

[87] Reichel J and Vuletic V 2011 *Atom Chips* (New York: Wiley)

[88] Zimmermann B, Müller T, Meineke J, Esslinger T and Moritz H 2011 High-resolution imaging of ultracold fermions in microscopically tailored optical potentials *New J. Phys.* **13** 043007

[89] Köhler T, Góral K and Julienne P S 2006 Production of cold molecules via magnetically tunable Feshbach resonances *Rev. Mod. Phys.* **78** 1311–61

[90] Chin C, Grimm R, Julienne P and Tiesinga E 2010 Feshbach resonances in ultracold gases *Rev. Mod. Phys.* **82** 1225–86

[91] Zürn G, Lompe T, Wenz A N, Jochim S, Julienne P S and Hutson J M 2013 Precise characterization of ^{6}li Feshbach resonances using trap-sideband-resolved RF spectroscopy of weakly bound molecules *Phys. Rev. Lett.* **110** 135301

[92] Smith N L, Heathcote W H, Hechenblaikner G, Nugent E and Foot C J 2005 Quasi-2D confinement of a BEC in a combined optical and magnetic potential *J. Phys. B: At. Mol. Phys.* **38** 223–35

[93] Meyrath T P, Schreck F, Hanssen J L, Chuu C-S and Raizen M G 2005 A high frequency optical trap for atoms using Hermite–Gaussian beams *Opt. Express* **13** 2843

[94] Lee J G, McIlvain B J, Lobb C J and Hill W T III 2013 Analogs of basic electronic circuit elements in a free-space atom chip *Sci. Rep.* **3** 1034

[95] Luo L and Thomas J E 2009 Thermodynamic measurements in a strongly interacting Fermi gas *J. Low Temp. Phys.* **154** 1–29

[96] Horikoshi M, Nakajima S, Ueda M and Mukaiyama T 2010 Measurement of universal thermodynamic functions for a unitary Fermi gas *Science* **327** 442

[97] Nascimbène S, Navon N, Jiang K J, Chevy F and Salomon C 2010 Exploring the thermodynamics of a universal Fermi gas *Nature* **463** 1057–60

[98] Navon N, Nascimbène S, Chevy F and Salomon C 2010 The equation of state CF a low-temperature Fermi gas with tunable interactions *Science* **328** 729

[99] Ku M J H, Sommer A T, Cheuk L W and Zwierlein M W 2012 Revealing the superfluid lambda transition in the universal thermodynamics of a unitary Fermi gas *Science* **335** 563–7

[100] Datta S 1995 *Electronic Transport in Mesoscopic Systems* (Cambridge: Cambridge University Press)

[101] Pothier H, Guéron S, Birge N O, Esteve D and Devoret M H 1997 Energy distribution of electrons in an out-of-equilibrium metallic wire *Z. Phys. B: Condens. Matter* **104** 178–82

[102] Pothier H, Guéron S, Birge N O, Esteve D and Devoret M H 1997 Energy distribution function of quasiparticles in mesoscopic wires *Phys. Rev. Lett.* **79** 3490–3

[103] Georges A 2013 Thermoelectricity: concepts, materials, challenges, available on www.college-de-france.fr

[104] Demarco B L 2001 Quantum behavior of an atomic Fermi gas *PhD Thesis* University of Colorado at Boulder

[105] Grenier C, Kollath C and Georges A 2012 Probing thermoelectric transport with cold atoms (arXiv:1209.3942)

[106] Kuhn R C, Sigwarth O, Miniatura C, Delande D and Müller C A 2007 Coherent matter wave transport in speckle potentials *New J. Phys.* **9** 161

[107] Choi J-Y, Hild S, Zeiher J, Schauß P, Rubio-Abadal A, Yefsah T, Khemani V, Huse D A, Bloch I and Gross C 2016 Exploring the many-body localization transition in two dimensions *Science* **352** 1547

[108] Wong C H, Stoof H T C and Duine R A 2012 Spin-Seebeck effect in a strongly interacting Fermi gas *Phys. Rev. A* **85** 063613

[109] Kim H and Huse D A 2012 Heat and spin transport in a cold atomic Fermi gas *Phys. Rev. A* **86** 053607

[110] Sommer A, Ku M and Zwierlein M W 2011 Spin transport in polaronic and superfluid Fermi gases *New J. Phys.* **13** 055009

[111] Grenier C, Georges A and Kollath C 2014 Peltier cooling of fermionic quantum gases *Phys. Rev. Lett.* **113** 200601

[112] Grenier C, Kollath C and Georges A Thermoelectric transport and Peltier cooling of cold atomic gases *C. R. Phys.* **17** 1161

[113] Sekera T, Bruder C and Belzig W 2016 Thermoelectricity in a junction between interacting cold atomic Fermi gases *Phys. Rev. A* **94** 033618

[114] Roßnagel J, Dawkins S T, Tolazzi K N, Abah O, Lutz E, Schmidt-Kaler F and Singer K 2016 A single-atom heat engine *Science* **352** 325

[115] Roßnagel J, Abah O, Schmidt-Kaler F, Singer K and Lutz E 2014 Nanoscale heat engine beyond the Carnot limit *Phys. Rev. Lett.* **112** 030602

[116] Giorgini S, Pitaevskii L P and Stringari S 2008 Theory of ultracold atomic Fermi gases *Rev. Mod. Phys.* **80** 1215–74

[117] Petrov D, Gangardt D and Shlyapnikov G 2004 Low-dimensional trapped gases *J. Phys.* IV **116** 5–44

[118] Kinoshita T, Wenger T and Weiss D S 2006 A quantum Newton's cradle *Nature* **440** 900–3

[119] Gring M, Kuhnert M, Langen T, Kitagawa T, Rauer B, Schreitl M, Mazets I, Smith D A, Demler E and Schmiedmayer J 2012 Relaxation and prethermalization in an isolated quantum system *Science* **337** 1318–22

[120] Kanász-Nagy M, Glazman L, Esslinger T and Demler E A 2016 Anomalous conductances in an ultracold quantum wire *Phys. Rev. Lett.* **117** 255302

[121] Imry Y and Landauer R 1999 Conductance viewed as transmission *Rev. Mod. Phys.* **71** S306–12

[122] Martin T and Landauer R 1992 Wave-packet approach to noise in multichannel mesoscopic systems *Phys. Rev. B* **45** 1742–55

[123] Batra I P 1998 Origin of conductance quantization *Surf. Sci.* **395** 43–5

[124] Chien C-C, Di Ventra M and Zwolak M 2014 Landauer, Kubo and microcanonical approaches to quantum transport and noise: a comparison and implications for cold-atom dynamics *Phys. Rev. A* **90** 023624

[125] Chien C-C, Peotta S and Di Ventra M 2015 Quantum transport in ultracold atoms *Nat. Phys.* **11** 998–1004

[126] Bruderer M and Belzig W 2012 Mesoscopic transport of fermions through an engineered optical lattice connecting two reservoirs *Phys. Rev. A* **85** 013623

[127] Nietner C, Schaller G and Brandes T 2014 Transport with ultracold atoms at constant density *Phys. Rev. A* **89** 013605

[128] Thywissen J H, Westervelt R M and Prentiss M 1999 Quantum point contacts for neutral atoms *Phys. Rev. Lett.* **83** 3762–5

[129] Papoular D J, Pitaevskii L P and Stringari S 2016 Quantized conductance through the quantum evaporation of bosonic atoms *Phys. Rev. A* **94** 023622

[130] Montie E A, Cosman E C, 't Hooft G W, van der Mark M B and Beenakker C W J 1991 Observation of the optical analogue of quantized conductance of a point contact *Nature* **350** 594–5

[131] Rego L G C and Kirczenow G 1998 Quantized thermal conductance of dielectric quantum wires *Phys. Rev. Lett.* **81** 232–5

[132] Schwab K, Henriksen E A, Worlock J M and Roukes M L 2000 Measurement of the quantum of thermal conductance *Nature* **404** 974–7

[133] Pendry J B 1983 Quantum limits to the flow of information and entropy *J. Phys. A: Math. Gen.* **16** 2161

[134] Jezouin S, Parmentier F D, Anthore A, Gennser U, Cavanna A, Jin Y and Pierre F 2013 Quantum limit of heat flow across a single electronic channel *Science* **342** 601–4

[135] Sato Y, Eom B-H and Packard R 2005 On the feasibility of detecting quantized conductance in neutral matter *J. Low Temp. Phys.* **141** 99

[136] Lambert G, Gervais G and Mullin W J 2008 Quantum-limited mass flow of liquid ^{3}He *Low Temp. Phys.* **34** 249–53

[137] Josephson B D 1962 Possible new effects in superconductive tunnelling *Phys. Lett.* **1** 251–3

[138] Anderson P W 1966 Considerations on the flow of superfluid helium *Rev. Mod. Phys.* **38** 298–310

[139] Packard R E 1998 The role of the Josephson–Anderson equation in superfluid helium *Rev. Mod. Phys.* **70** 641–51

[140] Leggett A J 2006 *Quantum Liquids: Bose Condensation and Cooper Pairing in Condensed-Matter Systems* (Oxford: Oxford University Press)

[141] Varoquaux E 2015 Anderson's considerations on the flow of superfluid helium: some offshoots *Rev. Mod. Phys.* **87** 803–54

[142] Madison K W, Chevy F, Wohlleben W and Dalibard J 2000 Vortex formation in a stirred Bose–Einstein condensate *Phys. Rev. Lett.* **84** 806–9

[143] Zwierlein M W, Abo-Shaeer J R, Schirotzek A, Schunck C H and Ketterle W 2005 Vortices and superfluidity in a strongly interacting Fermi gas *Nature* **435** 1047–51

[144] Onofrio R, Raman C, Vogels J M, Abo-Shaeer J R, Chikkatur A P and Ketterle W 2000 Observation of superfluid flow in a Bose–Einstein condensed gas *Phys. Rev. Lett.* **85** 2228–31

[145] Desbuquois R, Chomaz L, Yefsah T, Leonard J, Beugnon J, Weitenberg C and Dalibard J 2012 Superfluid behaviour of a two-dimensional Bose gas *Nat. Phys.* **8** 645–8

[146] Weimer W, Morgener K, Singh V P, Siegl J, Hueck K, Luick N, Mathey L and Moritz H 2015 Critical velocity in the BEC-BCS crossover *Phys. Rev. Lett.* **114** 095301

[147] Miller D E, Chin J K, Stan C A, Liu Y, Setiawan W, Sanner C and Ketterle W 2007 Critical velocity for superfluid flow across the BEC-BCS crossover *Phys. Rev. Lett.* **99** 070402

[148] Fagaly R L 2006 Superconducting quantum interference device instruments and applications *Rev. Sci. Instrum.* **77** 101101

[149] Feynman R P and Gorter C J 1955 *Chapter II Application of Quantum Mechanics to Liquid Helium* vol 1 (Amsterdam: Elsevier) pp 17–53

[150] Wright K C, Blakestad R B, Lobb C J, Phillips W D and Campbell G K 2013 Driving phase slips in a superfluid atom circuit with a rotating weak link *Phys. Rev. Lett.* **110** 025302

[151] Eckel S, Lee J G, Jendrzejewski F, Murray N, Clark C W, Lobb C J, Phillips W D, Edwards M and Campbell G K 2014 Hysteresis in a quantized superfluid 'atomtronic' circuit *Nature* **506** 200–3

[152] Greiner M, Mandel O, Esslinger T, Hänsch T W and Bloch I 2002 Quantum phase transition from a superfluid to a Mott insulator in a gas of ultracold atoms *Nature* **415** 39–44

[153] Smerzi A, Fantoni S, Giovanazzi S and Shenoy S R 1997 Quantum coherent atomic tunneling between two trapped Bose–Einstein condensates *Phys. Rev. Lett.* **79** 4950–3

[154] Eckel S, Lee J G, Jendrzejewski F, Lobb C J, Campbell G K and Hill W T 2016 Contact resistance and phase slips in mesoscopic superfluid-atom transport *Phys. Rev.* A **93** 063619

[155] Partridge G B, Li W, Kamar R I, Liao Y-A and Hulet R G 2006 Pairing and phase separation in a polarized Fermi gas *Science* **311** 503–5

[156] Zwierlein M W, Schunck C H, Schirotzek A and Ketterle W 2006 Direct observation of the superfluid phase transition in ultracold Fermi gases *Nature* **442** 54–8

[157] Allen J and Misener A 1938 Flow of liquid helium II *Nature* **141** 75

[158] Kapitza P 1938 Viscosity of liquid helium below the l-point *Nature* **141** 74

[159] Balibar S 2007 The discovery of superfluidity *J. Low Temp. Phys.* **146** 441–70

[160] Jendrzejewski F, Eckel S, Murray N, Lanier C, Edwards M, Lobb C J and Campbell G K 2014 *Phys. Rev. Lett.* **113** 045305

[161] Sanchez-Palencia L and Lewenstein M 2010 Disordered quantum gases under control *Nat. Phys.* **6** 87–95

[162] Fallani L, Lye J E, Guarrera V, Fort C and Inguscio M 2007 Ultracold atoms in a disordered crystal of light: towards a Bose glass *Phys. Rev. Lett.* **98** 130404

[163] White M, Pasienski M, McKay D, Zhou S Q, Ceperley D and Demarco B 2009 Strongly interacting bosons in a disordered optical lattice *Phys. Rev. Lett.* **102** 055301

[164] Deissler B, Zaccanti M, Roati G, D'Errico C, Fattori M, Modugno M, Modugno G and Inguscio M 2010 Delocalization of a disordered bosonic system by repulsive interactions *Nat. Phys.* **6** 354–8

[165] Pasienski M, McKay D, White M and DeMarco B 2010 A disordered insulator in an optical lattice *Nat. Phys.* **6** 677–80

[166] Beeler M C, Reed M E W, Hong T and Rolston S L 2012 Disorder-driven loss of phase coherence in a quasi-2D cold atom system *New J. Phys.* **14** 073024

[167] Allard B, Plisson T, Holzmann M, Salomon G, Aspect A, Bouyer P and Bourdel T 2012 Effect of disorder close to the superfluid transition in a two-dimensional Bose gas *Phys. Rev.* A **85** 033602

[168] D'Errico C, Lucioni E, Tanzi L, Gori L, Roux G, McCulloch I P, Giamarchi T, Inguscio M and Modugno G 2014 Observation of a disordered bosonic insulator from weak to strong interactions *Phys. Rev. Lett.* **113** 095301

[169] Giamarchi T and Schulz H J 1988 Anderson localization and interactions in one-dimensional metals *Phys. Rev.* B **37** 325–40

[170] Fisher M P A, Weichman P B, Grinstein G and Fisher D S 1989 Boson localization and the superfluid-insulator transition *Phys. Rev.* B **40** 546–70

[171] Pollet L, Prokof'ev N V, Svistunov B V and Troyer M 2009 Absence of a direct superfluid to Mott insulator transition in disordered Bose systems *Phys. Rev. Lett.* **103** 140402

[172] Krinner S, Stadler D, Meineke J, Brantut J-P and Esslinger T 2014 Erratum: Superfluidity with disorder in a thin film of quantum gas (2013 *Phys. Rev. Lett.* 110 100601) *Phys. Rev. Lett.* **112** 119901

[173] Weinrib A 1982 Percolation threshold of a two-dimensional continuum system *Phys. Rev.* B **26** 1352–61

[174] Pezzé L, Robert-de-Saint-Vincent M, Bourdel T, Brantut J-P, Allard B, Plisson T, Aspect A, Bouyer P and Sanchez-Palencia L 2011 Regimes of classical transport of cold gases in a two-dimensional anisotropic disorder *New J. Phys.* **13** 095015

[175] Goldman A M and Markovic N 1998 Superconductor-insulator transitions in the two-dimensional limit *Phys. Today* **51** 39–44

[176] Gantmakher V F and Dolgopolov V T 2010 Superconductor-insulator quantum phase transition *Phys.—Usp.* **53** 1

[177] Basko D, Aleiner I and Altshuler B 2006 On the problem of many-body localization *Problems Condens. Matter Phys.* 50–70

[178] Aleiner I L, Altshuler B L and Shlyapnikov G V 2010 A finite-temperature phase transition for disordered weakly interacting bosons in one dimension *Nat. Phys.* **6** 900–4

[179] Altman E and Vosk R 2015 Universal dynamics and renormalization in many body localized systems *Ann. Rev. Condensed Matter Phys.* **6** 383–409

[180] Nandkishore R and Huse D A 2015 Many-body localization and thermalization in quantum statistical mechanics *Ann. Rev. Condens. Matter Phys.* **6** 15–38

[181] Schreiber M, Hodgman S S, Bordia P, Lüschen H P, Fischer M H, Vosk R, Altman E, Schneider U and Bloch I 2015 Observation of many-body localization of interacting fermions in a quasirandom optical lattice *Science* **349** 842–5

[182] Kohstall C, Riedl S, Guajardo E R S, Sidorenkov L A, Denschlag J H and Grimm R 2011 Observation of interference between two molecular Bose–Einstein condensates *New J. Phys.* **13** 065027

[183] Yang C N 1962 Concept of off-diagonal long-range order and the quantum phases of liquid He and of superconductors *Rev. Mod. Phys.* **34** 694–704

[184] van der Post N, Peters E T, Yanson I K and van Ruitenbeek J M 1994 Subgap structure as function of the barrier in atom-size superconducting tunnel junctions *Phys. Rev. Lett.* **73** 2611–3

[185] Goffman M F, Cron R, Levy Yeyati A, Joyez P, Devoret M H, Esteve D and Urbina C 2000 Supercurrent in atomic point contacts and Andreev states *Phys. Rev. Lett.* **85** 170–3

[186] Bretheau L 2013 Localized excitations in superconducting atomic contacts: probing the Andreev doublet, *PhD Thesis*, Ecole Polytechnique

[187] Schirotzek A, Shin Y-I, Schunck C H and Ketterle W 2008 Determination of the superfluid gap in atomic Fermi gases by quasiparticle spectroscopy *Phys. Rev. Lett.* **101** 140403

[188] Kyröla E and Stenholm S 1977 Velocity tuned resonances as multi-Doppleron processes *Opt. Commun.* **22** 123–6

[189] Glück M, Kolovsky A R and Korsch H J 2002 Wannier–Stark resonances in optical and semiconductor superlattices *Phys. Rep.* **366** 103–82

[190] Yefsah T, Sommer A T, Ku M J H, Cheuk L W, Ji W, Bakr W S and Zwierlein M W 2013 Heavy solitons in a fermionic superfluid *Nature* **499** 426–30

[191] Ku M J H, Ji W, Mukherjee B, Guardado-Sanchez E, Cheuk L W, Yefsah T and Zwierlein M W 2014 Motion of a solitonic vortex in the BEC-BCS crossover *Phys. Rev. Lett.* **113** 065301

[192] Kleinsasser A W, Miller R E, Mallison W H and Arnold G B 1994 Observation of multiple Andreev reflections in superconducting tunnel junctions *Phys. Rev. Lett.* **72** 1738–41

[193] Shiba H 1968 Classical spins in superconductors *Prog. Theor. Phys.* **40** 435–51

[194] Kitaev A Y 2001 Unpaired Majorana fermions in quantum wires *Phys.—Usp.* **44** 131

[195] Jiang L, Kitagawa T, Alicea J, Akhmerov A R, Pekker D, Refael G, Cirac J I, Demler E, Lukin M D and Zoller P 2011 Majorana fermions in equilibrium and in driven cold-atom quantum wires *Phys. Rev. Lett.* **106** 220402

[196] Haussmann R, Rantner W, Cerrito S and Zwerger W 2007 Thermodynamics of the BCS-BEC crossover *Phys. Rev. A* **75** 023610

[197] Uchino S and Ueda M 2017 Anomalous transport in the superfluid fluctuation regime *Phys. Rev. Lett.* **118** 105303

[198] Liu B, Zhai H and Zhang S 2014 *Phys. Rev. A* **90** 051602

[199] Liu B, Zhai H and Zhang S 2017 *Phys. Rev. A* **95** 013623

[200] Gaebler J P, Stewart J T, Drake T E, Jin D S, Perali A, Pieri P and Strinati G C 2010 Observation of pseudogap behaviour in a strongly interacting Fermi gas *Nat. Phys.* **6** 569–73

[201] Sagi Y, Drake T E, Paudel R, Chapurin R and Jin D S 2015 Breakdown of the Fermi liquid description for strongly interacting fermions *Phys. Rev. Lett.* **114** 075301

[202] Taylor E 2009 Critical behavior in trapped strongly interacting Fermi gases *Phys. Rev. A* **80** 023612

[203] Debelhoir T and Dupuis N 2016 Critical region of the superfluid transition in the BCS-BEC crossover *Phys. Rev. A* **93** 023642

[204] Giamarchi T 2003 *Quantum Physics in One Dimension* (*Int. Series of Monographs on Physics*) (Oxford: Clarendon)

[205] DeMarco B, Papp S B and Jin D S 2001 Pauli blocking of collisions in a quantum degenerate atomic Fermi gas *Phys. Rev. Lett.* **86** 5409–12

[206] Gensemer S D and Jin D S 2001 Transition from collisionless to hydrodynamic behavior in an ultracold Fermi gas *Phys. Rev. Lett.* **87** 173201

[207] Valtolina G, Scazza F, Amico A, Burchianti A, Recati A, Enss T, Inguscio M, Zaccanti M and Roati G 2017 Evidence for ferromagnetic instability in a repulsive Fermi gas of ultracold atoms (https://doi.org/10.1038/nphys4108)

[208] Shin Y, Zwierlein M W, Schunck C H, Schirotzek A and Ketterle W 2006 Observation of phase separation in a strongly interacting imbalanced Fermi gas *Phys. Rev. Lett.* **97** 030401

[209] Zupancic P, Preiss P M, Ma R, Lukin A, Eric Tai M, Rispoli M, Islam R and Greiner M 2016 Ultra-precise holographic beam shaping for microscopic quantum control *Opt. Express* **24** 13881–93

[210] Feynman R P 1982 Simulating physics with computers *Int. J. Theor. Phys.* **21** 467–88

[211] Cirac J I and Zoller P 2012 Goals and opportunities in quantum simulation *Nat. Phys.* **8** 264–6

[212] Lye J E, Hope J J and Close J D 2003 Nondestructive dynamic detectors for Bose–Einstein condensates *Phys. Rev. A* **67** 043609

[213] Öttl A, Ritter S, Köhl M and Esslinger T 2005 Correlations and counting statistics of an atom laser *Phys. Rev. Lett.* **95** 090404

[214] Albert M, Haack G, Flindt C and Büttiker M 2012 Electron waiting times in mesoscopic conductors *Phys. Rev. Lett.* **108** 186806

[215] Haack G, Albert M and Flindt C 2014 Distributions of electron waiting times in quantum-coherent conductors *Phys. Rev. B* **90** 205429

[216] Sachdev S 2007 *Quantum Phase Transitions* (New York: Wiley)

[217] Chen K, Liu L, Deng Y, Pollet L and Prokof'ev N 2014 Universal conductivity in a two-dimensional superfluid-to-insulator quantum critical system *Phys. Rev. Lett.* **112** 030402

[218] Witczak-Krempa W, Sorensen E S and Sachdev S 2014 The dynamics of quantum criticality revealed by quantum Monte Carlo and holography *Nat. Phys.* **10** 361–6

[219] Janvier C *et al* 2015 Coherent manipulation of Andreev states in superconducting atomic contacts *Science* **349** 1199

[220] Thomas K J, Nicholls J T, Simmons M Y, Pepper M, Mace D R and Ritchie D A 1996 Possible spin polarization in a one-dimensional electron gas *Phys. Rev. Lett.* **77** 135–8

[221] Rejec T and Meir Y 2006 Magnetic impurity formation in quantum point contacts *Nature* **442** 900–3

[222] Bauer F, Heyder J, Schubert E, Borowsky D, Taubert D, Bruognolo B, Schuh D, Wegscheider W, von Delft J and Ludwig S 2013 Microscopic origin of the '0.7-anomaly' in quantum point contacts *Nature* **501** 73–8

[223] Iqbal M J *et al* 2013 Odd and even Kondo effects from emergent localization in quantum point contacts *Nature* **501** 79–83

[224] Beenakker C W J and van Houten H 1991 Josephson current through a superconducting quantum point contact shorter than the coherence length *Phys. Rev. Lett.* **66** 3056–9